

UNITED STATES AIR FORCE
ARMSTRONG LABORATORY

**The Direct Problem in Ultra-Short Pulse
Electromagnetic Wave Propagation
and Scattering**

Peter G. Petropoulos

Operational Technologies Corporation
4100 NW Loop 410
San Antonio, TX 78229

August 1997

19980410 100

DTIC QUALITY INSPECTED 3

*Approved for public release;
distribution is unlimited.*

Occupational and Environmental Health
Directorate
Mathematical Products Division
2503 Gillingham Street
Brooks Air Force Base TX 78235-5102

NOTICES

This report is published as received and has not been edited by the staff of the Directed Energy Bioeffects Division, Human Effectiveness Directorate.

Publication of this report does not constitute approval or disapproval of the ideas or findings. It is published in the interest of scientific and technical information (STINFO) exchange.

When Government drawings, specifications, or other data are used for any purpose other than in connection with a definitely Government-related procurement, the United States Government incurs no responsibility or any obligation whatsoever. The fact that the Government may have formulated or in any way supplied the said drawings, specifications, or other data, is not to be regarded by implication, or otherwise in any manner construed, as licensing the holder or any other person or corporation; or as conveying any rights or permission to manufacture, use, or sell any patented invention that may in any way be related thereto.

The mention of trade names or commercial products in this publication is for illustration purposes and does not constitute endorsement or recommendation for use by the United State Air Force.

The Office of Public Affairs has reviewed this report, and it is releasable to the National Technical Information Service, where it will be available to the general public, including foreign nationals.

This report has been reviewed and is approved for publication.

Government agencies and their contractors registered with Defense Technical Information Center (DTIC) should direct requests for copies to: Defense Technical Information Center, 8725 John J. Kingman Rd., STE 0944, Ft. Belvoir, VA 22060-6218.

Non-Government agencies may purchase copies of this report from: National Technical Information Services (NTIS), 5285 Port Royal Road, Springfield, VA 22161-2103.



RICHARD L. MILLER, PhD
Chief, Directed Energy Bioeffects Division

REPORT DOCUMENTATION PAGE			Form Approved OMB No. 0704-0188	
Public reporting burden for this collection of information is estimated to average 1 hour per response, including the time for reviewing instructions, searching existing data sources, gathering and maintaining the data needed, and completing and reviewing the collection of information. Send comments regarding this burden estimate or any other aspect of this collection of information, including suggestions for reducing this burden, to Washington Headquarters Services, Directorate for Information Operations and Reports, 1215 Jefferson Davis Highway, Suite 1204, Arlington, VA 22202-4302, and to the Office of Management and Budget, Paperwork Reduction Project (0704-0188), Washington, DC 20503.				
1. AGENCY USE ONLY (Leave blank)		2. REPORT DATE August 1997		3. REPORT TYPE AND DATES COVERED Final, November 1994 - March 1995
4. TITLE AND SUBTITLE The Direct Problem in Ultra-Short Pulse Electromagnetic Wave Propagation and Scattering			5. FUNDING NUMBERS C: F41624-92-D-4001 PE: 62202F PR: 6770 TA: OS WU: 02	
6. AUTHOR(S) Peter G. Petropoulos				
7. PERFORMING ORGANIZATION NAME(S) AND ADDRESS(ES) Operational Technologies Corporation 4100 NW Loop 410 San Antonio Texas 78229			8. PERFORMING ORGANIZATION REPORT NUMBER	
9. SPONSORING/MONITORING AGENCY NAME(S) AND ADDRESS(ES) Armstrong Laboratory Occupational and Environmental Health Directorate Mathematical Products Division 2503 Gillingham Street Brooks Air Force Base Texas 78235-5102			10. SPONSORING/MONITORING AGENCY REPORT NUMBER AL/OE-TR-1997-0109	
11. SUPPLEMENTARY NOTES				
12a. DISTRIBUTION AVAILABILITY STATEMENT Approved for public release; distribution is unlimited.			12b. DISTRIBUTION CODE	
13. ABSTRACT (Maximum 200 words) This effort addressed the direct problem in electromagnetic wave propagation and scattering in dispersive dielectrics objects. Particularly, the research concentrated on the development of numerical approaches that can solve the problem in a timely fashion as accurately as possible given a reasonable amount of computational resources. In addition, analytical methods were developed for the purpose of extracting features of the problem which are special to dispersive objects. First, four existing Finite Difference Time Domain extensions for the modeling of pulse propagation in Debye or Lorentz dispersive media were analyzed through studying the stability and phase error properties of the coupled difference equations corresponding to Maxwell's equations and to the equations for the dispersion. In order to understand more fully the discretization requirements and the general behavior of existing numerical methods for dispersive media we considered the propagation of arbitrary electromagnetic pulses in anomalously dispersive dielectrics characterized by M relaxation processes. Armed with the knowledge that finite difference schemes, which are more accurate in space than in time, are better suited for modeling pulse propagation in dispersive dielectrics we next determined some important properties of such high-order schemes in comparison to standard schemes. Finally, we examined further aspects of electromagnetic pulse propagation in anomalously dispersive media, using the Debye model as an example.				
14. SUBJECT TERMS Biological models Electromagnetic wave propagation Radiofrequency radiation Electromagnetic wave scattering			15. NUMBER OF PAGES 106	
			16. PRICE CODE	
17. SECURITY CLASSIFICATION OF REPORT Unclassified	18. SECURITY CLASSIFICATION OF THIS PAGE Unclassified	19. SECURITY CLASSIFICATION OF ABSTRACT Unclassified	20. LIMITATION OF ABSTRACT UL	

THIS PAGE INTENTIONALLY LEFT BLANK

TABLE OF CONTENTS

	Page
I STABILITY AND PHASE ERROR ANALYSIS OF FD-TD IN DISPERSIVE DIELECTRICS	
Introduction	I-1
Stability Analysis	I-2
Debye Medium	I-2
Lorentz Medium	I-3
Phase Error Analysis	I-4
Debye Medium	I-4
Lorentz Medium	I-4
2/3 Dimensional Extensions	I-5
Discussion	I-5
Summary	I-7
References	I-7
Figures	I-8
 II THE WAVE HIERARCHY FOR PROPAGATION IN RELAXING DIELECTRICS	
Introduction	II-2
Formulation	II-4
The Wave Hierarchy	II-6

	Page
Analysis of the Hierarchy	II-8
Numerical Experiments	II-11
Ramifications for Numerical Schemes	II-16
References	II-17
III PHASE ERROR CONTROL FOR FD-TD METHODS OF SECOND AND FOURTH ORDER ACCURACY	
Introduction	III-2
Dispersion Analysis	III-3
Numerical Validation	III-8
Summary	III-11
References	III-13
IV A GENERAL DESCRIPTION OF PROPAGATION AND SCATTERING FOR ELECTROMAGNETIC PULSES IN DISPERSIVE MEDIA	
Introduction	IV-2
Formulation and Results	IV-4
PDEs	IV-4
Green Functions	IV-7
Derivations	IV-14
PDEs	IV-14
Green Functions	IV-16
Numerical Validation and Laboratory Experiments	IV-28

	Page
Conclusion	IV-37
Appendix A: Error Estimates	IV-38
References	IV-43

THIS PAGE INTENTIONALLY LEFT BLANK

SUMMARY

This report summarizes research done in the last two and one-half years as an employee of the Operational Technologies Corporation. The original assignment was with the Radiation Analysis Branch of the Directed Energy Division (AL/OEDA) but, due to a number of reorganizations, was finished with the Biomathematics Branch of the Mathematical Products Division (AL/OESB).

This effort addressed the direct problem in electromagnetic wave propagation and scattering in dispersive dielectrics objects. Particularly, the research concentrated on the development of numerical approaches that can solve the problem in a timely fashion as accurately as possible given a reasonable amount of computational resources. In addition, analytical methods were developed for the purpose of extracting features of the problem which are special to dispersive objects.

First, four existing Finite Difference Time Domain extensions for the modeling of pulse propagation in Debye or Lorentz dispersive media were analyzed through studying the stability and phase error properties of the coupled difference equations corresponding to Maxwell's equations and to the equations for the dispersion. For good overall accuracy we showed that all schemes should be run at their Courant stability limit, and that the timestep should finely resolve the medium timescales. Particularly, for Debye schemes it should be at least $\Delta t = 10^{-3}\tau$, while for Lorentz schemes it should be $\Delta t = 10^{-2}\tau$, where τ is a typical medium relaxation time. A numerical experiment with a Debye medium confirmed this. We also determined that two of the discretizations for Debye media are totally equivalent. In the Lorentz medium case we established that the method that uses the polarization differential equation to model dispersion is stable for all wavenumbers, and that the method using the local-in-time constitutive relation is weakly unstable for modes with wavenumber k such that $k\Delta x > \pi/2$.

In order to understand more fully the discretization requirements and the general behavior of existing numerical methods for dispersive media we considered the propagation of arbitrary electromagnetic pulses in anomalously dispersive dielectrics characterized by M relaxation processes. A partial differential equation for the electric field in the dielectric was derived and analyzed. This single equation describes a hierarchy of $M + 1$ wave types, each type characterized by an attenuation coefficient and a wave speed. Our analysis identified a "skin-depth" where the pulse response is described by a telegrapher's equation with smoothing

terms, travels with the wavefront speed, and decays exponentially. Past this shallow depth we showed that the pulse response is described by a weakly dispersive advection-diffusion equation, travels with the sub-characteristic advection speed equal to the zero-frequency phase velocity in the dielectric, and decays algebraically. The analysis was verified with a numerical simulation. The relevance of our results to the development of numerical methods for such problems was discussed.

Armed with the knowledge that finite difference schemes, which are more accurate in space than in time, are better suited for modeling pulse propagation in dispersive dielectrics we next determined some important properties of such high-order schemes in comparison to standard schemes. For Finite Difference Time Domain methods we determined the spatial resolution of the discretized domain in terms of the total computation time and the desired phase error. It was shown that the spatial step should vary as $\Delta x \sim g \left[\frac{e_\phi}{t_c} \right]^{1/s}$ in order to maintain a prescribed phase error level e_ϕ throughout the computation time t_c , where s ($=2$ or 4) is the spatial order of accuracy of the scheme and g is a geometric factor. Significantly, we showed that the thumb rule of using 10-20 points per wavelength to determine the spatial cell size for the standard scheme is not optimal. Our results were verified by numerical simulations in two dimensions with the Yee scheme and the new 4th-order accurate scheme.

Finally, we examined further aspects of electromagnetic pulse propagation in anomalously dispersive media, using the Debye model as an example. Short-pulse, long-pulse, short-time, and long-time approximations and amplitude rate of decay estimates were derived with asymptotic methods. We also studied the following problem: Knowing only the peak amplitude and power density of an incident pulse, what can be said about the peak amplitude of the propagated pulse? We provided sharp upper and lower bounds for the propagated amplitude which may be useful in controlling the electromagnetic interference or the damage produced in dispersive media. We explained a factor-of-nine effect in the speed of waves in a Debye model for water, which seems to have been previously unnoticed, and some observations from experimental studies of pulse propagation in biological materials. Finally, we proposed some guidelines for sample size in Transmission Time Domain Spectroscopy studies of dielectrics.

Stability and Phase Error Analysis of FD-TD in Dispersive Dielectrics

Abstract—Four FD-TD extensions for the modeling of pulse propagation in Debye or Lorentz dispersive media are analysed through studying the stability and phase error properties of the coupled difference equations corresponding to Maxwell's equations and to the equations for the dispersion. For good overall accuracy we show that all schemes should be run at their Courant stability limit, and that the timestep should finely resolve the medium timescales. Particularly, for Debye schemes it should be at least $\Delta t = 10^{-3}\tau$, while for Lorentz schemes it should be $\Delta t = 10^{-2}\tau$, where τ is a typical medium relaxation time. A numerical experiment with a Debye medium confirms this. We have determined that two of the discretizations for Debye media are totally equivalent. In the Lorentz medium case we establish that the method that uses the polarization differential equation to model dispersion is stable for all wavenumbers, and that the method using the local-in-time constitutive relation is weakly unstable for modes with wavenumber k such that $k\Delta x > \pi/3$.

Keywords—Dispersive media, finite-difference time-domain method, algorithm stability and phase error, RF dosimetry, bioelectromagnetics.

I. INTRODUCTION

THE Computational Electromagnetics community has developed a variety of extensions of the popular FD-TD numerical method [1]-[2] for the modeling of pulse propagation in dispersive media with complex geometry. A representative list of these extensions is [3]-[7]. Some of these extensions append to the Partial Differential Equations (PDEs), that express Maxwell's equations, a set of Ordinary Differential Equations (ODEs) that either describe the local-in-time constitutive relation [3] involving the displacement \vec{D} and the electric field \vec{E} , or the dynamic evolution of the polarization \vec{P} excited by the propagating electric field [4]-[5]. Other popular extensions [6]-[7] use a convolution representation of the constitutive relation which is updated in sync with the time update of the FD-TD discretized PDEs. In the near future we hope to report an analysis of the important convolution integral approach. All the new schemes are useful in studies concerning possible medical effects of human exposure to pulsed electromagnetic fields. This type of application requires the accurate representation of amplitude and phase information for each frequency component in the problem, and commonly involves the execution of thousands of timesteps. Thus, the numerical method of choice should correctly model any energy loss due to physical mechanisms, and it should introduce as little phase error as possible, in addition to being

stable for all possible waves that can be supported on the computational grid.

The stability and phase error properties of the standard FD-TD approach are well known [2]. In sharp contrast, little is known of the numerical error properties of the discretizations of the extensions of FD-TD to dispersive media modeled with ODEs [3]-[5]. Questions that should be answered before such extensions are used in production codes include the following:

- 1) *Is the stability restriction of the FD-TD that is used to model the PDE part of the problem altered by appending the discretized (to second order of accuracy) ODEs that model the material dispersion?*
- 2) *What are the artificial dissipative properties of the composite scheme?*
- 3) *How does the phase error now depend on the discretization parameters?*
- 4) *Are the medium constants (relaxation time, resonance frequency, etc.) altered by the discretization? If so, how?*

We answer these questions by performing a stability and phase error analysis [8] of the coupled PDE-ODE difference system that models one-dimensional pulse propagation in linear dispersive media of Debye [9] and Lorentz [10] type. The analysis is novel, and its purpose is to provide insight to the spurious numerical attributes of FD-TD extensions for dispersive dielectrics. We give many details for the one-dimensional case to bring forward the salient features. In Section IV we show, without detailed derivations and Figures, the stability polynomial and the dispersion relation of the extensions studied herein for two/three-dimensional propagation in Debye and Lorentz dielectrics. In the Discussion section some guidelines will be provided for using the schemes given the medium parameters. The main analysis shows that for accuracy the discretization has to adequately sample the shortest timescale in the problem regardless of whether it is the incident pulse timescale, the medium relaxation timescale, or the medium resonance timescale. The implication of this is that one usually will have to resolve a scale that may be a tenth (usually a hundredth or a thousandth) of that of the incident pulse. Such disparity of scales occurs often in practice where experimental data indicates that typical medium timescales are of $O(10^{-8} - 10^{-12})$ seconds while the duration of pulses of large amplitude (of interest to health and safety analysts) is of the order of hundreds of nanoseconds. Also,

the Courant number should be chosen close to its maximum value for stability so that the phase error is minimum for a given timestep. Another important finding is that the discretization in [3] for a Lorentz medium is weakly unstable for wavenumbers k such that $k\Delta x > \pi/2$. These wavenumbers correspond to unresolved waves (less than 4 cells per wavelength) and numerical noise (grid-scale oscillations). Due to the instability such low-amplitude waves may contaminate well-resolved events in computations encompassing thousands of timesteps, a case typical of computations in dispersive media which usually involve $O(10^4 - 10^5)$ timesteps. The discovered instability will tend to slowly amplify noise instead of producing detectable numerical overflow. The Lorentz scheme in [5] is found to be stable for $0 \leq k\Delta x \leq \pi$, and to slightly damp the range $k\Delta x > \pi/2$ so that the timestepping itself will remove the numerical noise instead of amplifying it.

II. STABILITY ANALYSIS

A. Debye Medium

For brevity we will not include details of derivations since they are quite lengthy. Rather, we will describe any missing steps so the reader can replicate them. Throughout, we assume the reader will refer to the appropriate reference for the relevant physical equations. For the sake of completeness we include the difference schemes for the approaches treated herein.

We begin by considering the scheme presented in [3] for Debye dispersive media. The difference equations for the update of the magnetic, displacement, and electric fields read:

$$\begin{aligned} H_{j+\frac{1}{2}}^{n+\frac{1}{2}} &= H_{j+\frac{1}{2}}^{n-\frac{1}{2}} + \frac{\Delta t}{\mu_o \Delta} (E_{j+1}^n - E_j^n), \\ D_j^{n+1} &= D_j^n + \frac{\Delta t}{\Delta} (H_{j+\frac{1}{2}}^{n+\frac{1}{2}} - H_{j-\frac{1}{2}}^{n+\frac{1}{2}}), \\ E_j^{n+1} &= \frac{\Delta t + 2\tau}{\eta} D_j^{n+1} + \frac{\Delta t - 2\tau}{\eta} D_j^n + \frac{2\tau\epsilon_\infty - \epsilon_s \Delta t}{\eta} E_j^n, \end{aligned} \quad (1)$$

where n is the discrete time index, j is the discrete spatial index, $\eta = 2\tau\epsilon_\infty + \epsilon_s \Delta t$, τ is the medium relaxation time, ϵ_∞ is the infinite frequency permittivity, ϵ_s is the static permittivity, and μ_o is the permeability of the vacuum. Neglecting the effects of boundary conditions and initial conditions a solution of (1) is defined as follows

$$\begin{Bmatrix} H_j^n \\ D_j^n \\ E_j^n \end{Bmatrix} = \begin{Bmatrix} \tilde{h} \\ \tilde{d} \\ \tilde{e} \end{Bmatrix} \xi^n e^{ikj\Delta}. \quad (2)$$

In (2) the complex valued vector $\tilde{\mathbf{x}} = \{\tilde{h}, \tilde{d}, \tilde{e}\}^T$ is the eigenvector of the difference system, ξ is the complex time-eigenvalue we wish to find and whose magnitude will determine the stability and dissipation properties of the difference equations, and k is the real wavenumber of the arbitrary harmonic wave component whose stability and decay

is determined by $|\xi|$. Substituting (2) in (1) we collect the coefficients of the vector $\tilde{\mathbf{x}}$ in the form of a homogeneous linear system $A\tilde{\mathbf{x}} = 0$ where the matrix A involves ξ , the discretization, and the medium parameters. Then we seek non-zero solutions for $\tilde{\mathbf{x}}$ by setting $\det(A) = 0$. Extensive manipulations of the entries in A result in an algebraic polynomial equation for ξ . The polynomial, whose solutions give ξ as a function of the medium parameters, the timestep, and the quantity $k\Delta$ ($= 2\pi/N_{ppw}$, N_{ppw} = points per wavelength), is

$$\begin{aligned} &\xi^3 + \frac{p^2(h+2) - 6\epsilon_\infty - h\epsilon_s}{2\epsilon_\infty + h\epsilon_s} \xi^2 \\ &+ \frac{p^2(h-2) + 6\epsilon_\infty - h\epsilon_s}{2\epsilon_\infty + h\epsilon_s} \xi \\ &- \frac{2\epsilon_\infty - h\epsilon_s}{2\epsilon_\infty + h\epsilon_s} = 0, \end{aligned} \quad (3)$$

where $p = 2\nu \sin \frac{k\Delta}{2}$, $h = \Delta t/\tau$, $\nu = \frac{c_\infty \Delta t}{\Delta}$, and all permittivities are now relative to ϵ_o . The speed c_∞ is the maximum wavespeed in the problem and is given by $c_\infty = c/\sqrt{\epsilon_\infty}$. The speed of light in free-space is c .

Next we considered the scheme presented in [4]. The analysis determines that the two schemes are identical in terms of their stability polynomial and phase error (see Section III.A), provided we make the following identifications and definitions for the medium parameters used in (3) above, i.e., set $\epsilon_\infty = 1$ and $\epsilon_s = 1 + \chi$ where χ is the susceptibility used in [4]. Taking $\tau = 8.1 \times 10^{-12}$ sec, $\epsilon_s = 78.2$, and $\epsilon_\infty = 1$, we calculate numerically with IMSL routines the 3 roots of (3) for a variety of h and Courant numbers ν as functions of $k\Delta$. These medium parameters describe the main relaxation of water in the microwave range of frequencies.

By examining the root of largest magnitude, $\max|\xi|$, as a function of $k\Delta$ in the range $0 \leq k\Delta \leq \pi$ we determined that the difference equations are stable since it was always that $\max|\xi| \leq 1$ for any $k\Delta$ in the range considered as long as $\nu \leq 1$ and h arbitrary. In such a graph the amount of artificial dissipation introduced by the differenced ODEs is evident since it is known that the FD-TD differenced PDEs should always have $|\xi| = 1$ for all $k\Delta$ when $\nu \leq 1$. This is also obtained from (3) by solving for ξ with $h = 0$. The result is shown in Fig. 1 for $\nu = 1$. In the Figure we consider the values $h = 0.1$, $h = 0.01$, and $h = 0.001$ corresponding respectively to a resolution of 10, 100, and 1000 timesteps per relaxation time, τ . It turned out that $\max|\xi| > 1$ (instability) whenever $\nu > 1$ (or $\nu > \sqrt{\epsilon_\infty}$ if $c_\infty < c$) regardless of the medium parameters. Thus, the one-dimensional stability restriction of the standard FD-TD scheme is preserved by both extensions for Debye media. Further, since at a given space-time point the dispersion is the material's memory of past Electric field values, found along the axis of the light-cone extending into the past with vertex at the given spatial point, the stability restriction of the standard FD-TD in two and three dimensions will also be preserved by these schemes. This is because the discrete dispersion variables are appropri-

ately centered with respect to the discrete Electric field so for $0 < \nu \leq 1/\sqrt{\text{dim}}$, where $\text{dim}(= 1, 2, 3)$ is the spatial dimension, the characteristics of the overall scheme are the same as those of the standard FD-TD and include the physical characteristics whose slope is $\pm c_\infty$.

B. Lorentz Medium

For the Lorentz medium case, the schemes of [3] (here called the JHT scheme), and [5] (here called the KF scheme), differ, both in the structure of their difference equations, and in their stability and phase error properties.

We begin with the scheme given in [3] for Lorentz media. The difference equations now are as in (1), above, for $H_{j+\frac{1}{2}}^{n+\frac{1}{2}}$ and D_j^{n+1} , but the electric field update is performed with

$$E_j^{n+1} = \frac{\alpha}{\eta} E_j^n + \frac{\beta}{\eta} E_j^{n-1} + \frac{\gamma}{\eta} D_j^{n+1} + \frac{\zeta}{\eta} D_j^n + \frac{\theta}{\eta} D_j^{n-1}, \quad (4)$$

where now $\eta = \omega_o^2 \Delta t^2 \epsilon_s + 2\delta \Delta t \epsilon_\infty + 2\epsilon_\infty$, the other coefficients being

$$\begin{aligned} \alpha &= 4\epsilon_\infty \\ \beta &= -(\omega_o^2 \Delta t^2 \epsilon_s - 2\delta \Delta t \epsilon_\infty + 2\epsilon_\infty) \\ \gamma &= \omega_o^2 \Delta t^2 + 2\delta \Delta t + 2 \\ \zeta &= -4. \\ \theta &= \omega_o^2 \Delta t^2 - 2\delta \Delta t + 2. \end{aligned} \quad (5)$$

In (5) ω_o is the medium resonance frequency, $\delta = 1/2\tau$ with τ being the relaxation time, and the rest of the parameters are as above for the Debye medium. Substituting (2) into the difference equations we obtain the associated stability polynomial, now of fourth order in ξ because (4) involves an extra level of storage,

$$\xi^4 + \frac{p^2 \gamma' + \alpha'}{\eta} \xi^3 + \frac{p^2 \theta' + \beta'}{\eta} \xi^2 + \frac{p^2 \zeta' + \delta'}{\eta} \xi + \frac{\eta'}{\eta} = 0 \quad (6)$$

with

$$\begin{aligned} \gamma' &= 2 + h_1 + 4\pi^2 h_2^2 \\ \theta' &= -4 \\ \zeta' &= 2 - h_1 + 4\pi^2 h_2^2 \\ \alpha' &= -8\epsilon_\infty - 2h_1\epsilon_\infty - 8\pi^2 h_2^2 \epsilon_s \\ \beta' &= 12\epsilon_\infty + 8\pi^2 h_2^2 \epsilon_s \\ \delta' &= -8\epsilon_\infty + 2h_1\epsilon_\infty - 8\pi^2 h_2^2 \epsilon_s \\ \eta' &= 2\epsilon_\infty - h_1\epsilon_\infty + 4\epsilon_s \pi^2 h_2^2, \end{aligned} \quad (7)$$

where now $h_1 = \Delta t/\tau$, $h_2 = \Delta t/T_o$ ($T_o = 2\pi/\omega_o$), and $\eta = 2\epsilon_\infty + h_1\epsilon_\infty + 4\epsilon_s \pi^2 h_2^2$. The period T_o is that corresponding

to the medium resonant frequency so h_2 is a measure of how well the resonant period of the medium is resolved by the time discretization.

Next, we analyze the scheme of [5]. The difference equations given there are

$$\begin{aligned} H_{j+\frac{1}{2}}^{n+\frac{1}{2}} &= H_{j+\frac{1}{2}}^{n-\frac{1}{2}} + \frac{\Delta t}{\mu_o \Delta} (E_{j+1}^n - E_j^n), \\ E_j^{n+1} + P_j^{n+1}/\epsilon_o &= E_j^n + P_j^n/\epsilon_o \\ &+ \frac{\Delta t}{\Delta} (H_{j+\frac{1}{2}}^{n+\frac{1}{2}} - H_{j-\frac{1}{2}}^{n+\frac{1}{2}}), \\ \chi E_j^{n+1} - \omega_o^2 P_j^{n+1} - \left(\frac{2}{\Delta t} + \gamma''\right) J_j^{n+1} &= -\chi E_j^n \\ &+ \omega_o^2 P_j^n - \left(\frac{2}{\Delta t} - \gamma''\right) J_j^n, \\ P_j^{n+1} - \frac{\Delta t}{2} J_j^{n+1} &= P_j^n + \frac{\Delta t}{2} J_j^n, \end{aligned} \quad (8)$$

where $\chi = \epsilon_o \omega_p^2$, $\gamma'' = 1/\tau$, ϵ_o is the free-space permittivity, and ω_p is the plasma frequency. In terms of the parameter definitions used for the Lorentz scheme of [3] it is that $\omega_p^2 = \omega_o^2(\epsilon_s - 1)$. This scheme is nice for the following reason: The second, third, and fourth difference equations in (8) are implicit in the variables E_j^{n+1} , J_j^{n+1} , P_j^{n+1} , while the first and second are explicit in $H_{j+\frac{1}{2}}^{n+\frac{1}{2}}$, E_j^{n+1} . As a result, the stability properties are independent of the medium time constants, and the Courant restriction for stability of the standard scheme will be retained even in two and three dimensions. The partial implicitness in (8) is not troublesome since the matrix relating E_j^{n+1} , J_j^{n+1} , P_j^{n+1} is inverted just once, except when Δt , χ , ω_o^2 , and τ are functions of time. A solution of (8) is of the form

$$\begin{Bmatrix} H_j^n \\ E_j^n \\ P_j^n \\ J_j^n \end{Bmatrix} = \begin{Bmatrix} \tilde{h} \\ \tilde{e} \\ \tilde{p} \\ \tilde{j} \end{Bmatrix} \xi^n e^{ik_j \Delta}. \quad (9)$$

Substituting (9) in (8) and carrying out the steps indicated above we arrive at the stability polynomial for this scheme

$$\xi^4 + \frac{p^2 \gamma' + \alpha'}{\eta} \xi^3 + \frac{p^2 \theta' + \beta'}{\eta} \xi^2 + \frac{p^2 \zeta' + \delta'}{\eta} \xi + \frac{\eta'}{\eta} = 0 \quad (10)$$

for which now

$$\begin{aligned} \gamma' &= 4 + 2h_1 + 4\pi^2 h_2^2 \\ \theta' &= -8 + 8\pi^2 h_2^2 \\ \zeta' &= 4 - 2h_1 + 4\pi^2 h_2^2 \\ \alpha' &= -16 - 4h_1 \\ \beta' &= 24 - 8\epsilon_s \pi^2 h_2^2 \\ \delta' &= -16 + 4h_1 \\ \eta' &= 4 - 2h_1 + 4\epsilon_s \pi^2 h_2^2, \end{aligned} \quad (11)$$

and $\eta = 4 + 2h_1 + 4\epsilon_s \pi^2 h_1^2$. Equation (10) is of 4th order in ξ not because an additional time level was introduced but because the second order in time ODE for the polarization was transformed to a first order system in accordance with Maxwell equations.

The parameters used in the two approaches considered will address the same physical problem if we set $\chi = \epsilon_o \omega_p^2$, and $\omega_p^2 = \omega_o^2(\epsilon_s - 1)$ for the parameters used in [5] using values for ω_o , τ , ϵ_∞ , and ϵ_s from the numerical example of [3]. With these values we study the 4 roots of the stability polynomials (6) and (10) using the parameter definitions (8) and (11) for each respectively. The values used here are $\tau = 1.786 \times 10^{-16}$ sec, $\epsilon_\infty = 1$, $\epsilon_s = 2.25$, and $\omega_o = 4 \times 10^{16}$ rad/sec. The results are shown in Fig. 3a) for $\nu = 1$ and $h_1 = 0.1$, and in Fig. 3b) for $\nu = 1$ and $h_1 = 0.01$. For the scheme of [5] it is determined that $\max|\xi| > 1$, which corresponds to instability, occurs only when $\nu > 1$ *regardless* of the medium parameters. However, for the scheme of [3] we observe instability for the range $k\Delta > \pi/2$ and some ratios $h_1 = \Delta t/\tau$.

III. PHASE ERROR ANALYSIS

Now we will determine the phase error of each approach considered in the previous section. After proper parameter identifications the modeling approaches of [3] and [4] for Debye media have identical phase error properties. We will consider the following definition of phase error

$$\Phi^{D,L}(\omega\Delta t) = \left| \frac{k_{zz}^{D,L}(\omega) - k_{num}^{D,L}(\omega\Delta t)}{k_{zz}^{D,L}(\omega)} \right| \quad (12)$$

for real ω , where $k_{zz}^{D,L}(\omega)$ is the dispersion relation of the continuous models of Debye (D) and Lorentz (L) media given by

$$k_{zz}^D(\omega) = \frac{\omega}{c} \sqrt{\frac{\epsilon_s}{\tau} - i\omega} \quad (13)$$

$$k_{zz}^L(\omega) = \frac{\omega}{c} \sqrt{\frac{\omega^2 - \omega_o^2 \epsilon_s + 2i\delta\omega}{\omega^2 - \omega_o^2 + 2i\delta\omega}},$$

and $k_{num}^{D,L}(\omega\Delta t)$ will be determined in the subsections below. Note that for both types of media we have set $\epsilon_\infty = \epsilon_o$ so the expressions simplify (also this value is used in the numerical experiments presented in the references). We have used $\omega_p^2 = \omega_o^2 \chi$, $\chi = \epsilon_s - 1$, and $2\delta = 1/\tau$ to relate the Lorentz mediums of [3] and [5]. The ω range considered is such that $0 \leq \omega\Delta t \leq \pi$ given Δt . The spatial step Δ is determined from Δt and ν .

A. Debye Medium

Only the scheme of [3] will be considered since it is identical to that of [4] for $\epsilon_\infty = \epsilon_o$. To determine the numerical dispersion relation we now substitute

$$\begin{Bmatrix} H_j^n \\ D_j^n \\ E_j^n \end{Bmatrix} = \begin{Bmatrix} \tilde{h} \\ \tilde{d} \\ \tilde{e} \end{Bmatrix} e^{i(k_{num}^D j \Delta - \omega n \Delta t)}, \quad (14)$$

in the difference equations (1), with $(\tilde{h}, \tilde{d}, \tilde{e})^T$ being an arbitrary complex vector, and manipulate the result so that again we obtain a homogeneous linear system whose determinant of the coefficient matrix we demand to vanish. The dependence of k_{num}^D on the frequency ω and on the various medium and discretization parameters is thus obtained. The result is

$$k_{num}^D(\omega\Delta t) = \frac{2}{\Delta} \sin^{-1} \left[\frac{\omega}{c} \frac{\Delta}{2} s_\omega \sqrt{\frac{\epsilon_s}{\tau} \cos \frac{\omega\Delta t}{2} - i\omega s_\omega} \right], \quad (15)$$

where $s_\omega = \frac{\sin \omega\Delta t/2}{\omega\Delta t/2}$. By inspecting (15), and comparing it to k_{zz}^D given above, two features emerge that are solely due to the discretization of the ODE involved. The relaxation time τ of the medium is now $\tau_{num} = \frac{\tau}{\cos(\omega\Delta t/2)}$, i.e., the medium actually modeled by the numerics is one with *higher* relaxation time constant. This is the source of the artificial dissipation exhibited by the maximum root, $\max|\xi|$, of (3). Further, since $\cos(\omega\Delta t/2) \rightarrow 0$ for $\omega \rightarrow \pi/\Delta t$, we infer that the corresponding frequency component will be adversely affected by the scheme since it will experience a medium of unphysically high constant conductivity equal to $\epsilon_o(\epsilon_s - 1)/\tau_{num}$. Such artificial dissipation can be controlled by choosing Δt so that $\cos \omega\Delta t/2 \sim 1$ across the range of frequencies present in the short-pulse that propagates in the medium. For $\nu = 1$, Fig. 2 shows the dependence of the phase error (12) on the number of timesteps per relaxation time, $h = \Delta t/\tau$, as a function of $\omega\Delta t$.

B. Lorentz Medium

For the scheme in [3] pertaining to Lorentz media, we follow the same procedure as with the Debye medium but now the third difference equation in (1) is replaced with (4). Using (14) we obtain for the numerical dispersion relation k_{num}^L ,

$$k_{num}^L(\omega\Delta t) = \frac{2}{\Delta} \sin^{-1} \left\{ \frac{\omega}{c} \frac{\Delta}{2} s_\omega \sqrt{\frac{\omega^2 s_\omega^2 - \epsilon_s \omega_o^2 \cos \omega\Delta t + i\delta\omega \frac{\sin \omega\Delta t}{\omega\Delta t/2}}{\omega^2 s_\omega^2 - \omega_o^2 \cos \omega\Delta t + i\delta\omega \frac{\sin \omega\Delta t}{\omega\Delta t/2}}} \right\}. \quad (16)$$

Equation (16) shows how this extension of FD-TD misrepresents the relaxation time by enforcing $\tau_{num} = \frac{\tau \sin(\omega\Delta t/2)}{\sin(\omega\Delta t)}$, and the resonance frequency of the medium by enforcing $\omega_{num}^o = \omega_o \sqrt{\cos(\omega\Delta t)}$.

Next, we determine the phase error of the scheme in [5]. Substituting

$$\begin{Bmatrix} H_j^n \\ E_j^n \\ P_j^n \\ J_j^n \end{Bmatrix} = \begin{Bmatrix} \tilde{h} \\ \tilde{e} \\ \tilde{p} \\ \tilde{j} \end{Bmatrix} e^{i(k_{num}^L j \Delta - \omega n \Delta t)} \quad (17)$$

in the difference equations (10) we obtain the dispersion relation

$$k_{num}^L(\omega\Delta t) = \frac{2}{\Delta} \sin^{-1} \left[\frac{\omega}{c} \frac{\Delta}{2} s_\omega \right]$$

$$\sqrt{\frac{\omega^2 s_\omega^2 - \epsilon_\infty \omega_0^2 \cos^2 \frac{\omega \Delta t}{2} + 2i\delta \cos \frac{\omega \Delta t}{2} \omega s_\omega}{\omega^2 s_\omega^2 - \omega_0^2 \cos^2 \frac{\omega \Delta t}{2} + 2i\delta \cos \frac{\omega \Delta t}{2} \omega s_\omega}}, \quad (18)$$

now for γ of [5] equal to 2δ (δ is used in [3]). From (18) we see that this approach also misrepresents the relaxation time by enforcing $\tau_{num} = \frac{\tau}{\cos(\omega \Delta t/2)}$ which is the same as the misrepresentation in the Debye medium case. The numerical resonance frequency of the medium is now $\omega_{num}^D = \omega_0 \cos(\omega \Delta t/2)$.

Phase error comparisons between the two approaches using (12) are shown in Figs. 4a) and 4b) for $\nu = 1$, and ratios $h_1 = \Delta t/\tau = 0.1$ and 0.01 respectively.

IV. 2/3 DIMENSIONAL EXTENSIONS

Herein we assume the reader is familiar with the two dimensional Transverse Magnetic polarization formulation of the standard FD-TD [1]. The unknown two-dimensional fields are H_x , H_y , D_x , E_x . The discretized dispersion ODE of all schemes is unchanged in higher dimensions. We set $\Delta x = \Delta y = \Delta$.

To determine the stability for the Debye extension of the scheme of [3] we proceed as in Section II.A. The difference equations now reflect the existence of the extra fields and the two spatial variables. Accordingly, (2) is extended as follows

$$\begin{Bmatrix} H_x^n(j, m) \\ H_y^n(j, m) \\ D_x^n(j, m) \\ E_x^n(j, m) \end{Bmatrix} = \begin{Bmatrix} \tilde{h}_x \\ \tilde{h}_y \\ \tilde{d}_x \\ \tilde{e}_x \end{Bmatrix} \xi^n e^{i(jk \cos \theta + mk \sin \theta)\Delta}, \quad (19)$$

where (j, m) are the discrete spatial indices, $k = \sqrt{k_x^2 + k_y^2}$ is the wavenumber magnitude, and θ is the angle of propagation with respect to the grid x -axis. Equation (3) becomes

$$\begin{aligned} & \xi^4 + \frac{p^2(2+h) - 8\epsilon_\infty - 2h\epsilon_s}{2\epsilon_\infty + h\epsilon_s} \xi^3 + \frac{12\epsilon_\infty - 4p^2}{2\epsilon_\infty + h\epsilon_s} \xi^2 \\ & + \frac{p^2(2-h) - 8\epsilon_\infty + 2h\epsilon_s}{2\epsilon_\infty + h\epsilon_s} \xi \\ & + \frac{2\epsilon_\infty - h\epsilon_s}{2\epsilon_\infty + h\epsilon_s} = 0, \end{aligned} \quad (20)$$

where now $p^2 = 4\nu^2(\sin^2 \rho + \sin^2 \zeta)$, $\rho = k \cos \theta(\Delta/2)$, and $\zeta = k \sin \theta(\Delta/2)$. The numerical dispersion relation is obtained by using

$$\begin{Bmatrix} H_x^n(j, m) \\ H_y^n(j, m) \\ D_x^n(j, m) \\ E_x^n(j, m) \end{Bmatrix} = \begin{Bmatrix} \tilde{h}_x \\ \tilde{h}_y \\ \tilde{d}_x \\ \tilde{e}_x \end{Bmatrix} e^{i[(jk_{num}^D \cos \theta + mk_{num}^D \sin \theta)\Delta - \omega n \Delta t]} \quad (21)$$

in the difference equations and proceeding as in one dimension. After performing the calculations we find that the dispersion relation for real frequency ω is

$$\sin^2 \rho(\omega, \theta, \Delta) + \sin^2 \zeta(\omega, \theta, \Delta) = \frac{\Delta^2 \omega^2}{4 c^2} s_\omega^2 \left[\frac{\epsilon_s \cos \frac{\omega \Delta t}{2} - i\epsilon_\infty \omega s_\omega}{\frac{1}{\tau} \cos \frac{\omega \Delta t}{2} - i\omega s_\omega} \right], \quad (22)$$

where $\rho = k_{num}^D(\omega \Delta t) \cos \theta(\Delta/2)$, $\zeta = k_{num}^D(\omega \Delta t) \sin \theta(\Delta/2)$. Again, for $\epsilon_\infty = 1$ the two-dimensional extension of the Debye scheme of [4] is again identical to that of [3].

The stability of the Lorentz scheme of [5] can be addressed with the discussions in the end of Section II.A and below equation (8). The relevant polynomial for the Lorentz scheme of [3] is

$$\begin{aligned} & \xi^5 + \frac{p^2 \gamma - 3 - \alpha}{\eta} \xi^4 + \frac{p^2(\zeta - \gamma) + 3 + 3\alpha - \beta}{\eta} \xi^3 \\ & + \frac{p^2(\theta - \zeta) - 1 - 3\alpha + 3\beta}{\eta} \xi^2 \\ & + \frac{\alpha - 3\beta - \theta p^2}{\eta} \xi + \frac{\beta}{\eta} = 0, \end{aligned} \quad (23)$$

and the various symbol definitions can all be found in equations (4) and (5). In (23) p^2 is the same as for equation (20). The numerical dispersion relations for all the Lorentz medium schemes are easily obtained from equations (16) and (18) by inspection considering that dispersion is a temporal phenomenon and does not enter in geometrical considerations. As a result, the two-dimensional dispersion relations are

$$\sin^2 \rho(\omega, \theta, \Delta) + \sin^2 \zeta(\omega, \theta, \Delta) = A^2, \quad (24)$$

where A is the argument of the \sin^{-1} function in (16) and (18), and ρ and ζ are defined as for (22) but with k_{num}^L replacing k_{num}^D . Notice that (22) can also be derived in the same way with A now being the argument of the \sin^{-1} function in (15).

In three dimensions the dispersion relation for all schemes (Debye and Lorentz) considered herein will be

$$\begin{aligned} & \sin^2 \rho(\omega, \theta, \psi, \Delta) + \sin^2 \zeta(\omega, \theta, \psi, \Delta) \\ & + \sin^2 \pi(\omega, \theta, \psi, \Delta) = A^2. \end{aligned} \quad (25)$$

In (25), A is as above, $\rho = k_{num}^{D,L}(\omega \Delta t) \cos \theta \sin \psi(\Delta/2)$, $\zeta = k_{num}^{D,L}(\omega \Delta t) \sin \theta \sin \psi(\Delta/2)$, $\pi = k_{num}^{D,L}(\omega \Delta t) \cos \psi(\Delta/2)$, with ψ being the angle of propagation of the harmonic wave with respect to the z -axis and now θ being the angle between the grid x -axis and the projection of the wavevector, $\vec{k}_{num}^{D,L}(\omega \Delta t) = \hat{x}k_x^{D,L} + \hat{y}k_y^{D,L} + \hat{z}k_z^{D,L}$, on the $x-y$ plane.

V. DISCUSSION

The finite difference approaches of [3] and [4] for Debye media have been determined to be equivalent in any number of dimensions. Therefore, we studied the stability polynomial (3) and the phase error (15), obtained for the scheme

of [3] in one dimension. Fig. 1 shows the magnitude of the largest of the 3 roots of the stability polynomial as a function of the product $k\Delta$, which may be thought of as wavenumber if Δ is fixed, or as inverse of points per wavelength (equivalently, as Δ) if k is viewed as fixed. While the Figure shows all roots to be inside the unit circle (hence the scheme to be stable), it also indicates that the difference equations are now spuriously dissipative. This is in contrast to the case where FD-TD solves Maxwell's equations in free-space (the solid line in these Figures), or when the dispersion ODEs are solved separately from Maxwell's equations, i.e., set $h = 0$ in (3) and solve for the roots. It turned out that for $\nu \leq 1$ it was $\max|\xi| \leq 1$ always, and that $\max|\xi| > 1$ only for $\nu > 1$. Therefore these extensions of FD-TD for Debye media preserve the stability restriction of the standard FD-TD scheme in non-dispersive dielectrics. The graph also shows that the artificial dissipation is strongly dependent on the quantity h . We see that h has to be sufficiently small so that not much energy is lost after the large amount of timesteps usually needed to propagate short pulses any appreciable distance into a medium. One guideline for a user would be that the timestep chosen must be at least of $O(10^{-3}\tau)$, where τ is the relaxation time in the Debye medium, or the smallest relaxation time in a medium modeled with multiple Debye relaxation mechanisms. In Fig. 2 the phase error (12) is graphed as a function of $\omega\Delta t$ for the same three values of h . The horizontal axis again has a triple interpretation, i.e., frequency, timestep, or points per period. Again, we see that $\Delta t \sim O(10^{-3}\tau)$ is optimal. In both Figures $\nu = 1$, i.e., the maximum Courant number for stability. It turned out that if $\nu < 1$ then, for a fixed accuracy, the timestep restriction with regard to the relaxation time is more severe, thus another guideline is that these schemes should be run close to their Courant stability limit, and this will result in minimal run time since the timestep will then be optimally maximum. One must point out that these results do not depend on the points per wavelength used to sample the incident/propagating pulse. If the pulse duration is longer than the relaxation time, one must still maintain a sampling rate that resolves the shortest timescale, which is the relaxation time in this case. If the incident pulse duration is shorter than τ one decides on the sampling in the usual way as long as $h = 10^{-3}$.

Figs. 3a) and 3b) are concerned with stability comparisons of the JHT scheme and the KF scheme, for Lorentz media. We see that the JHT scheme is unstable ($\max|\xi| > 1$) for $k\Delta > \pi/2$ at $\nu = 1$ if h_1 is not chosen correctly, whereas the standard FD-TD and the KF scheme are stable for all wavenumbers. It turns out that the JHT extension has a stability limit that is more restrictive than that of FD-TD in non-dispersive dielectrics. Reducing h_1 to at least 10^{-2} stabilizes the scheme. We attribute this instability to incorrect time centering of the local-in-time constitutive relation with respect to the time centering of the discretized PDEs. From the difference equation (4) for the constitutive relation it is seen that dD/dt , d^2D/dt^2 are centered at the n -th timestep while in the Maxwell's equa-

tions discretization dD/dt is centered at the $n + \frac{1}{2}$ timestep. This is also indicated by the presence of sinusoidal factors with argument $\omega\Delta t$ and $\omega\Delta t/2$ in the dispersion relation for the scheme (16). On the other hand, the KF scheme centers the ODE part correctly and does not exhibit this instability. The phase error of the two Lorentz schemes are shown in Figs. 4a) and 4b) for $\nu = 1$ and two values of h_1 . Running the schemes with $\nu < 1$ is again discouraged. For these schemes we notice that it is enough to choose $\Delta t \sim O(10^{-2}\tau)$, where $\tau = 1/(2\delta)$. Note that the KF scheme exhibits consistently less phase error than the JHT scheme. We have not investigated the effect of varying h_2 since for the numerical values of the medium parameters used here, $\tau \sim T_0$.

In Section IV we presented the stability polynomials of the Debye medium schemes and of the weakly unstable Lorentz scheme of [3] for two-dimensional TM propagation. All schemes that correctly center the dispersion variables preserve the known stability restriction of the standard FD-TD in higher dimensions. Numerically solving for the roots of these polynomials and determining the largest root, as a function of the discretization parameters for each angle of propagation of the harmonic wave given the medium parameters, one can easily ascertain the degree of decay each mode will sustain and thus will be guided towards the selection of optimum parameters. The Debye schemes and the Lorentz scheme of [5] are stable for $\nu \leq 1/\sqrt{2}$ regardless of the value of h , or h_1 . The Lorentz scheme of [3] is again weakly unstable. The dispersion relations of all schemes are easy to deduce in higher dimensions, once their one-dimensional form is known. We give all dispersion relations in two and three dimensions. Now the wavenumber cannot be explicitly determined as a function of the real frequency ω . An iterative scheme must be used to calculate $k_{num}^{D,L}$ for each ω , θ , ψ , given the medium parameters, using the non-dispersive value $\omega\sqrt{\epsilon_\infty}/c$ as a starting value.

Finally, we simulated the propagation of a 1 nanosecond duration square-modulated sine wave with carrier frequency at 10 GHz normally incident on a Debye medium ($\epsilon_s = 80.35$, $\epsilon_\infty = 1.0$, $\tau = 8.13$ picoseconds) half-space from the air side. Six runs were made with a code written from reference [3]. The timestep was successively halved (starting with $h \sim 0.05$) by halving h for fixed τ and $\nu = 1$. A time trace of the electric field at a depth of 10 mm was recorded with a window of 2 nanoseconds. The number of timesteps executed in each run was $2 \times 10^{-9}/\Delta t \sim O(10^3 - 10^5)$. Fig. 5 shows the time traces from the first three runs and how they converge with the reduction of the timestep. Further reduction shows that the timestep for which $h = 0.00615$ is adequate for a converged result. In Fig. 6, the $h = 0.00615$ result is indistinguishable from the $h = 0.003075$ result. Graphs of the dissipation and phase errors (not shown here) reflect the fact that, in terms of numerical errors, the computed results should not change much with further timestep reduction past the value for which $h = 0.00615$. With only this information we could have avoided the six convergence runs. The guideline $\Delta t \sim O(10^{-3}\tau)$ is confirmed.

VI. SUMMARY

In this paper we have analyzed four FD-TD based schemes for modeling pulse propagation in dispersive media of Debye and Lorentz type. The medium dispersion is described by ODEs representing the local-in-time constitutive relation [3], or the dynamic equation for the polarization evolution driven by the electric field [4]-[5]. We found that the extensions considered here do not preserve the non-dissipative character of the standard FD-TD which is good for tracking individual frequency components for a large amount of timesteps, and that the ease of limiting artificial dispersion is lost since now there are more parameters, in addition to ν , that control it. The overall difference systems are more dispersive than the standard FD-TD, and their accuracy depends strongly on how well the chosen timestep resolves the shortest timescales. All parameters which play a major role in the elimination of artificial dissipation and phase error for these schemes have been identified. The higher dimensional form of our results has also been given.

development of numerical and analytical approaches for modeling time-domain propagation and scattering in dispersive dielectric media. Dr. Petropoulos is a member of Tau Beta Pi, Eta Kappa Nu, Sigma Xi, and SIAM.

REFERENCES

- [1] K.S. Yee, "Numerical Solution of Initial Boundary Value Problems Involving Maxwell's Equations in Isotropic Media," *IEEE Trans. Antennas Propagat.*, vol. 14, pp. 302-306, 1966.
- [2] A. Taflov and K.R. Umashankar, "The Finite-Difference Time-Domain (FD-TD) Method for Electromagnetic Scattering and Interaction Problems," *J. Electromag. Wav. Appl.*, vol. 1, no. 3, pp. 243-267, 1987.
- [3] R.M. Joseph, S.C. Hagness and A. Taflov, "Direct Time Integration of Maxwell's Equations in Linear Dispersive Media with Absorption for Scattering and Propagation of Femtosecond Electromagnetic Pulses," *Optics Lett.*, vol. 16, no. 18, pp. 1412-1414, 1991.
- [4] T. Kashiwa, N. Yoshida and I. Fukai, "A Treatment by the Finite-Difference Time-Domain Method of the Dispersive Characteristics Associated with Orientation Polarization," *IEICE Transactions*, vol. E73, no. 8, pp. 1328-1328, 1990.
- [5] T. Kashiwa and I. Fukai, "A Treatment by the FD-TD Method of the Dispersive Characteristics Associated with Electronic Polarization," *Microw. Optic. Tech. Lett.*, vol. 3, no. 6, pp. 203-205, 1990.
- [6] D. H. Lam, "Finite Difference Methods for Transient Signal Propagation in Stratified Dispersive Media," *PhD Thesis*, Ohio State University, 1974.
- [7] R. Luebbers, F.P. Hunsberger, K.S. Kunz, R.B. Standler and M. Schneider, "A Frequency-Dependent Finite-Difference Time-Domain Formulation for Dispersive Materials," *IEEE Trans. Electrom. Compat.*, vol. 32, no. 3, pp. 222-227, 1990.
- [8] J.C. Strikwerda, *Finite Difference Schemes and Partial Differential Equations*, Pacific Grove CA: Wadsworth and Brooks/Cole (1989).
- [9] P. Debye, *Polar Molecules*, New York: Dover (1929).
- [10] J. D. Jackson, *Classical Electrodynamics*, 2nd ed. New York: Wiley (1975).

Peter G. Petropoulos received the B.Sc. degree with Highest Honors in Electrical Engineering from Rutgers University, New Brunswick, NJ, in 1986, and the M.Sc. and Ph.D. degrees in Applied Mathematics from Northwestern University, Evanston, IL, in 1988 and 1991 respectively. In 1991 he joined the USAF Armstrong Laboratory, Brooks AFB, TX, where he has been an HSC Scholar working on the

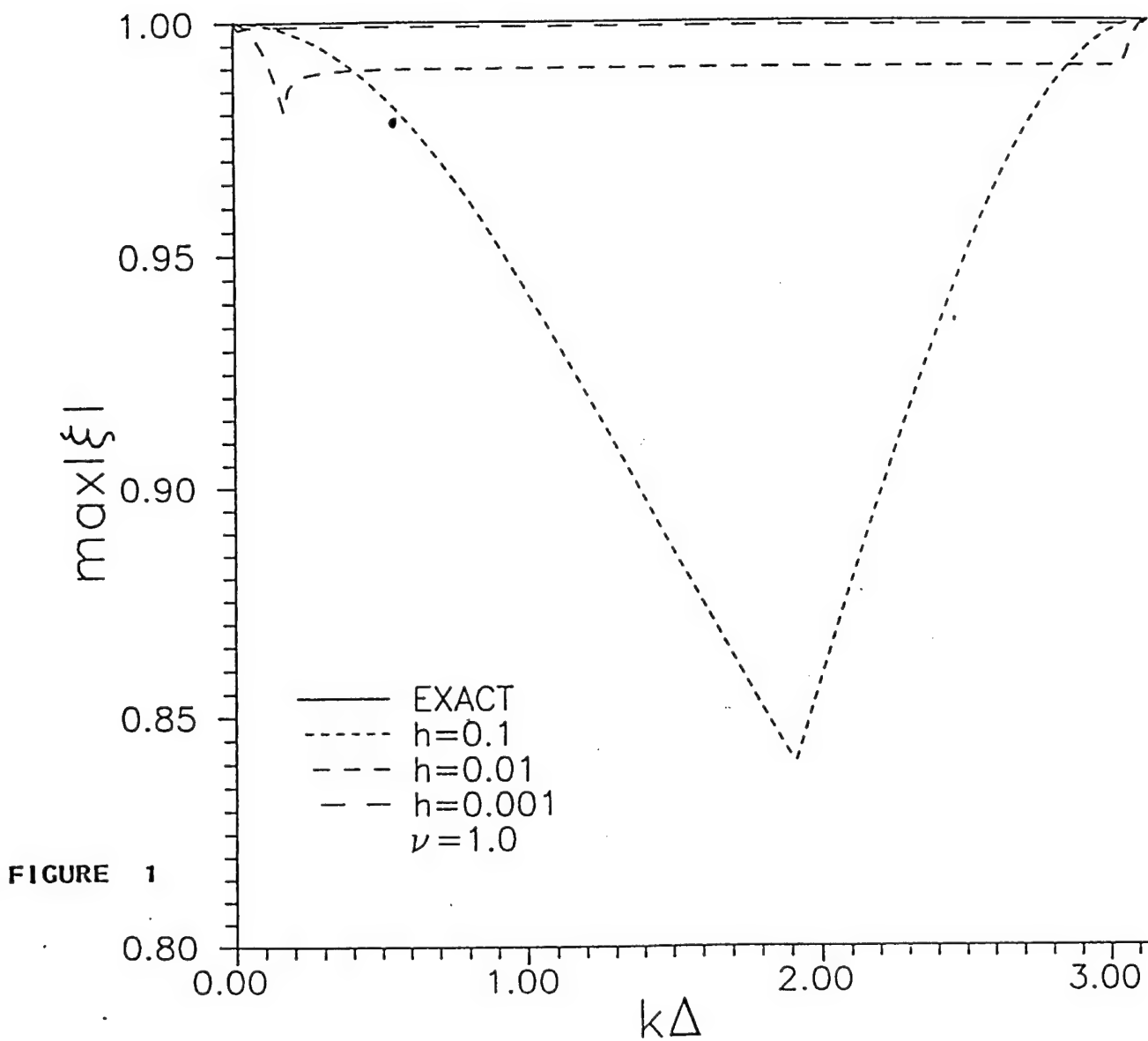
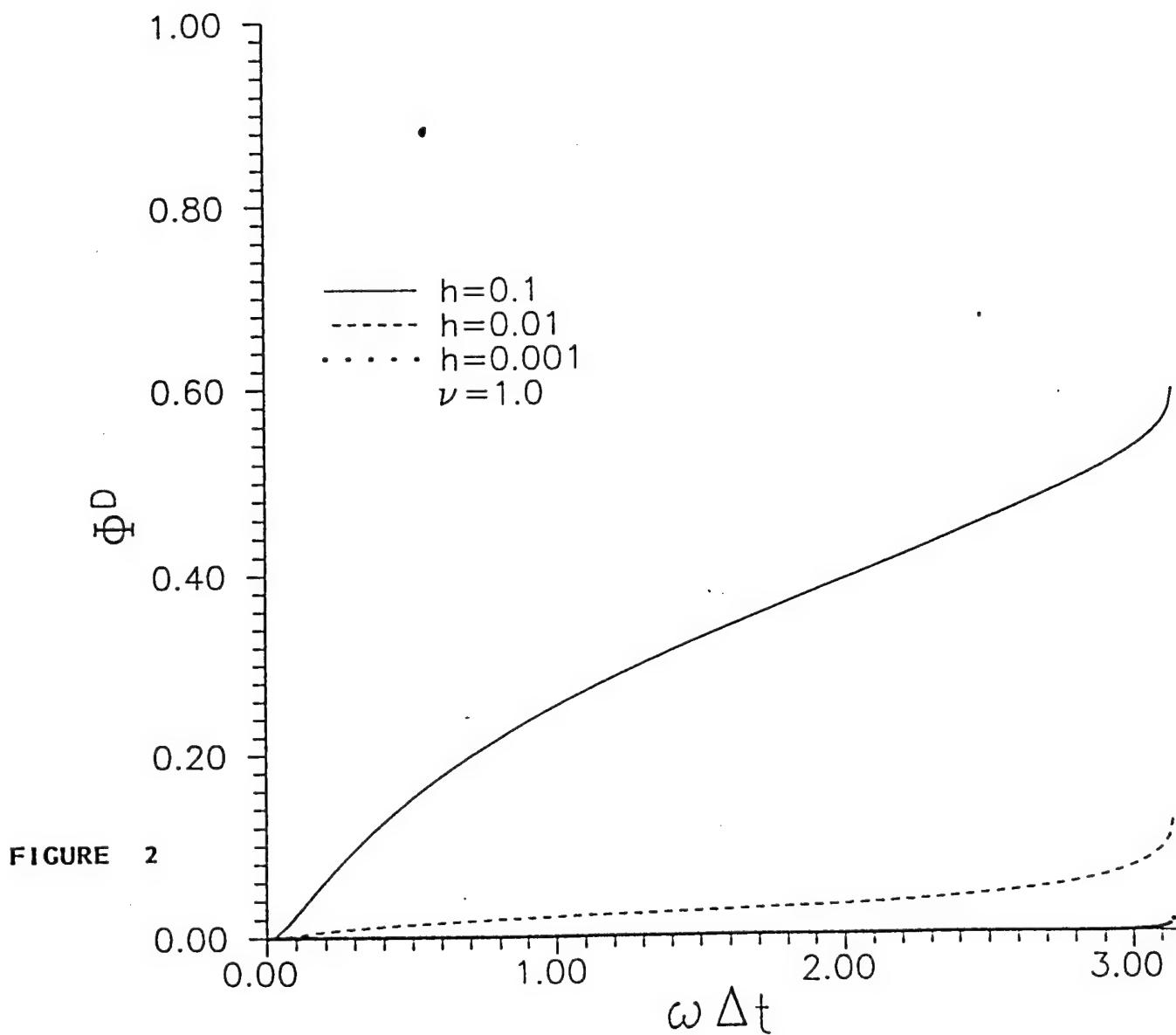
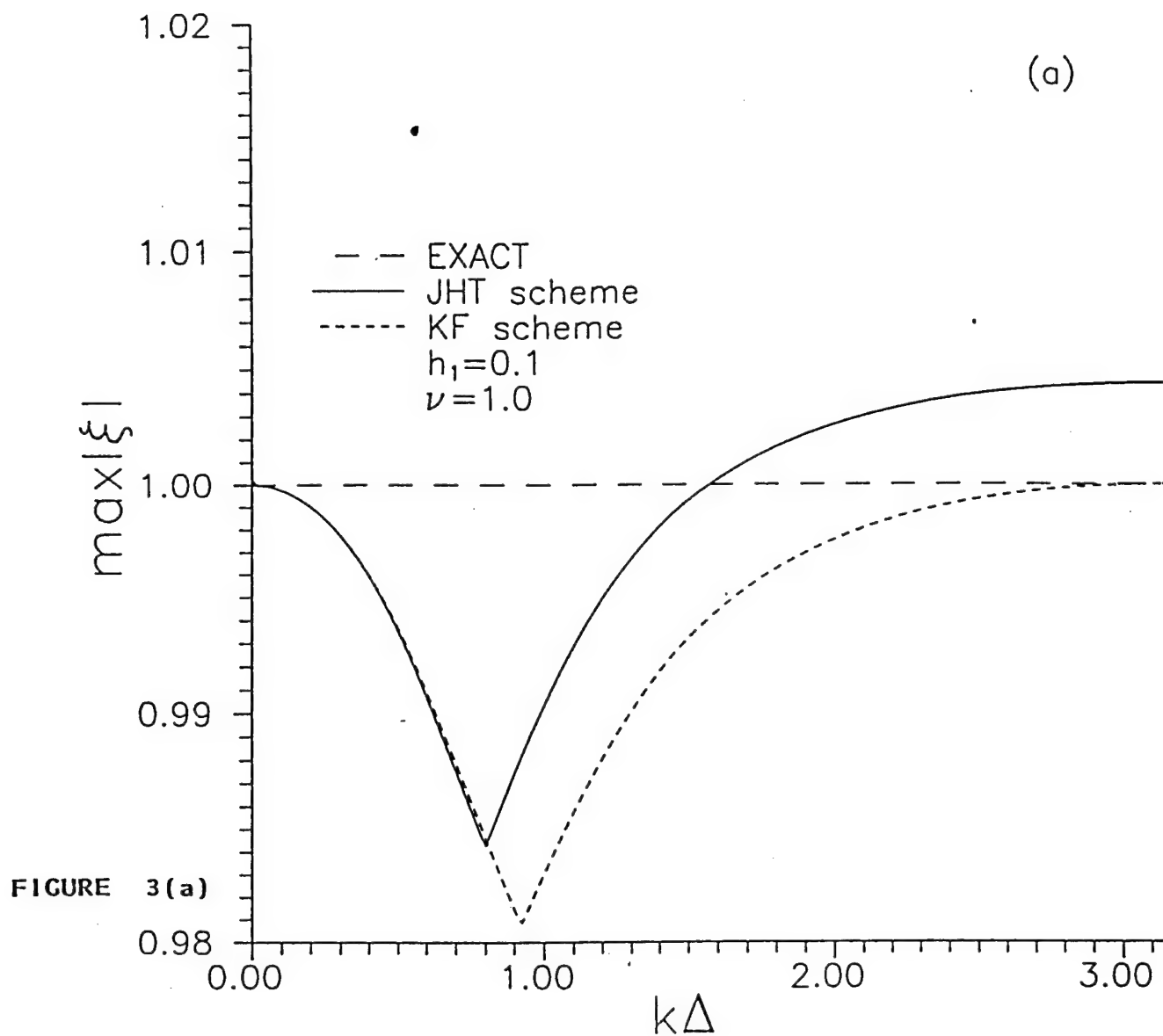


FIGURE 1

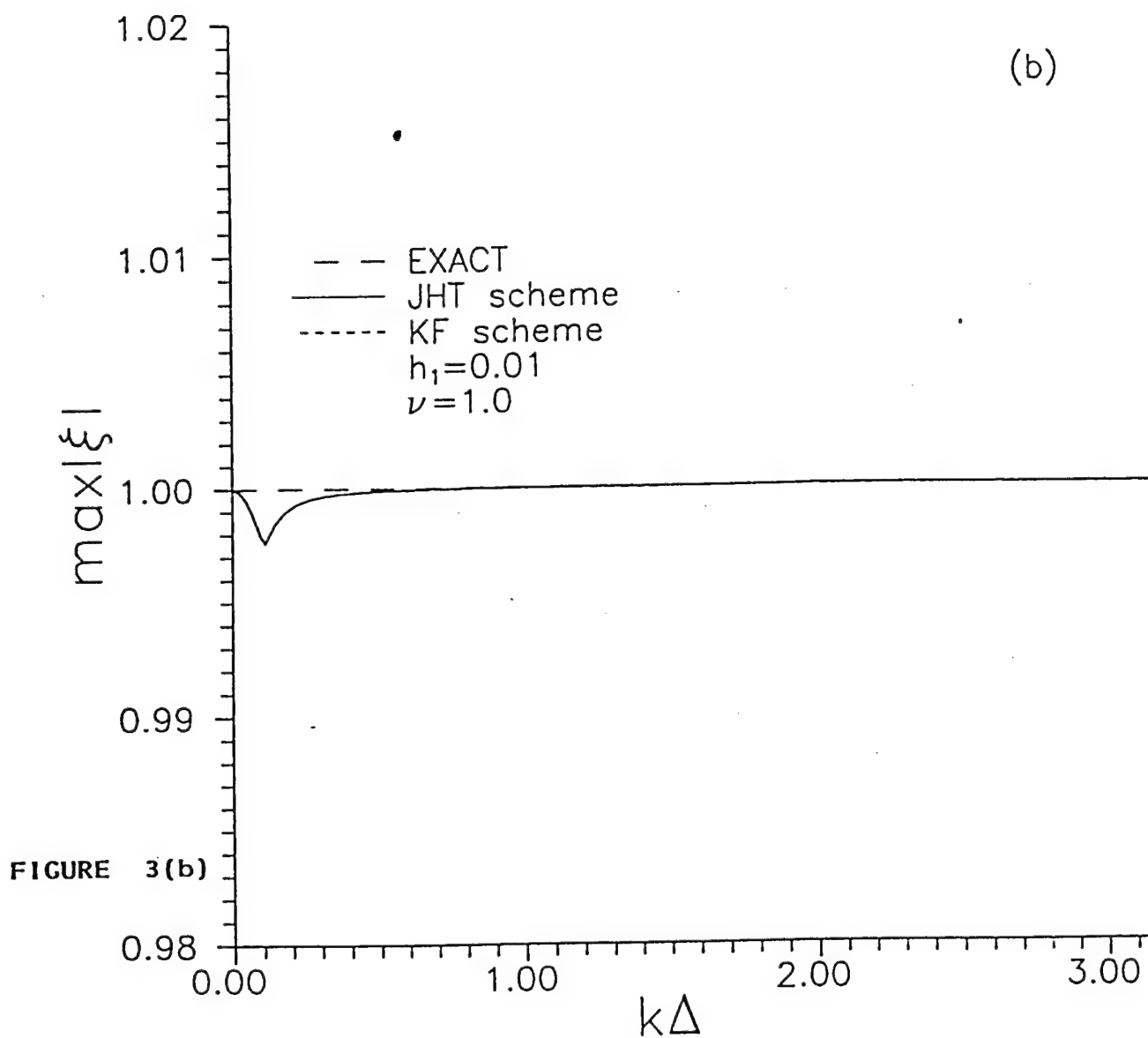
1. The maximum stability eigenvalue of the Debye medium difference schemes versus $k\Delta (= 2\pi/N_{ppw})$ for $\nu = c_{\infty}\Delta t/\Delta = 1.0$.



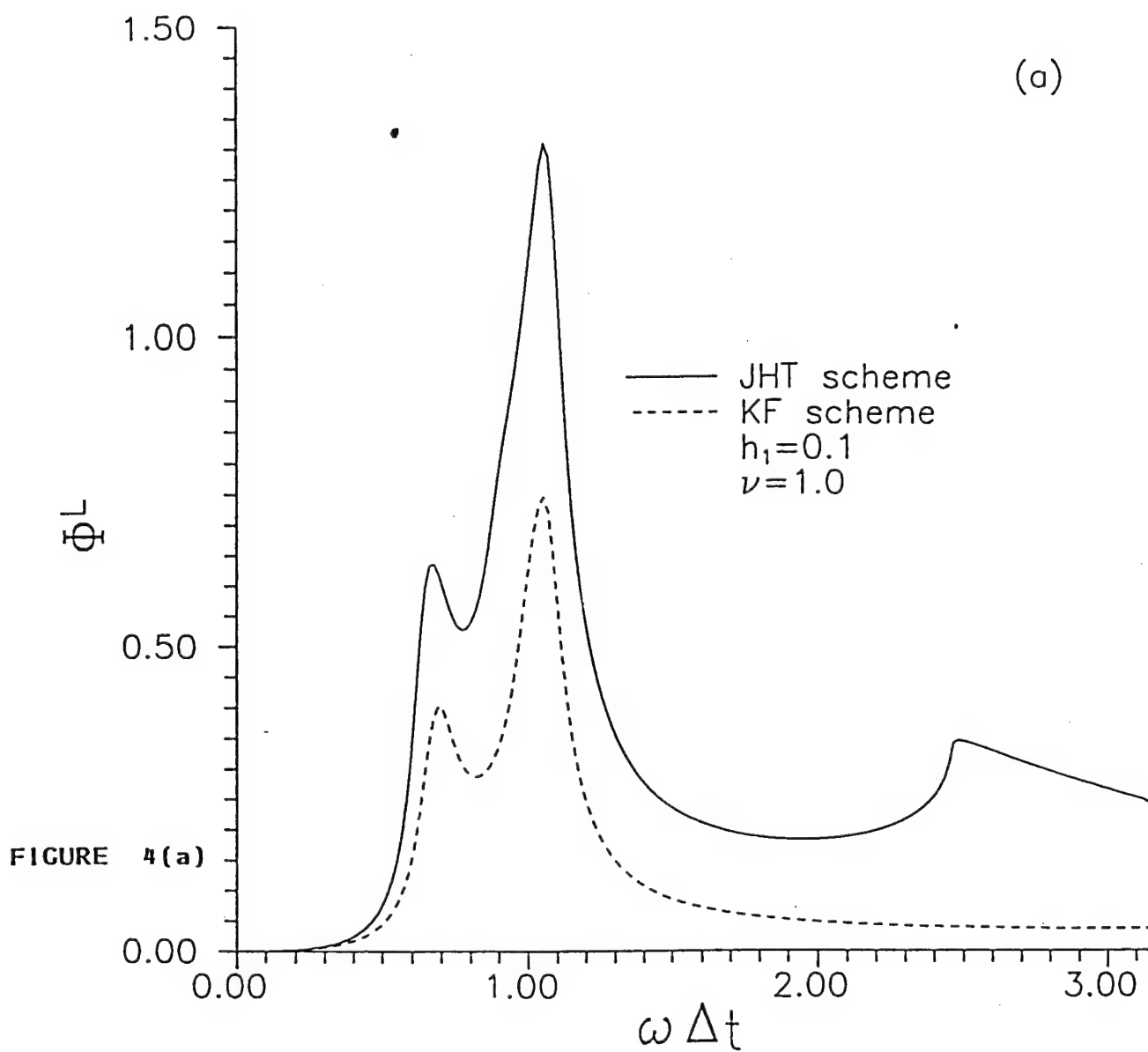
2. Phase error for the Debye medium difference schemes versus $\omega \Delta t$ for $\nu = 1.0$.



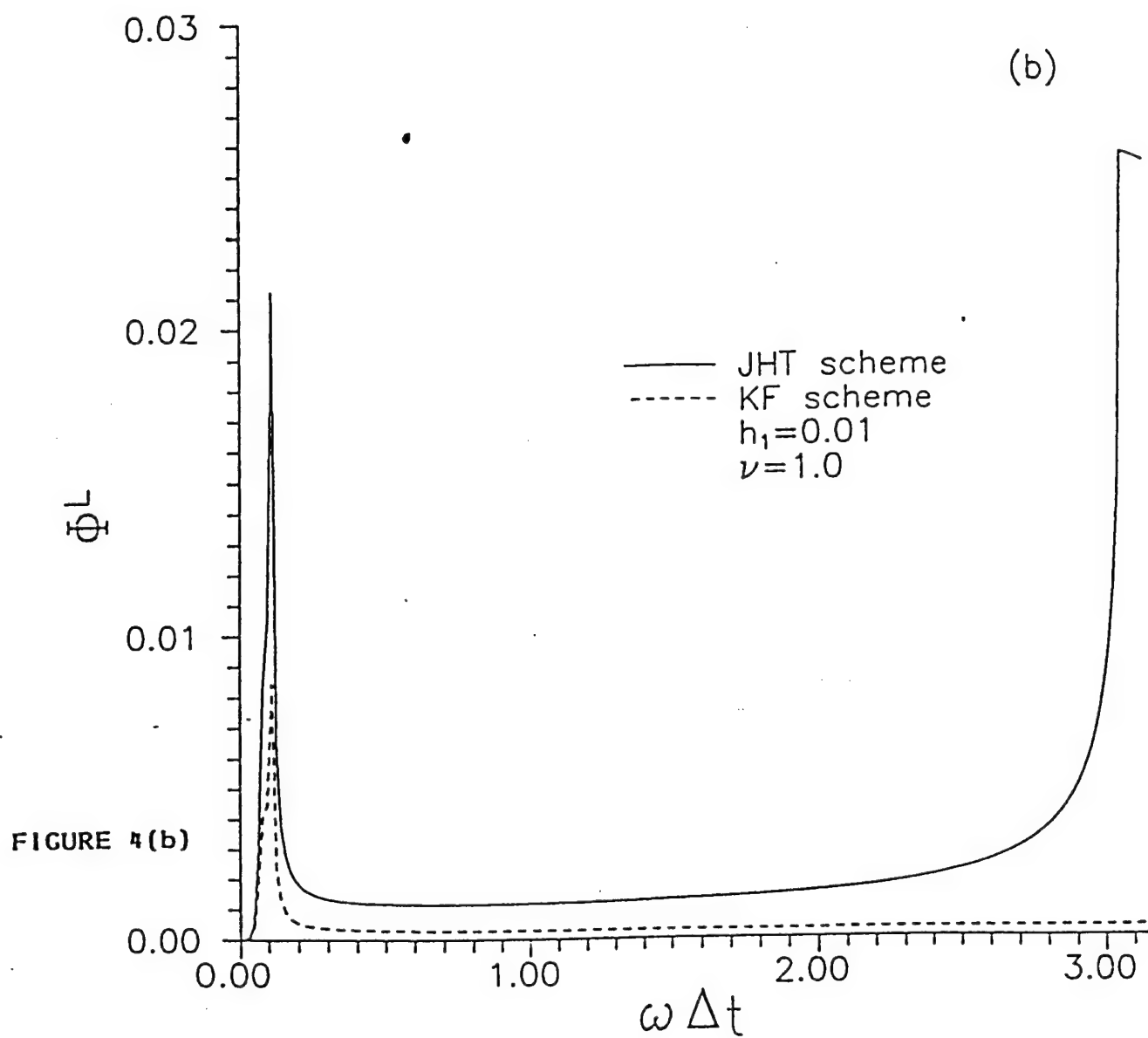
3. Comparison of the stability eigenvalues of the JHT and KF Lorentz medium difference schemes for a) $h_1 = 0.1$, and b) $h_1 = 0.01$.



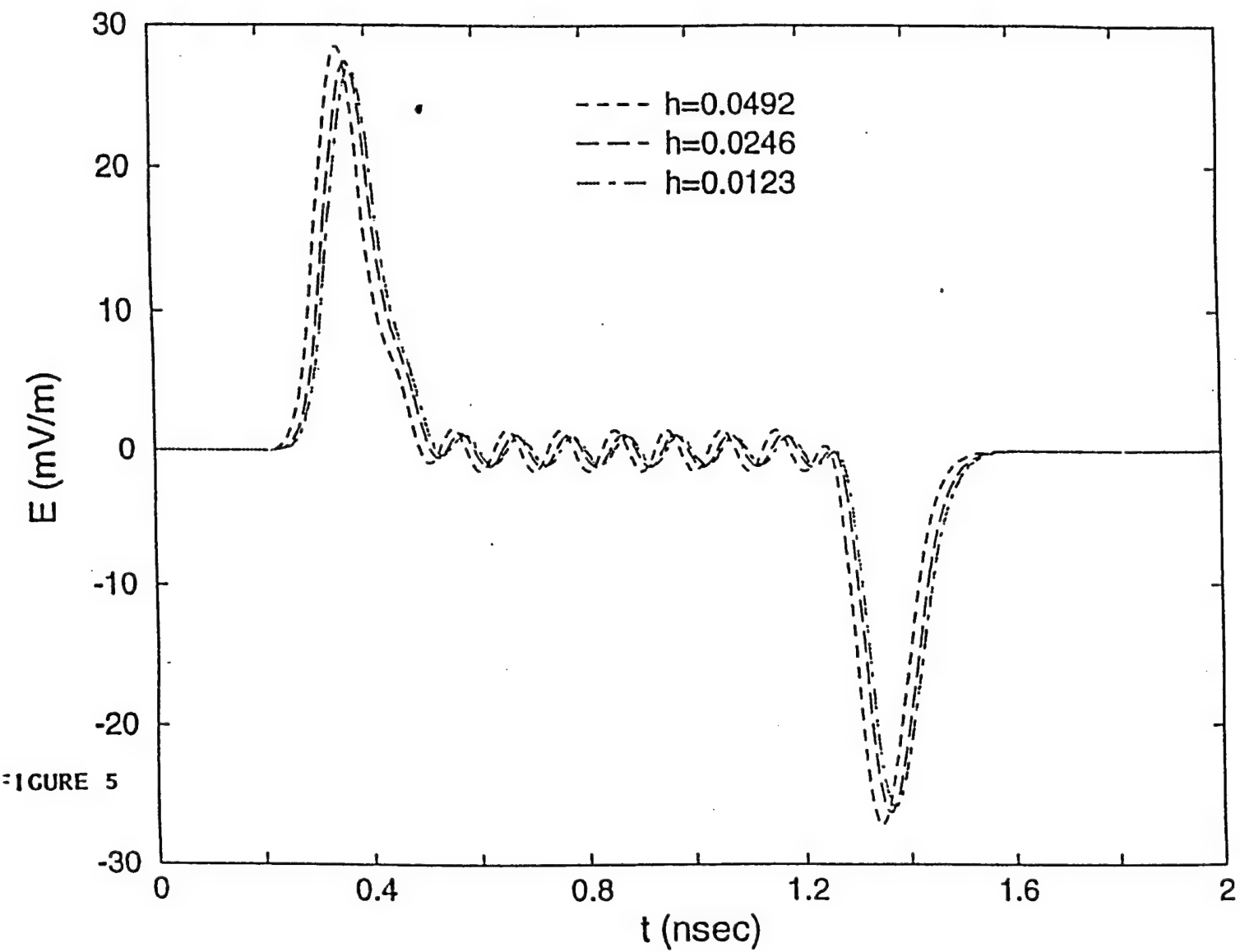
3. Comparison of the stability eigenvalues of the JHT and KF Lorentz medium difference schemes for a) $h_1 = 0.1$, and b) $h_1 = 0.01$.



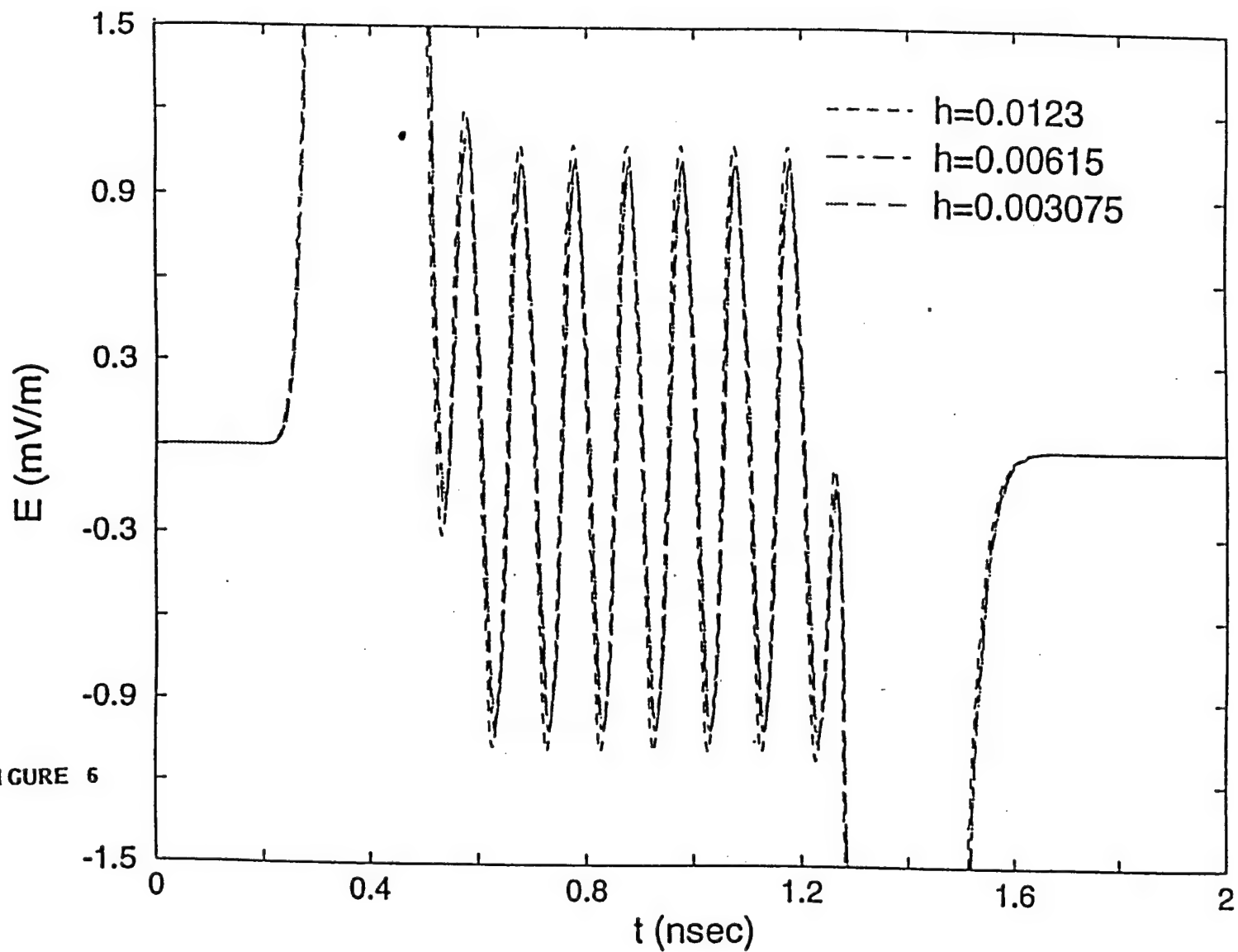
4. Comparison of the phase errors attained by the JHT and KF Lorentz medium difference schemes for a) $h_1 = 0.1$, and b) $h_1 = 0.01$. Note the difference in scales between the two Figures.



4. Comparison of the phase errors attained by the JHT and KF Lorentz medium difference schemes for a) $h_1 = 0.1$, and b) $h_1 = 0.01$. Note the difference in scales between the two Figures.



5. Electric field computed with FD-TD for Debye medium as a function of $h = \Delta t/\tau$.



6. Same as Fig. 5 for further reduction of h . Convergence is achieved at $h = 0.00615$.

THIS PAGE INTENTIONALLY LEFT BLANK

The Wave Hierarchy for Propagation in Relaxing Dielectrics

Abstract

We consider the propagation of arbitrary electromagnetic pulses in anomalously dispersive dielectrics characterized by M relaxation processes. A partial differential equation for the electric field in the dielectric is derived and analyzed. This single equation describes a hierarchy of $M + 1$ wave types, each type characterized by an attenuation coefficient and a wave speed. Our analysis identifies a "skin-depth" where the pulse response is described by a telegrapher's equation with smoothing terms, travels with the wavefront speed, and decays exponentially. Past this shallow depth we show that the pulse response is described by a weakly dispersive advection-diffusion equation, travels with the sub-characteristic advection speed equal to the zero-frequency phase velocity in the dielectric, and decays algebraically. The analysis is verified with a numerical simulation. The relevance of our results to the development of numerical methods for such problems is discussed.

1. Introduction

The application of ultra-short pulsed fields in the areas of radar, hyperthermia, and biological/environmental imaging is imminent. For that reason there is a need for a thorough understanding of the short-pulse response of media, such as biological tissues, soils, humid atmospheres, and radar absorbing materials, whose dielectric properties are described by frequency-dependent permittivity models fitted to experimental data. In addition, a future extension of the IEEE C95.1-1991 RF exposure standard to regulate pulsed fields will also require qualitative and quantitative understanding of this sort to be developed. Since the alternative to actual measurement of the response is numerical simulation we are also interested in obtaining analytical results to guide the development of robust numerical techniques for such applications (see Section 6).

In this paper we consider time-domain electromagnetic pulse propagation in general relaxing dielectrics, a problem relevant to studies of electromagnetic interactions in homogeneous anomalously dispersive media. We will be concerned primarily with biological media but our results can be used directly to understand pulse propagation in other dielectrics provided their permittivity is represented by relaxation models. The Debye model [1] (orientational relaxation mechanism) has been found to accurately represent the experimentally obtained frequency-dependent permittivity of biological media [2]-[3], of homogeneous dispersive rock [4]-[5], and of homogeneous sea ice [6]. All these media generally exhibit several relaxation mechanisms. Accordingly, experimentally obtained dielectric data is fitted to the complex relative permittivity function

$$\epsilon(\omega) = \epsilon_{\infty} + \sum_{n=1}^M \frac{\epsilon_n^0 - \epsilon_{\infty}}{1 - i\omega\tau^n}, \quad (1)$$

for the relevant range of frequencies ω in order to study wave propagation in a given material. In (1) ϵ_{∞} is the infinite-frequency relative permittivity, ϵ_n^0 the zero-frequency relative permittivity of the n -th relaxation mechanism, and τ^n the n -th relaxation time constant. The phase velocity of harmonic waves in the dielectric is $v^{phase}(\omega) = c/\text{Re}\sqrt{\epsilon(\omega)}$, with c being the speed of light in vacuum. Typical parameters for which (1) fits water data in the microwave frequency range are $M = 1$, $\epsilon_s = 80.35$, $\epsilon_{\infty} = 1.0$, $\tau = 8.13$ picoseconds [2]. Water is considered here since it is a major constituent of human tissue. We will use the inverse Fourier transform with (1) in the electromagnetic frequency-domain constitutive relation, $\vec{D} = \epsilon_o\epsilon(\omega)\vec{E} = \epsilon_o(\epsilon_{\infty}\vec{E} + \sum_{n=1}^M \vec{P}^n)$, to close the system of Maxwell's equations in

the time-domain with M ordinary differential equations, one for each relaxation \tilde{P}^n forced by the electric field. The reformulation in Section 3 of the resulting problem (Equation (3), Section 2) as a signaling problem involving a single partial differential equation (p.d.e.) for the electric field E ,

$$\sum_{n=0}^M \beta_n \partial_t^{M-n} (\partial_{tt} - c_n^2 \partial_{zz}) E = 0, \quad (2)$$

facilitates further analysis. The coefficients β_n characterize dissipative effects associated with the n -th wave type, and c_n is the corresponding wave speed. Both constants are related to the parameters selected, so that (1) fits the experimental data for a given medium. All the sub-characteristics of (2) with speeds c_n ($n = 1, \dots, M$) lie between the characteristic with speed c_0 , and the zero speed characteristic of multiplicity M . Therefore, the relative permittivity (1) is causal and its real and imaginary parts are related through the Kramers-Kronig relations [7].

Equation (2) belongs to a class of p.d.e. which describe coexisting waves of different types [8], e.g., non-dispersive, dispersive, diffusive. In Section 4 we show that the high-order term, $n = 0$, mainly describes the propagation of the penetrating pulse in a thin layer near the air/dielectric interface. In this layer the lower order terms contribute exponential decay and smoothing of the pulse envelope. We name this short depth the "skin-depth" for pulses. The pulse propagates there with speed $c_0 = v^{phase}(\omega = \infty)$. The layer's width is determined by the time constant of the fastest relaxation since it will be the first one to equilibrate, i.e., $z_{skin} \sim O(c_0 \tau^{min})$ meters. Each lower order term, $1 < n < M - 1$, becomes sequentially important as the pulse propagates deeper in the medium while the remaining orders introduce smoothing, dispersion, and diffusion. Since the available experimental data shows that $\beta_M \gg 1$ typically, the low-order term, $n = M$, will describe the main response which will travel with speed $c_M = v^{phase}(\omega = 0)$ in the bulk of the medium while the higher order terms will introduce high-order dispersion and diffusion. Thus, the response inside the dielectric will be decaying as $z^{-\alpha}$, $\alpha \geq 1/2$. The achieved value of α depends on the pulse frequency content, the pulse shape, and on M . Explicit solutions will be given for $M = 1$ whence the short- and long-time response respectively satisfy a telegraphers equation and an advection-diffusion equation. For this case we will deduce the $O(c_0 \tau)$ size of the "skin-depth" for pulses, and the asymptotic decay rate $z^{-1/2}$ with depth of the peak electric field, or $t^{-1/2}$ with time. These results are verified with a numerical simulation in Section 5. The rate of decay determined herein for pulsed electric fields may be of interest to

workers in the fields of hyperthermia or ground penetrating radar. The signals used in these technological areas are continuous waves and as a result the electric field in the dielectric (tissue or ground) decays exponentially with depth [7] due to the imaginary part of the frequency-dependent permittivity. Our work suggests using pulsed electromagnetic waves to circumvent shortcomings associated with use of continuous waves in such applications.

2. Formulation

A Transverse Magnetic pulse is obliquely incident on a homogeneous dispersive half-space from the air side ($z < 0$) at an angle ϕ_{inc} with the normal to the air/dielectric interface. The dielectric occupies the half-space $z \geq 0$. The equations governing the scattering and propagation of the incident pulse are the time-domain Maxwell's equations coupled, thru the electric field, to M ordinary differential equations that describe the evolution of M orientational polarization mechanisms (P_y^n ; $n = 1, \dots, M$, see (1)) of Debye type. They are:

$$\begin{aligned}\mu_o \frac{\partial H_x}{\partial t} &= \frac{\partial E_y}{\partial z} \\ \mu_o \frac{\partial H_z}{\partial t} &= -\frac{\partial E_y}{\partial x} \\ \epsilon_o \epsilon_\infty \frac{\partial E_y}{\partial t} &= \frac{\partial H_x}{\partial z} - \frac{\partial H_z}{\partial x} - \epsilon_o \sum_{n=1}^M \frac{\partial P_y^n}{\partial t} \\ \frac{\partial P_y^n}{\partial t} &= \frac{1}{\tau^n} (\epsilon_o \Delta \epsilon^n E_y - P_y^n); \quad n = 1, \dots, M,\end{aligned}\tag{3}$$

where ϵ_o and μ_o are respectively the permittivity and permeability of the vacuum, and $\Delta \epsilon^n = \epsilon^n - \epsilon_\infty$. Apart from ϵ_o and μ_o all other parameters in (3) are obtained by fitting (1) to experimental data for the tissue types of interest. The incident electric field is an arbitrary plane pulse $E_y^{inc}(x, z, t) = f(t - x \sin \phi_{inc}/c - z \cos \phi_{inc}/c)$ of duration T_p , and we assume it has been in contact with the interface since $t = -\infty$. Operational considerations fix the incident pulse shape f , and T_p . On the interface, $z = 0$, the total electric field is given by $E_y(x, 0, t) = f(t - x/v) + E^{scat}(x, 0, t) = g(t - x/v)$, where $v = c/\sin \phi_{inc}$, and E^{scat} is the scattered field. Thus g is known, either by direct measurement of E_y on the interface, or by measurement of E^{scat} in the air region $z < 0$. In Section 3 we will show that (3) is a strictly hyperbolic system of p.d.e.

The incident pulse description along with the electromagnetic boundary conditions on the dielectric interface at $z = 0$ impose symmetry on all the fields and a change of dependent variables (indicated by the arrow) is possible: $E_y(x, z, t) \rightarrow \tilde{E}_y(z, t - x/v)$, and $H_{x,z}(x, z, t) \rightarrow \tilde{H}_{x,z}(z, t - x/v)$. A one-dimensional system for the tilded fields can be obtained by defining the time-like variable $\xi = t - x/v$, and changing coordinates $(x, z, t) \rightarrow (z, \xi)$ in (3). Omitting details, we find that $\tilde{H}_x(z, \xi) = \frac{1}{v\mu_0} \tilde{E}_y(z, \xi)$. Through differentiation with respect to ξ and z we can further eliminate \tilde{H}_x to obtain the following one-dimensional system of equations,

$$\begin{aligned} \frac{\partial^2 \tilde{E}_y}{\partial \xi^2} - c_\infty^2 \frac{\partial^2 \tilde{E}_y}{\partial z^2} &= \frac{-1}{\epsilon_\infty \cos^2 \phi_{inc}} \sum_{n=1}^M \frac{\partial^2 \tilde{P}_y^n}{\partial \xi^2} \\ \frac{\partial \tilde{P}_y^n}{\partial \xi} + \frac{1}{\tau^n} \tilde{P}_y^n &= \frac{\Delta \epsilon^n}{\tau^n} \tilde{E}_y; \quad n = 1, \dots, M, \end{aligned} \quad (4)$$

where $c_\infty = c/\sqrt{\epsilon_\infty} \cos \phi_{inc}$ is the wavefront speed in the dielectric, and $c = 1/\sqrt{\epsilon_0 \mu_0}$. In the next section we derive from (4) a single equation for the electric field in the dispersive medium by eliminating all the \tilde{P}_y^n . Once \tilde{E}_y is determined the remaining magnetic field is $\tilde{H}_x = \frac{1}{\mu_0} \int_0^\xi \frac{\partial \tilde{E}_y(z, \xi')}{\partial z} d\xi'$.

It is instructive to consider here various limiting values of the τ^n by appealing to the solution of the second equation in (4), i.e.,

$$\tilde{P}_y^n(\xi) = \Delta \epsilon^n \int_0^\xi \frac{e^{-\frac{\xi-\xi'}{\tau^n}}}{\tau^n} \tilde{E}_y(\xi') d\xi'; \quad n = 1, \dots, M. \quad (5)$$

Letting some, or all, of the τ^n be large corresponds to making the approximation $e^{-\frac{\xi-\xi'}{\tau^n}}/\tau^n \sim (1 - O(\frac{\xi-\xi'}{\tau^n}))/\tau^n$ in (5). By letting one of the relaxation times be large, e.g., take $\tau^1 \gg \tau^n$, $n = 2, \dots, M$, so that (5) becomes $\tilde{P}_y^1 \sim \frac{\Delta \epsilon^1}{\tau^1} \int_0^\xi \tilde{E}_y(\xi') dt'$, one can model the presence of a zero-frequency conductivity in the medium with value $\sigma = \frac{\Delta \epsilon^1}{\tau^1 \epsilon_\infty \cos^2 \phi_{inc}}$. The right hand side of (4) will have the term $-\sigma \frac{\partial \tilde{E}_y}{\partial \xi}$ and it will now be coupled to $M - 1$ ordinary differential equations for the remaining relaxations. In the "infinite"-relaxation limit ($\tau^n \gg 1$; $n = 1, \dots, M$ so that $\tilde{P}_y^n \sim \frac{\Delta \epsilon^n}{\tau^n} \int_0^\xi \tilde{E}_y(\xi') d\xi'$) (4) becomes a telegraphers equation for propagation in a medium of constant conductivity,

$$\frac{\partial^2 \tilde{E}_y}{\partial \xi^2} - c_\infty^2 \frac{\partial^2 \tilde{E}_y}{\partial z^2} + \sigma_\infty \frac{\partial \tilde{E}_y}{\partial \xi} = 0, \quad (6)$$

where $\sigma_\infty = \frac{1}{\epsilon_\infty \cos^2 \phi_{inc}} (\sum_{n=1}^M \frac{\Delta \epsilon^n}{\tau^n})$. In this case the "skin-depth" extends to infinity. Alternatively, one can derive the zero-relaxation limit by integrating (5) by parts and exploiting

the fact that $1/\tau^n \rightarrow \infty; n = 1, \dots, M$, to evaluate the Laplace integral $\int_0^\xi e^{\xi'/\tau^n} \frac{\partial \bar{E}_y(\xi')}{\partial \xi'} d\xi'$ which arises. Then, all mechanisms appear in equilibrium, i.e., $\bar{P}_y^n \sim \Delta\epsilon^n \bar{E}_y$, and (4) becomes a lossless wave equation describing propagation in a medium of nondispersive relative permittivity $\epsilon^0 = \epsilon_\infty \cos^2 \phi_{inc} + \sum_{n=1}^M \Delta\epsilon^n$,

$$\frac{\partial^2 \bar{E}_y}{\partial \xi^2} - \frac{c_\infty^2}{1 + \frac{\sum_{n=1}^M \Delta\epsilon^n}{\epsilon_\infty \cos^2 \phi_{inc}}} \frac{\partial^2 \bar{E}_y}{\partial z^2} = 0. \quad (7)$$

Note that now the "skin-depth" collapses to zero.

Equations (6) and (7) respectively set the lower- and upper-bound of the peak electric field inside the medium. With increasing z , \bar{E}_y becomes smoother since $\frac{\partial^2 \bar{E}_y}{\partial \xi^2} \ll \frac{\partial \bar{E}_y}{\partial \xi}$, and (6) becomes the diffusion equation (no propagation). The field will be zero past some small depth. This will be the lower bound of the peak response in the original medium. On the other hand, (7) describes the upper bound of the response in the equilibrated medium. This bound is the zero frequency transmission coefficient for the interface, $T(\omega = 0) = 2/(1 + \sqrt{\epsilon^0})$. We have just shown that $0 < |\bar{E}_y^{peak}| \leq T(\omega = 0)$, i.e., that the maximum response in the dispersive medium is bounded above and below by the large-depth response in media corresponding respectively to the "infinite"- and zero-relaxation limits of the original medium.

3. The Wave Hierarchy

In this Section we set $E = \bar{E}_y$ and $P^n = \bar{P}_y^n$ for simplicity. We define the following operators:

$$\begin{aligned} D^n &= \partial_\xi + \frac{1}{\tau^n} \\ D_n &= \prod_{\substack{m=1 \\ m \neq n}}^M D^m \\ D &= \prod_{m=1}^M D^m. \end{aligned} \quad (8)$$

To begin the derivation of (2) apply the operator D to both sides of the first equation in (4) and the operator D_n to the second equation there twice differentiated with ξ . Our working system now is

$$D\left(\frac{\partial^2 E}{\partial \xi^2} - c_\infty^2 \frac{\partial^2 E}{\partial z^2}\right) = \frac{-1}{\epsilon_\infty \cos^2 \phi_{inc}} \sum_{n=1}^M D \frac{\partial^2 P^n}{\partial \xi^2}$$

(9)

$$D_n D^n P_{\xi\xi}^n = \frac{\Delta \epsilon^n}{\tau^n} D_n E_{\xi\xi}; \quad n = 1, \dots, M.$$

Noting from (8) that $D = D_n D^n$ we sum the second equation in (9) over n thus obtaining an expression for the right-hand side of the first equation there in terms of the electric field, i.e.,

$$\sum_{n=1}^M D \frac{\partial^2 P^n}{\partial \xi^2} = \sum_{n=1}^M \Delta \epsilon^n \frac{1}{\tau^n} D_n E_{\xi\xi}. \quad (10)$$

Equation (9) now becomes

$$D \left(\frac{\partial^2 E}{\partial \xi^2} - c_\infty^2 \frac{\partial^2 E}{\partial z^2} \right) + \frac{1}{\epsilon_\infty \cos^2 \phi_{inc}} \sum_{n=1}^M \Delta \epsilon^n \frac{1}{\tau^n} D_n E_{\xi\xi} = 0. \quad (11)$$

Using in (11) the identity $\frac{1}{\tau^n} D_n = (D^n - \partial_\xi) D_n = D - \lim_{\tau \rightarrow \infty} \{D^n\} D_n$ and the expansion

$$D = \sum_{n=0}^M \alpha_n \partial_\xi^{M-n} \quad (12)$$

$$\alpha_0 = 1$$

$$\alpha_n = \frac{1}{n!} \sum_{\substack{i_n=1 \\ i_n \neq i_{n-1}, \dots, i_1}}^M \frac{1}{\tau^{i_n}} \sum_{\substack{i_{n-1}=1 \\ i_{n-1} \neq i_{n-2}, \dots, i_1}}^M \frac{1}{\tau^{i_{n-1}}} \dots \sum_{\substack{i_2=1 \\ i_2 \neq i_1}}^M \frac{1}{\tau^{i_2}} \sum_{i_1=1}^M \frac{1}{\tau^{i_1}}; \quad n = 1, \dots, M-1$$

$$\alpha_M = \prod_{i=1}^M \frac{1}{\tau^i},$$

we obtain, after rearranging the various terms, the sought after single p.d.e. for E in the quarter-plane:

$$\sum_{n=0}^M \beta_n \partial_\xi^{M-n} (\partial_{\xi\xi} - c_n^2 \partial_{zz}) E = 0; \quad z > 0, \xi > 0$$

$$\beta_0 = 1, \quad c_0 = c_\infty$$

$$\beta_n = \alpha_n + \frac{1}{\epsilon_\infty \cos^2 \phi_{inc}} \sum_{i=1}^M \Delta \epsilon^i (\alpha_n - \lim_{\tau \rightarrow \infty} \{\alpha_n\}); \quad n = 1, \dots, M-1 \quad (13)$$

$$c_n = \frac{c_0}{\sqrt{\beta_n}}; \quad n = 1, \dots, M-1$$

$$\beta_M = \alpha_M \left(1 + \frac{\sum_{i=1}^M \Delta \epsilon^i}{\epsilon_\infty \cos^2 \phi_{inc}} \right), \quad c_M = c_0 \sqrt{\frac{\alpha_M}{\beta_M}}.$$

The signaling problem is complete once we specify the initial and boundary conditions $E(z, 0) = \partial_\xi E(z, 0) = \dots = \partial_\xi^{M+1} E(z, 0) = 0$ and $E(0, \xi) = g(\xi)$ respectively, and the radiation condition $E(z \rightarrow \infty, \xi) \rightarrow 0$. Equation (13) is a strictly hyperbolic p.d.e. since the $n = 0$ term, which is the principal part of the operator acting on E , has a complete set of $M + 2$ distinct eigenvectors, one for each of the two distinct eigenvalues $\pm c_0$, and M eigenvectors for the zero eigenvalue of multiplicity M due to the ∂_ξ^M operating on the $n = 0$ term. Note that (13) also holds in two- and three-dimensions for every component of the electric field if ∂_{zz} is replaced by ∇^2 , the appropriate higher dimensional Laplacian. This is because the incident electric field induces the polarization so that $\vec{\nabla} \cdot \vec{P} = 0$ everywhere inside the medium. Equation (13) is valid for material parameters that are continuously or discretely layered in the z -direction (depth). The β_n and c_n form the ordered sequences

$$\beta_0 = 1 < \beta_1 < \dots < \beta_n < \dots < \beta_{M-1} < \beta_M \quad . \quad (14)$$

$$c_0 = v^{phase}(\omega = \infty) > c_1 > \dots > c_n > \dots > c_{M-1} > c_M = v^{phase}(\omega = 0)$$

so each wave type is a member of a wave hierarchy.

4. Analysis of the Hierarchy

To introduce the incident pulse duration in our analysis we scale the independent variables, $\xi' = \frac{\xi}{T_p}$ and $z' = \frac{z}{c_0 T_p}$, change to the new variables, and then drop the primes for convenience. Our working equation, factored to exhibit left- and right-going waves, then becomes

$$\sum_{n=0}^M \beta_n T_p^n \partial_\xi^{M-n} (\partial_\xi - \bar{c}_n \partial_z) (\partial_\xi + \bar{c}_n \partial_z) E = 0, \quad (15)$$

where $\bar{c}_0 = 1$ and $\bar{c}_n = c_n/c_0$. The "infinite"-relaxation limit (Equation (6)) is equivalent to $T_p \ll \tau^{minimum}$ whence $\beta_M T_p^M \ll 1$, while the zero-relaxation limit (Equation (7)) is equivalent to $T_p \gg \tau^{maximum}$ ($\beta_M T_p^M \gg 1$). The peak response will be bounded as described in Section 2 for any pulse duration and the response in the medium will depend on the frequency content of the boundary function $g(\xi)$. The highest frequencies constitute the high-order waves described mainly by $n = 0$ term in (15) and will propagate with the wavefront speed $\bar{c}_0 (= 1)$ which is the highest speed. In the "skin-depth" the high-order waves approximately satisfy $\partial_\xi E \sim -\bar{c}_0 \partial_z E$ since the relaxations have not had time yet

to respond to the incoming wave. Using this in each term in (15) except in $\partial_\xi + \bar{c}_0 \partial_z$ we determine the p.d.e. that governs this order's propagation, i.e.,

$$(\partial_\xi + \bar{c}_0 \partial_z)E + \frac{1}{2\beta_0} \sum_{n=1}^M (-1)^{n+1} \beta_n T_p^n \frac{\bar{c}_0^2 - \bar{c}_n^2}{\bar{c}_0^{n+1}} \partial_z^{-n+1} E = 0, \quad (16)$$

where the operator ∂_z^{-n+1} is interpreted formally as $n-1$ integrations of E with respect to z . The second term in (16) is a smoothing operator with the $n=1$ term producing exponential decay of E with depth. Discontinuities of $g(\xi)$ will be important only near the interface across the characteristic ray $z - \bar{c}_0 \xi = 0$ and will be exponentially attenuated for models with $M=1$. Models fitted to data with $M > 1$ will smooth any discontinuity in the incident pulse.

Bands of lower frequencies around the relaxation frequencies are each governed by the intermediate terms $1 \leq n \leq M-1$ in (15). Because experimental data indicates that $\beta_M \gg 1$ ($\beta_M \sim O(10^{13})$ for an $M=1$ model of water) these intermediate orders are unimportant in comparison to the low-order waves described by the $n=M$ term. From the dependence of β_M on the angle of incidence we also deduce that the amplitude of the low-order waves (and hence of the main response) will be maximal for pulses that are normally incident. Due to the largeness of β_M the low-order waves approximately satisfy $\partial_\xi E \sim -\bar{c}_M \partial_z E$ and using this in (15), except in the term $\partial_\xi + \bar{c}_M \partial_z$, the p.d.e. governing the propagation of this wave order is

$$(\partial_\xi + \bar{c}_M \partial_z)E + \frac{(\bar{c}_M)^{M-1}}{2\beta_M T_p^M} \sum_{n=0}^{M-1} (-1)^{M-n} \beta_n T_p^n \frac{\bar{c}_n^2 - \bar{c}_M^2}{(\bar{c}_M)^n} \partial_z^{M-n+1} E = 0. \quad (17)$$

Equation (17) describes diffusive-dispersive propagation with speed \bar{c}_M ($\sim 1/9$ for the $M=1$ water model). Dispersion comes from those terms of the second part of (17) which contain odd number of derivatives of E with respect to z , while diffusion comes from terms with even number of z -derivatives of E . The response is smooth across the sub-characteristic rays $z - \bar{c}_n \xi = \text{constant}$; $n=1, \dots, M$. The largeness of β_M indicates that low frequencies are important in such problems. These frequencies need not be present in the problem through a zero-frequency component in the incident pulse, rather they appear through the spectrum of the envelope of incident pulses which always contains low frequencies. One could have derived (17) by using the slow variables $z' = \epsilon^\gamma(z - \bar{c}_M t)$ and $t' = \epsilon^{2\gamma} t$ ($0 < \epsilon \ll 1$) in the same way long-wave approximations are derived. In such a derivation the particular value of γ will depend on whether $M+2$ is even or odd.

In this paragraph we consider (16) and (17) for $M=1$ (our water model). For this

medium we obtain explicit solutions describing the behavior of the response and we are interested in deducing qualitative results from them. These results will be validated with a numerical simulation in the next section for $\phi_{inc} = 0$ ($\xi = t$). The equation for the small-depth response is

$$(\partial_\xi + \partial_z)E + \frac{1}{2}\beta_1 T_p(1 - \bar{c}_1^2)E = 0, \quad (18)$$

while for large-depth it is

$$(\partial_\xi + \bar{c}_1 \partial_z)E - \frac{1 - \bar{c}_1^2}{2\beta_1 T_p} \partial_z^2 E = 0. \quad (19)$$

The constants are $\bar{c}_1 = \frac{1}{\sqrt{\tau\beta_1}}$, $\beta_1 = \frac{1}{\tau}(1 + \frac{\Delta\epsilon^1}{\epsilon_\infty \cos^2 \phi_{inc}})$, and $\Delta\epsilon^1 = \epsilon_s - \epsilon_\infty$. Values for ϵ_s , ϵ_∞ , and τ for water are given in the introduction. Note that (19) is parabolic while the (18) and the full problem are hyperbolic. The solution of (18), subject to the boundary condition $E(0, \xi) = g(\xi)$, is

$$E(z, \xi) = g(\xi - z)e^{-\frac{1}{2}\beta_1 T_p(1 - \bar{c}_1^2)z}, \quad (20)$$

It shows that the contribution of the exponentially decaying part of the response will be negligible after a depth $O(c_0\tau)$ m (in dimensional variables) which we name the "skin-depth."

The solution of (19) is

$$E(z, \xi') = \sqrt{\frac{\beta_1 T_p}{2\pi(1 - \bar{c}_1^2)}} z \int_0^{\xi'} d\kappa \frac{h(\kappa)}{(\xi' - \kappa)^{\frac{3}{2}}} e^{-\frac{\beta_1 T_p}{2(1 - \bar{c}_1^2)} \frac{(z - \bar{c}_1(\xi' - \kappa))^2}{\xi' - \kappa}}, \quad (21)$$

where $h(\xi')$ is related to the inverse Fourier transform of the spectrum of $g(\xi)$ after the highest frequencies have decayed in the "skin-depth." The origin of ξ' is the first time after which the response evolves according to (21) and is approximately $O(\tau)$ sec. The response is diffusing around the sub-characteristic $z = \bar{c}_1 \xi'$, and its peak will be on that ray. Thus the frequency content of the response is constricted through diffusion. The kernel in (21) acts like a delta-function because $\beta_1 \gg 1$. This leads to the prediction that on the sub-characteristic ray the peak response for an arbitrary incident pulse will be decaying as $z^{-\alpha}$, $\alpha \geq 1/2$, or as $\xi'^{-\alpha}$ (this can be obtained by remembering that also $\xi' = z/\bar{c}_1$ on the sub-characteristic ray), i.e.,

$$E(z, \xi') \sim \sqrt{\frac{\beta_1 T_p}{2\pi(1 - \bar{c}_1^2)}} z \frac{h(0)}{\xi'^{\frac{3}{2}}}; \quad z = \bar{c}_1 \xi'. \quad (22)$$

For pulses with $h(0) = 0$ (21) is evaluated after $h(\kappa)$ is expanded in a Taylor series around zero.

5. Numerical Experiments

Now we validate the results of the previous section for the $M = 1$ Debye model of water, namely the predictions that the response is exponentially decaying in a thin layer (the "skin-depth") where it travels with the infinite-frequency phase velocity $c_0 = c$, and that past this layer it travels with the zero-frequency phase velocity and is a diffusion wave whose peak decays algebraically. The propagation of a normally incident ($\phi_{inc} = 0^\circ$) square pulse of $T_p = 50$ psec is simulated by solving the system (3) with $M = 1$. The discretization parameters are chosen with the aid of our previous work [9] and the results shown contain no numerical artifacts. The numerical source is in free-space, 5 cells in front of the interface, and there are 10 cells between the left-hand side radiation condition (which is in free-space) and the dielectric. We record time-traces of the response every ten spatial cells starting at a depth of 10 cells in the medium, and subsequently search in the data for the peak response which we save along with the location (t^{peak}, z^{peak}) of its occurrence. The computational domain is taken to be large so that artificial reflections from the right-hand end of the grid do not reach the recording locations in the time window of interest.

Fig. 1 shows the (t, z) location of the peak of the response in the half space for the first 80 psec of evolution. The z -axis offset at $t = 0$ corresponds to twenty cells (left-hand radiation condition to first recording depth). We see that the peak response indeed travels with the free-space speed of light as predicted. The prediction is graphed as a dotted line. The gap in the curve (between the parallel lines) is due to the movement of the peak from the leading edge of the pulse to the trailing edge. The data in that interval was deleted since the apparent slow-down is not relevant to the speed of propagation of the peak. Past 50 psec the pulse peak starts slowing down. This happens up to about 75 psec whence the speed of the peak has achieved the zero-frequency phase velocity. This is shown clearly in Fig. 2 where the evolution of the peak's location past 80 psec is shown. The slope of the straight line is $c/\sqrt{80.35}$ and this is very close to the observed slope. It takes a "skin-depth" of $O(\epsilon\tau)$ m (~ 2.4 mm) to achieve this slow speed.

Fig. 3 shows the decay of the peak of the response for $0.05 < z < 0.25$ mm during the early evolution. The Figure shows that the predicted exponential decay, i.e., the dotted line drawn according to (20), is observed in the simulation results (circles). Finally, Fig. 4 depicts the decay of the pulse peak for $z > O(\epsilon\tau)$ m, i.e., past the "skin-depth". On the graph we indicate with a dashed line the algebraic decay $z^{-\frac{1}{2}}$ predicted by (22) with $z = c_1 t$.

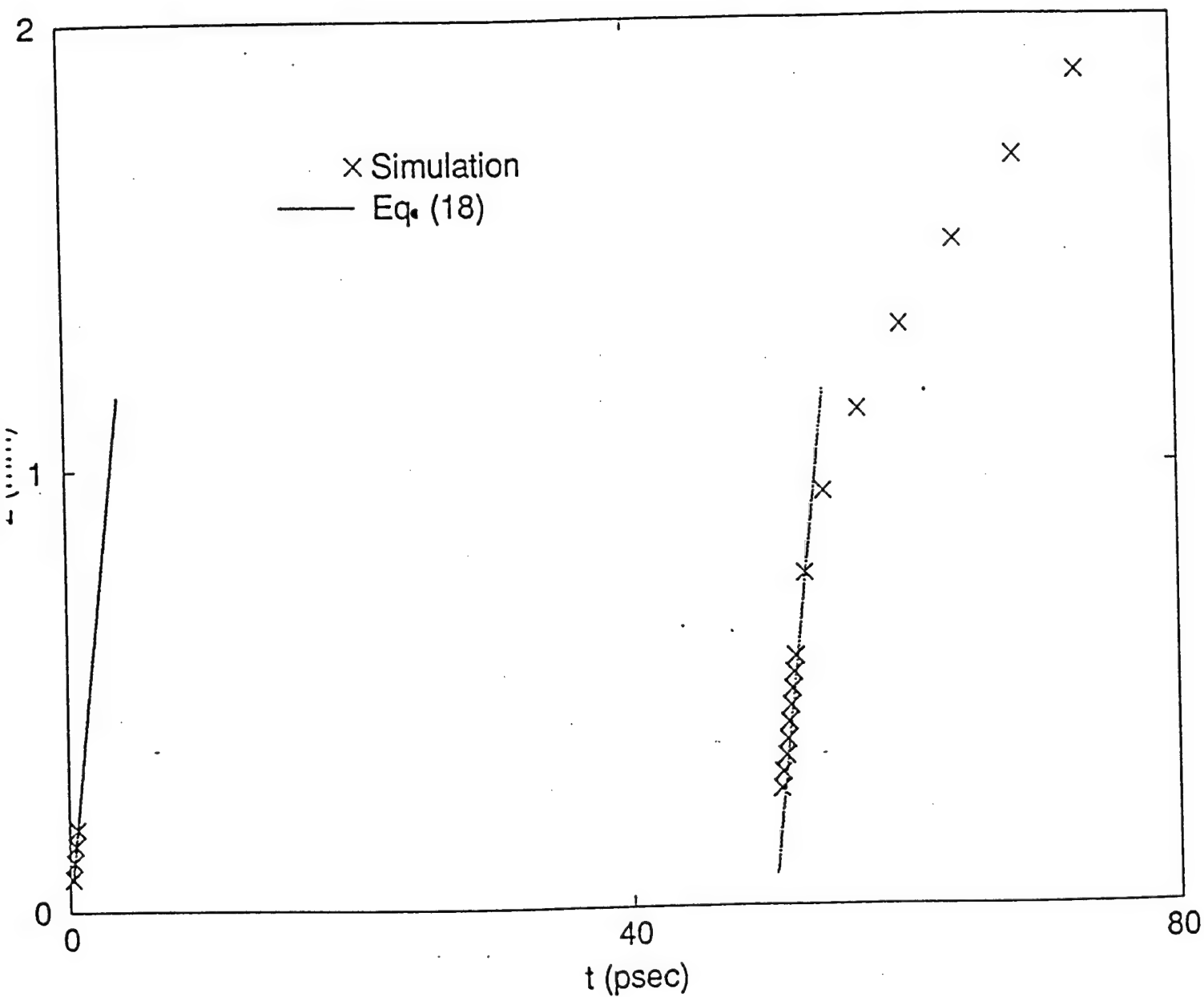


Figure 1 The (t, z) location of the peak of the response during the first 80 psec of evolution. The slope of the dotted lines is exactly c as predicted by Eq. (18). The separation of the two parallel lines is exactly the pulse duration.

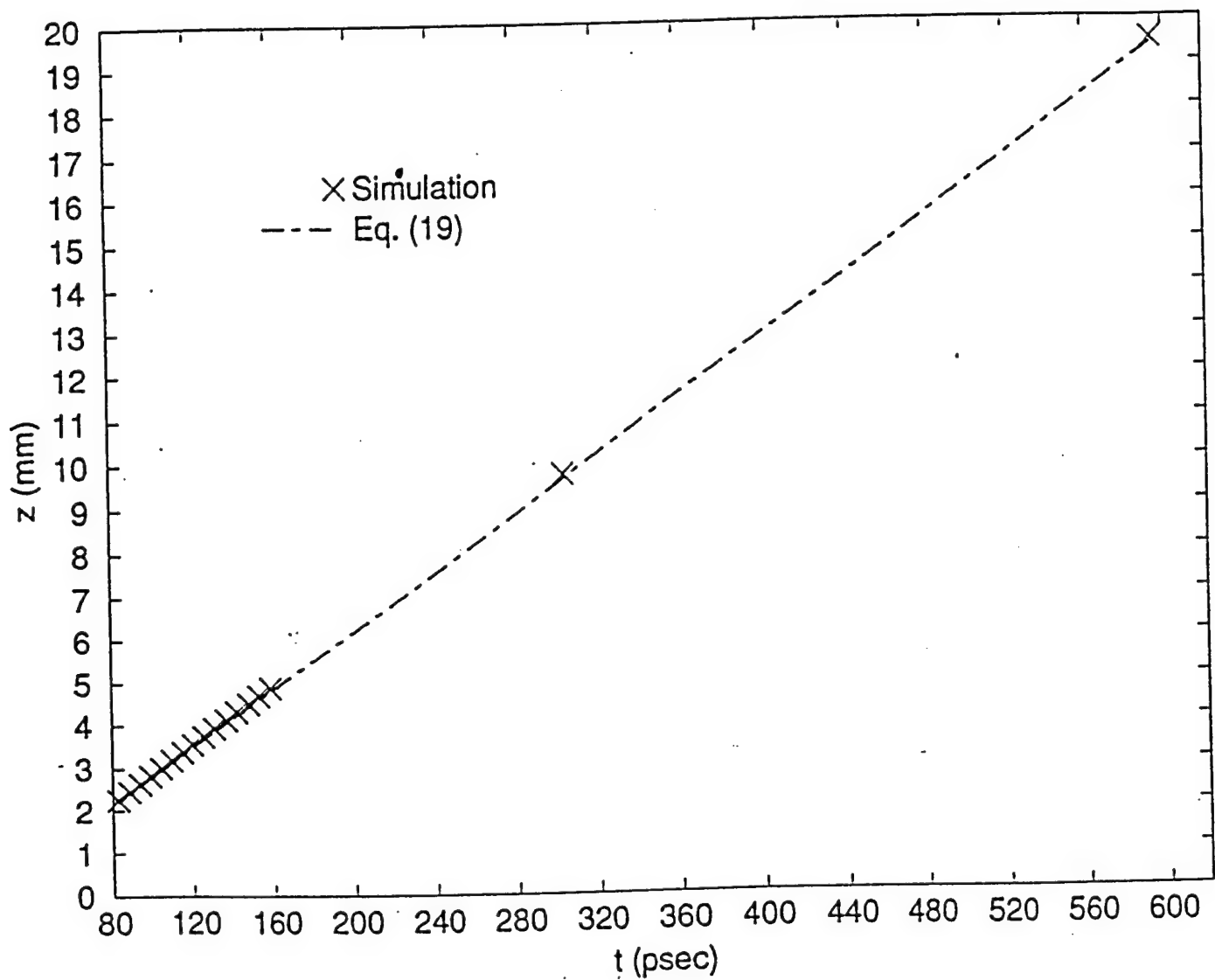


Figure 2 The (t, z) location of the peak of the response for $t > 80$ psec. The slope of the dashed line is the prediction $c_1 = c/\sqrt{80.35}$.

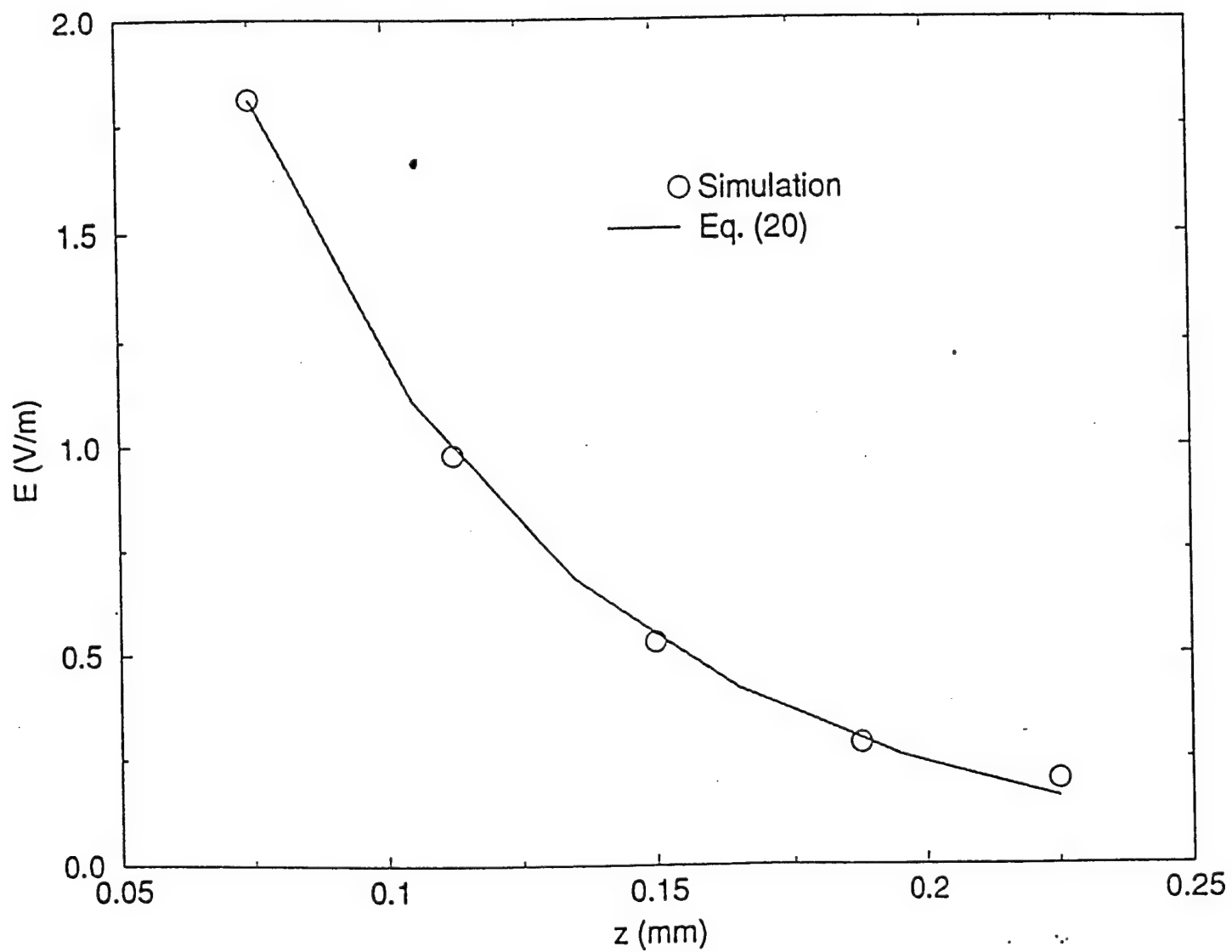


Figure 3 The small-depth decay of the peak of the response as a function of z . The dotted line indicates the predicted exponential decay and the circles indicate the observed decay.

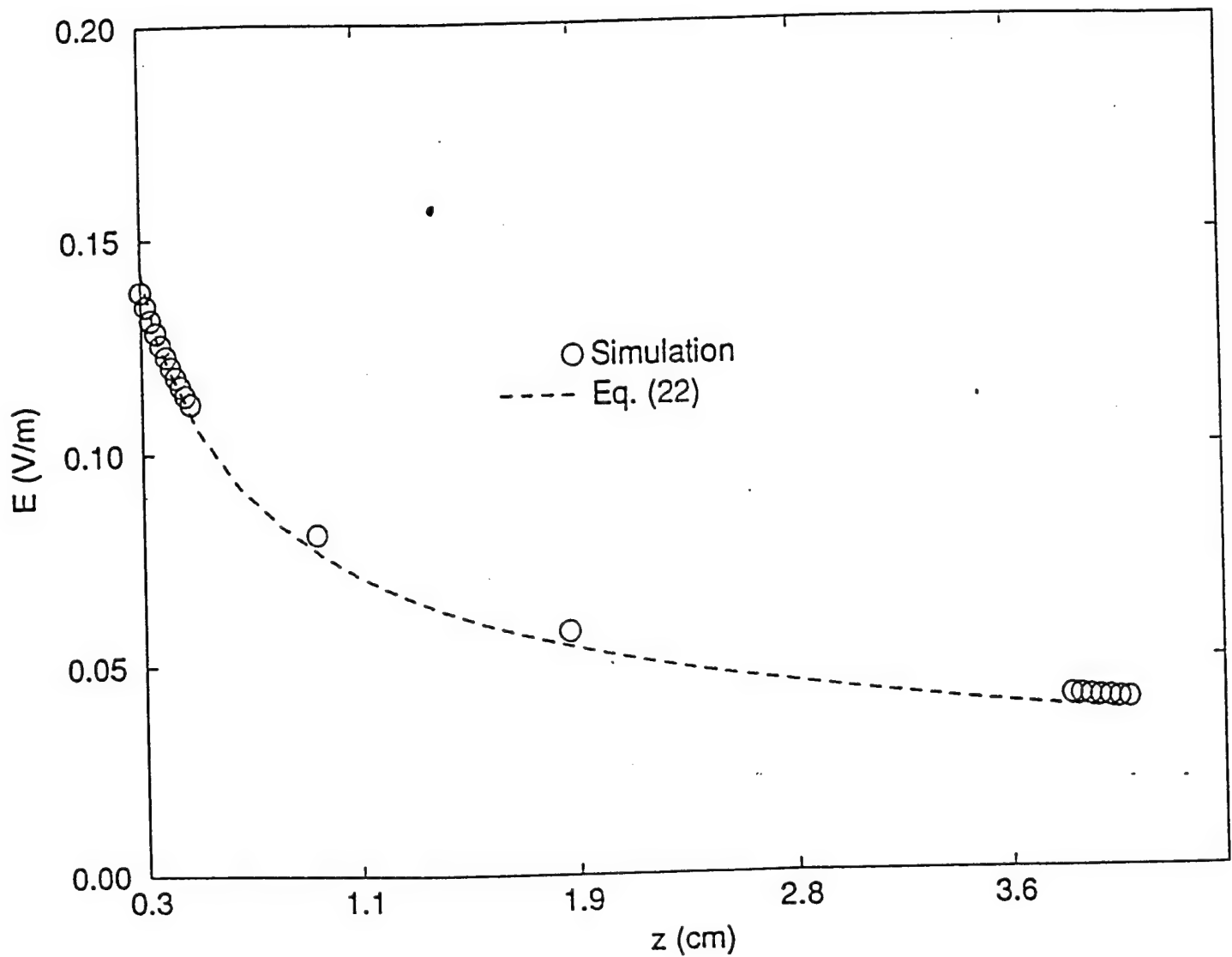


Figure 4 The large-depth decay of the peak of the response as a function of z . The dashed line indicates the predicted algebraic decay and the circles indicate the observed decay.

The observed decay is plotted with open circles.

6. Ramifications for Numerical Schemes

In summary, we have found that the pulse response in a relaxing dielectric is mainly a diffusion wave traveling with the zero-frequency phase velocity, c_M , of harmonic waves, and that the fastest speed c_0 , i.e., the infinite-frequency phase velocity, is important only in a thin layer near the air/dielectric interface in which the response is hyperbolic and decays exponentially. As an example, for the $M = 1$ model of water permittivity this thin layer is $O(10^{-3})$ m, and $c_1 \sim c_0/9$. Thus, one is faced with a stiff problem in the time direction due to the exponential decay in the "skin-depth," and with the existence of disparate wave speeds in well defined spatio-temporal regions. In addition, the problem is asymptotically singularly perturbed since for large z and t it changes type from hyperbolic (18) to parabolic (19). In this section we indicate how these findings can be used to correctly set the discretization in existing numerical methods for pulse propagation in relaxing media. Also, we present an argument in favor of using high-order finite difference schemes which are second-order accurate in time and fourth-order accurate in space.

We have shown in [9] that the timestep, Δt , for Leapfrog based Debye schemes is required to resolve the shortest relaxation timescale τ^{\min} for reasonable accuracy over long-time simulations. This is due to the time stiffness in the problem for realistic media and to the fact that simple A-stable approaches (the trapezoidal method) were used in those methods to discretize the ordinary differential equations for the polarization.

Next we show how to choose the spatial resolution in light of the existence of multiple speeds in the dielectric. In explicit finite difference schemes for equations with multiple wave speeds the stability requirement is based on the highest speed in the problem, c_0 , while the spatial resolution is based on the slow speed, c_M . Due to the large magnitude of β_M the slow speed will be dominant in realistic models of materials. In the system (3) the other speeds c_n , $1 \leq n \leq M$, are not evident. It must be noted here that the slow speed is not characteristic and that it develops during the evolution. This is contrary to what happens in elastic wave propagation where the two speeds (compressional and shear) are characteristic speeds. If one considers a fixed frequency f then we see that the wavelength associated with the slow speed is smaller than that associated with the fast speed, thus, a small length scale develops in time. If we assume that the $M+1$ wave types are decoupled then the timestep for

each type is determined by $\Delta t/\Delta z_n = \nu/c_n$, $n = 0, \dots, M$, where ν is the Courant number. Thus, for a fixed timestep and Courant number, the spatial steps for the most important waves in the problem are related as

$$\Delta z_M = \frac{c_M}{c_0} \Delta z_0. \quad (23)$$

We deduce that the disparate speeds require a reduction of the Courant number since one would have to use Δz_M from (23) in the stability restriction $c_0 \Delta t/\Delta z_M = \nu$ to obtain the timestep, i.e., $c_0 \Delta t/\Delta z_0 = \nu c_M/c_0 < \nu$, where ν is the value we would have used if we only knew of the characteristic speed. Typically, $0.1 < c_M/c_0 < 0.5$.

Finite difference schemes which are second-order accurate in both time and space, the so called (2 - 2) schemes, require that the Courant number used be the maximum allowed for stability ($\nu = 1$ in one dimension) in order for them to introduce the least phase error. Here we have shown that once the spatial resolution is set according to the slow speed one cannot get away from having to reduce the Courant number. However, (2 - 4) schemes that are second-order accurate in time and fourth-order accurate in space are stable for $\nu \leq 6/7$, operate well for $0.1 < \nu < 0.5$, and they are overall fourth-order accurate for $\Delta t \sim O(1)\Delta z^2$. This last relationship between the time and the spatial steps in the high-order scheme is like the diffusion scaling $t \sim O(1)z^2$ which appears in our problem asymptotically. In any case, due to the time stiffness one desires to use a small time step by reducing the Courant number or by increasing the spatial cell size and this can be done with (2 - 4) schemes. If (2 - 2) schemes are used the time stiffness will also affect the Δz by forcing it to be extremely small.

References

- [1] P. Debye, *Polar Molecules*, New York: Dover (1929).
- [2] C. J. F. Bottcher and P. Bordewijk, "Theory of Electric Polarization Vol. II," New York: Elsevier (1978).
- [3] W. D. Hurt, "Multiterm Debye Dispersion Relations for Permittivity of Muscle," *IEEE Trans. Biomedical Engineering*, vol. 32, pp. 60-64, 1985.
- [4] J. A. Fuller and J. R. Wait, "Electromagnetic Pulse Transmission in Homogeneous Dispersive Rock," *IEEE Trans. Antennas Propagat.*, vol. 20, pp. 530-533, 1972.

- [5] T. M. Papazoglou, "Transmission of a Transient Electromagnetic Plane Wave Into a Lossy Half-Space," *J. Applied Physics*, vol. 46, pp. 3333-3341, 1975.
- [6] A. Von Hippel, *Dielectric Materials and Applications*, New York: Wiley (1954).
- [7] J. D. Jackson, *Classical Electrodynamics*, 2nd ed. New York: Wiley (1975).
- [8] G. B. Whitham, *Linear and Nonlinear Waves*, New York: Wiley (1974).
- [9] P. G. Petropoulos, "Stability and Phase Error Analysis of FD-TD in Dispersive Dielectrics," *IEEE Trans. Antennas Propagat.*, vol. 42, pp. 62-69, 1994.

PHASE ERROR CONTROL FOR FD-TD METHODS OF SECOND AND FOURTH ORDER ACCURACY

Abstract

For FD-TD methods we determine the spatial resolution of the discretized domain in terms of the total computation time and the desired phase error. It is shown that the spatial step should vary as $\Delta x \sim g \left[\frac{e_\phi}{t_c} \right]^{1/s}$ in order to maintain a prescribed phase error level e_ϕ throughout the computation time t_c , where s ($=2$ or 4) is the spatial order of accuracy of the scheme and g is a geometric factor. Significantly, we show that the thumb rule of using 10-20 points per wavelength to determine the spatial cell size for the standard scheme is not optimal. Our results are verified by numerical simulations in two dimensions with the Yee scheme and a new 4th-order accurate FD-TD scheme.

1. Introduction

In finite element methods for the frequency-domain Maxwell's equations the electrical size of the computational domain is related to the quantity $k\Delta = 2\pi/N_{ppw}$, where k is the wavenumber, Δ is a typical spatial cell size, and N_{ppw} is the points per wavelength. In these methods, in order to maintain a constant error level, N_{ppw} should increase as the domain's electrical size increases [1]-[3], thus higher order elements should be used on electrically large problems since they require a smaller N_{ppw} for the same error in comparison to the standard elements. Herein, we consider time-domain FD-TD methods and derive the N_{ppw} required so that only a prescribed amount of phase error accumulates in a given computation time interval. We will consider the standard Yee scheme [4], hereafter referred to as the (2,2) scheme, and a 4th-order accurate in space FD-TD type scheme [8], hereafter named the (2,4) scheme since it is 2nd-order accurate in time.

We will derive and numerically validate the estimate

$$N_{ppw} \sim \alpha(s, \theta) \left[\frac{P}{e_\phi} \right]^{\frac{1}{s}} \quad (1.1)$$

for determining the spatial discretization in two dimensional FD-TD schemes of spatial order of accuracy s ($=2$ or 4 here). In (1.1) θ is the angle of propagation with respect to a grid axis, P is the number of periods in time for which the computation will proceed, and e_ϕ is the maximum phase error in radians that will be allowed to accumulate over the computation duration for the highest frequency in the problem. From t_c , the actual computation time, and ω_* , the highest frequency that is expected to be present in the calculation it is $P = t_c \omega_*/2\pi$. An estimate for ω_* can be obtained by considering the initial pulse frequency content, while e_ϕ and t_c are defined *a priori*. Our derivation will start from the semi-discrete Maxwell's equations thus our estimate will be formally valid in the case $\nu \ll 1/\sqrt{2}$, where $\nu = c\Delta t/\Delta$ is the Courant number of the fully discrete scheme. However, we will show in Section 2 that the dependence of the phase error on P and N_{ppw} as shown in (1.1) also holds for fully discrete schemes. The implication of (1.1) is that methods of higher order of accuracy in space can achieve the same error over a fixed computation time interval as the Yee scheme but with a larger spatial step (less memory) and less amount of timesteps. (1.1) will be verified by numerical simulations of mode propagation in a metallic waveguide (a truly two dimensional test case) with the (2,2) and (2,4) FD-TD schemes.

The first (2,4) and (4,4) schemes on two and three dimensional staggered meshes appeared in [5] for subsets of Maxwell's equations in the time-domain. Reference [6] presented a

method for achieving 4th-order time accuracy without requiring the introduction of extra time levels of storage. In [7] a two dimensional (2,4) FD-TD type scheme was presented for the elastic velocity-stress vector wave equations. References [8] and [9] also present 4th-order schemes for Maxwell's equations.

2. Dispersion Analysis

Our working equations are the two dimensional Maxwell's equations for Transverse Magnetic (TM) polarization in an unbounded domain,

$$\begin{aligned}\frac{\partial H_y}{\partial t} &= \frac{\partial E_z}{\partial x} \\ \frac{\partial H_x}{\partial t} &= -\frac{\partial E_z}{\partial y} \\ \frac{\partial E_z}{\partial t} &= \left(\frac{\partial H_y}{\partial x} - \frac{\partial H_x}{\partial y} \right),\end{aligned}\tag{2.1}$$

but our analysis can be applied to Transverse electric (TE) polarization, and to the general three dimensional equations. (2.1) results from the dimensional Maxwell's equations by scaling the electric and magnetic fields respectively on $\sqrt{\epsilon_0}$ and $\sqrt{\mu_0}$, and subsequently scaling space and time respectively on the speed of light c and its inverse c^{-1} so that $|k|$, the magnitude of the wavevector \vec{k} , and ω are synonymous quantities. An exact solution of (2.1) corresponding to a spatial Fourier component is the vector $\vec{M} = (H_y(x, y, t), H_x(x, y, t), E_z(x, y, t))^T = (h_y(t), h_x(t), e_z(t))^T e^{i(k_x x + k_y y)}$, where the superscript T denotes transpose, and $\vec{k} = \hat{i}k_x + \hat{j}k_y$ is the wavevector. We determine the $h_y(t), h_x(t), e_z(t)$ by substituting in (2.1) and solving the resultant Ordinary Differential Equations (ODE) for the time dependence with initial conditions given by the constant vector $\vec{M}(x, y, 0)$. The resulting plane wave solution is given by

$$\vec{M} = \begin{Bmatrix} h_y(0) \\ h_x(0) \\ e_z(0) \end{Bmatrix} e^{i|k|(x \sin \theta + y \cos \theta - t)}.\tag{2.2}$$

In (2.2) we have used $k_x = |k| \sin \theta$, $k_y = |k| \cos \theta$, with θ being the angle of propagation with respect to the vertical y -axis of the grid. The analysis now proceeds by considering 2nd- and 4th-order accurate finite difference approximations for $\partial/\partial x$ and $\partial/\partial y$ in (2.1).

Representing the spatial derivatives by half-cell centered 2nd-order accurate finite differences (FD-TD), denoting the resulting approximate solution by \vec{M}^{app} , and substituting it in

(2.1) we obtain the ODE system

$$\begin{aligned}
\frac{dh_y^{app}(t)}{dt} e^{i\frac{k_x \Delta}{2}} &= \frac{1}{\Delta} (e^{ik_x \Delta} - 1) e_z^{app}(t) \\
\frac{dh_x^{app}(t)}{dt} e^{i\frac{k_y \Delta}{2}} &= -\frac{1}{\Delta} (e^{ik_y \Delta} - 1) e_z^{app}(t) \\
\frac{de_z^{app}(t)}{dt} &= \frac{1}{\Delta} (e^{i\frac{k_x \Delta}{2}} - e^{-i\frac{k_x \Delta}{2}}) h_y^{app}(t) - \frac{1}{\Delta} (e^{i\frac{k_y \Delta}{2}} - e^{-i\frac{k_y \Delta}{2}}) h_x^{app}(t)
\end{aligned} \tag{2.3}$$

with Δ being the cell width (taken to be the same in the x and y directions), where space is discretized as $(x, y) = (m\Delta, n\Delta)$ with integer (m, n) . Upon elimination of the magnetic components from (2.3) we get a second-order ODE for the time evolution of the electric field. Solving this ODE we find that (using $\Delta = \frac{2\pi}{|k|N_{ppw}}$)

$$E_z^{app}(x, y, t) = e_z(0) e^{i[k_x x + k_y y - t \frac{|k|N_{ppw}}{\pi} \sqrt{\sin^2(\frac{\pi}{N_{ppw}} \sin \theta) + \sin^2(\frac{\pi}{N_{ppw}} \cos \theta)}]} \tag{2.4}$$

The phase error is defined as the ordered difference between the exact and numerical phase, $e_\phi = \Phi_{exact} - \Phi_{numerical}$. Subtracting the phase of (2.4) from that of the electric field component in (2.2) we find the phase error produced by the spatial finite differencing to be

$$\begin{aligned}
e_\phi &= -|k|t \left[1 - \frac{N_{ppw}}{\pi} \sqrt{p_x^2 + p_y^2} \right] \\
p_x &= \sin\left(\frac{\pi \sin \theta}{N_{ppw}}\right) \\
p_y &= \sin\left(\frac{\pi \cos \theta}{N_{ppw}}\right).
\end{aligned} \tag{2.5}$$

Thus, e_ϕ grows linearly with time, t , for a given discretization that is fixed at the beginning of the simulation. For an actual computation one would set $|k|$ to be the highest wavenumber, $|k_*|$, in the problem for which we want a preset accuracy to be maintained up to the end of the time stepping. From (2.5), using $t = t_c$ and the Taylor series of the \sin function for π/N_{ppw} small, and keeping only the first term in the series for which e_ϕ in (2.5) is non-vanishing we obtain the approximate dependence of N_{ppw} on the allowed phase error, the total computation time, and the angle of propagation, as follows (using $|k_*|t_c = 2\pi P$)

$$N_{ppw} \sim \left(\frac{1}{3}\right)^{\frac{1}{2}} \pi^{\frac{3}{2}} (\sin^4 \theta + \cos^4 \theta)^{\frac{1}{2}} \left(\frac{P}{e_\phi}\right)^{\frac{1}{2}}. \tag{2.6}$$

The phase error of the fully discrete scheme can be found using the methods in [12]. In the notation used here it is given by

$$e_\phi = -2\pi P \left[1 - \frac{N_{ppw}}{\nu\pi} \sin^{-1}(\nu\sqrt{p_x^2 + p_y^2}) \right] \quad (2.7)$$

where ν is the Courant number, and p_x, p_y are as in (2.5). It is immediately obvious that (2.7) reduces to (2.5) for small ν regardless of the size of π/N_{ppw} . (2.6) is subsequently recovered for π/N_{ppw} small. Additionally, for π/N_{ppw} small and ν arbitrary it is easy to show that

$$\frac{N_{ppw}}{\nu\pi} \sin^{-1}(\nu\sqrt{p_x^2 + p_y^2}) \sim 1 - \frac{1}{6} \left(\frac{\pi}{N_{ppw}} \right)^2 (\sin^4\theta + \cos^4\theta) + \frac{1}{72} \left(\frac{\pi}{N_{ppw}} \right)^4 (\sin^6\theta + \cos^6\theta) - \dots, \quad (2.8)$$

so, by neglecting 4th order and higher terms, (2.8) reduces (2.7) to (2.6) regardless of the Courant number ν . Thus, (2.6) also holds for the fully discrete scheme with arbitrary ν as long as π/N_{ppw} is small.

The $O(\Delta^4)$ accurate half-cell centered discretization for the spatial derivatives in (2.1) is given by

$$\frac{\partial f}{\partial \xi} \Big|_{\xi=(m+\frac{1}{2})\Delta} = \frac{1}{\Delta} \left[\frac{9}{8} (f_{m+1} - f_m) - \frac{1}{24} (f_{m+2} - f_{m-1}) \right] \quad (2.9)$$

where $\xi = x$ or y , and for electric variables m is an integer while for magnetic variables $m = m' - \frac{1}{2}$ with m' an integer. When discretized in time (2.1) will result in the (2.4) scheme given by the difference equations [2] below:

$$\begin{aligned} H_y^{n+\frac{1}{2}}(i + \frac{1}{2}, j) &= H_y^{n-\frac{1}{2}}(i + \frac{1}{2}, j) + \gamma [\zeta(E_x^n(i+1, j) - E_x^n(i, j)) - \\ &\quad \eta(E_x^n(i+2, j) - E_x^n(i-1, j))] \\ H_x^{n+\frac{1}{2}}(i, j + \frac{1}{2}) &= H_x^{n-\frac{1}{2}}(i, j + \frac{1}{2}) - \gamma [\zeta(E_z^n(i, j+1) - E_z^n(i, j)) - \\ &\quad \eta(E_z^n(i, j+2) - E_z^n(i, j-1))] \\ E_x^{n+1}(i, j) &= E_x^n(i, j) + \gamma [\zeta(H_y^{n+\frac{1}{2}}(i + \frac{1}{2}, j) - H_y^{n+\frac{1}{2}}(i - \frac{1}{2}, j)) - \\ &\quad \eta(H_y^{n+\frac{1}{2}}(i + \frac{3}{2}, j) - H_y^{n+\frac{1}{2}}(i - \frac{3}{2}, j)) - \\ &\quad \zeta(H_x^{n+\frac{1}{2}}(i, j + \frac{1}{2}) - H_x^{n+\frac{1}{2}}(i, j - \frac{1}{2})) + \end{aligned} \quad (2.10)$$

$$\eta(H_x^{n+\frac{1}{2}}(i, j + \frac{3}{2}) - H_x^{n+\frac{1}{2}}(i, j - \frac{3}{2})),$$

where $\gamma = \Delta t/\Delta$, $\zeta = 9/8$, and $\eta = 1/24$. Altering η, ζ one obtains the (4,4) FD-TD scheme [8] which can be analyzed with the methods herein. The semi-discrete case is recovered by letting $\Delta t \rightarrow 0$ in (2.10). Proceeding as for the (2,2) scheme, we obtain the phase error for the (2,4) scheme

$$\begin{aligned} e_\phi &= -|k|t[1 - \frac{N_{ppw}}{\pi}\sqrt{p_x^2 + p_y^2}] \\ p_x &= \frac{9}{8}\sin(\frac{\pi \sin \theta}{N_{ppw}}) - \frac{1}{24}\sin(\frac{3\pi \sin \theta}{N_{ppw}}) \\ p_y &= \frac{9}{8}\sin(\frac{\pi \cos \theta}{N_{ppw}}) - \frac{1}{24}\sin(\frac{3\pi \cos \theta}{N_{ppw}}), \end{aligned} \quad (2.11)$$

where $|k| = |k_*|$ (the magnitude of the maximum wavenumber in the problem). Setting $|k_*|t_c = 2\pi P$, and expanding the \sin functions for small values of π/N_{ppw} (2.11) becomes

$$N_{ppw} \sim (\frac{3}{20})^{\frac{1}{4}} \pi^{\frac{5}{4}} (\sin^6 \theta + \cos^6 \theta)^{\frac{1}{4}} (\frac{P}{e_\phi})^{\frac{1}{4}}. \quad (2.12)$$

The phase error of the fully discrete scheme (2.10) can also be found. In the notation used here that phase error is again (2.7) but with p_x and p_y now given by those in (2.11). Arguments similar to those after (2.7) apply here too for the relation of the exact error to (2.12).

Relations (2.6) and (2.12) are the main result of this paper since they give an estimate for N_{ppw} based on a priori selected computation parameters. Figure 1 shows the N_{ppw} required to maintain a phase error of 0.1 radians ($\sim 5.73^\circ$) over P time periods of computation for a harmonic wave propagating along the grid axis ($\theta = 0^\circ$) and along the grid diagonal ($\theta = 45^\circ$). The benefit of a high order spatial differencing scheme is apparent from this Figure particularly for long time computations (P large) with such a severe phase error restriction. Significantly, Figure 1 indicates that for the standard Yee scheme the thumb rule of $N_{ppw} = 10 - 20$ will be good for computations up to only $P = 3$ for a phase error of 5.73° . Figure 1 also applies to the fully discrete schemes used with any ν whenever π/N_{ppw} is small. Since in our analysis ν is the same (~ 0) for both the (2,2) and (2,4) methods another deduction from the Figure is that the higher order methods will allow a larger time step.

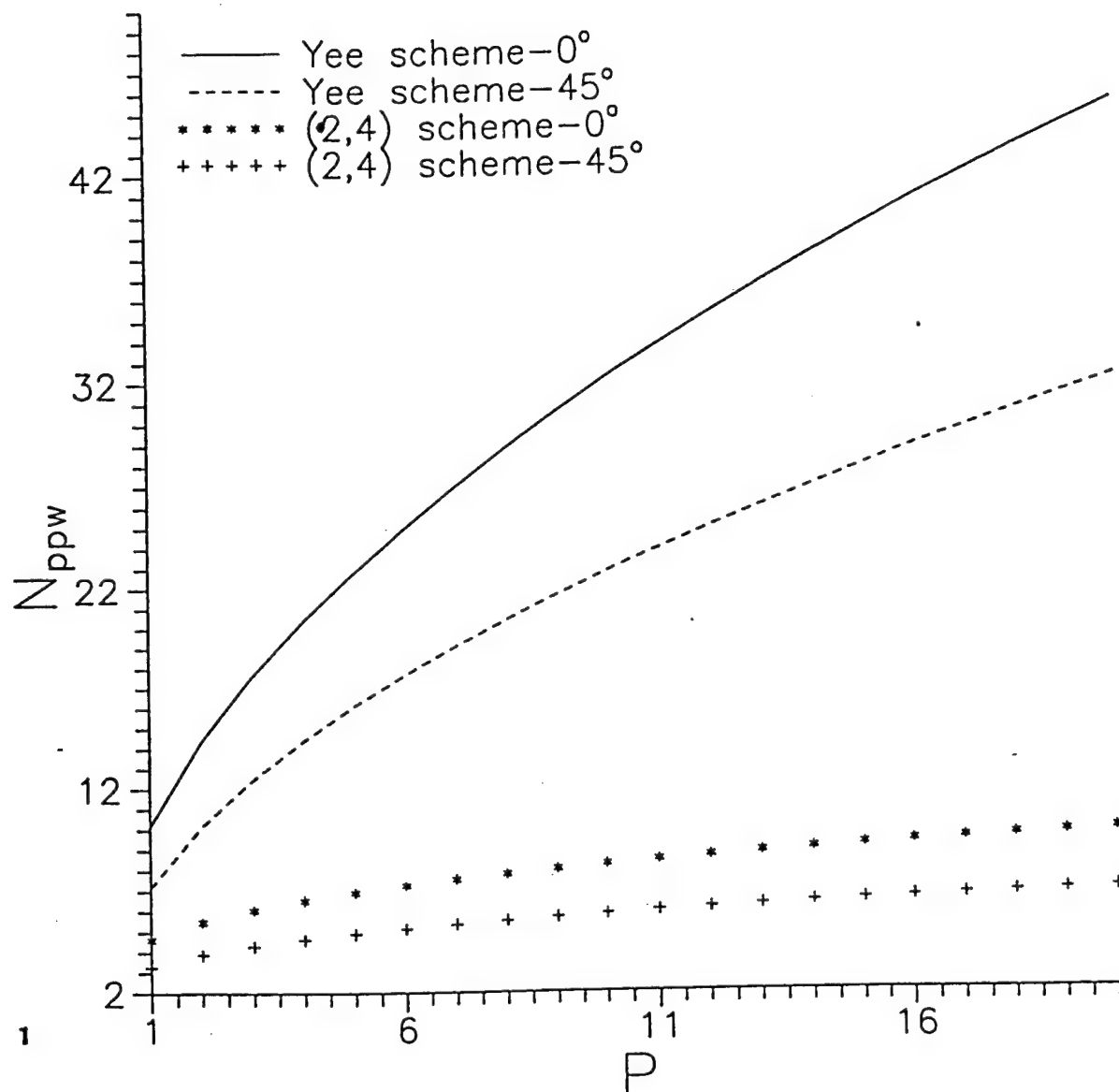


FIGURE 1

Figure 1 The dependence of N_{ppw} on P for an allowed phase error $e_\phi = 0.1$ radians ($\sim 5.73^\circ$) and two angles of propagation with respect to the grid axis.

3. Numerical Validation

We consider a mode propagating in a metallic air-filled waveguide. The system (2.1) is solved numerically on the domain $0 \leq x \leq 1$, $0 \leq y \leq 1$, $0 \leq t \leq t_c$, together with Dirichlet boundary conditions on the waveguide walls $E_x(x, y = 0, t) = E_x(x, y = 1, t) = 0$, $H_y(x, y = 0, t) = H_y(x, y = 1, t) = 0$ for $0 \leq x \leq 1$, and periodic boundary conditions along the direction of propagation $E_z(x = 0, y, t) = E_z(x = 1, y, t)$, $H_y(x = 0, y, t) = H_y(x = 1, y, t)$ for $0 \leq y \leq 1$. An exact solution representing the ℓ -th mode is easy to find with standard methods [11]. In the following, $k\xi = \sqrt{k^2 - (\ell\pi)^2}$ is the longitudinal wavenumber, and $\ell = 1, 2, \dots$ is the waveguide mode index. This model problem provides a truly two dimensional test of our analysis. In a well resolved computation the truncation error is negligible, the only error source being phase misrepresentation due to the differencing. Figure 2 shows for the Yee scheme the effect of phase error (only 5.12°) on the relative error for a computation in the waveguide designed with the analysis herein. Although visually (Figure 2a) the phase error seems to be responsible for just a small shift in the computed field we note (Figure 2b) its large effect on the relative error. The reliability of interior field calculations depends on the relative error they contain. The main problem here is that the zeros of the field are not computed correctly due to the (small) phase error although the absolute field values are very accurate.

The Dirichlet conditions for the standard FD-TD posed no problem since it is enough to apply the boundary condition $E_x = 0$ on the waveguide walls by prescribing the E_x nodes at $y = 0, 1$ and $0 \leq x < 1$, for the boundary condition to be automatically satisfied to 2nd-order accuracy by the differencing strategy. However, the implementation of boundary conditions for the (2,4) scheme is not so straightforward. The spatial stencil of the 4th-order method is twice as long as that of the standard FD-TD, thus special treatment is required for electric and magnetic nodes adjacent to the metallic waveguide walls. After alot of experimentation we used the symmetry properties of the electric and magnetic fields with respect to the waveguide walls (the electric field is an odd function of y , while the magnetic field is an even function of y with respect to the walls) to implement the Dirichlet condition for the (2,4) method with 4th-order accuracy. Matching the Yee scheme 2nd-order differencing to the (2,4) interior stencil in order to compute the nodes adjacent to the computational boundary proved to be unstable.

The model problem is discretized with the (2,2) and (2,4) schemes in order to obtain the

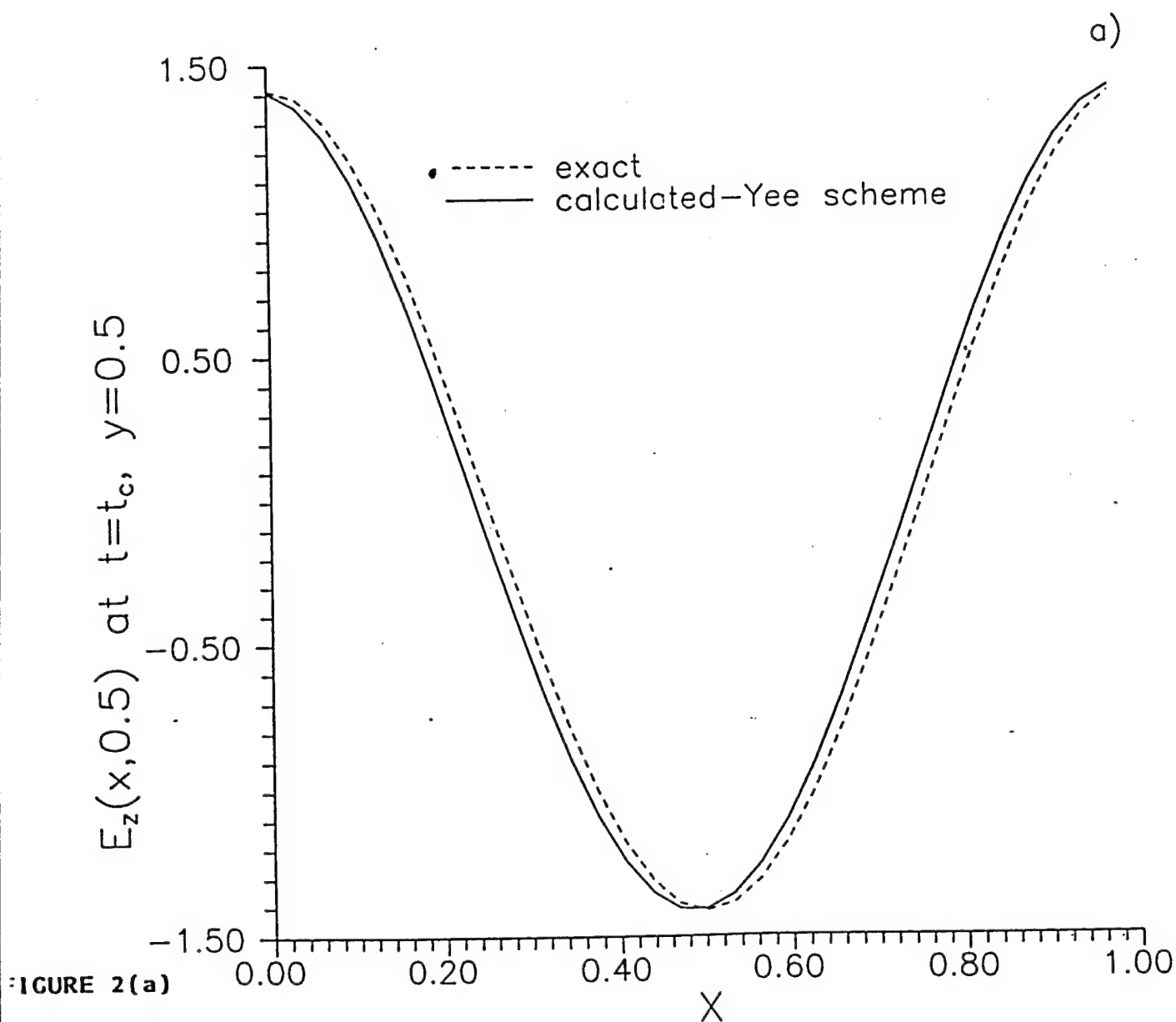


Figure 2 a) Electric field along the waveguide at $P = 10$, $y = 0.5$, computed by the standard Yee scheme with 5.12° phase error (solid line). b) Error relative to the exact solution solely due to the "small" phase error allowed.

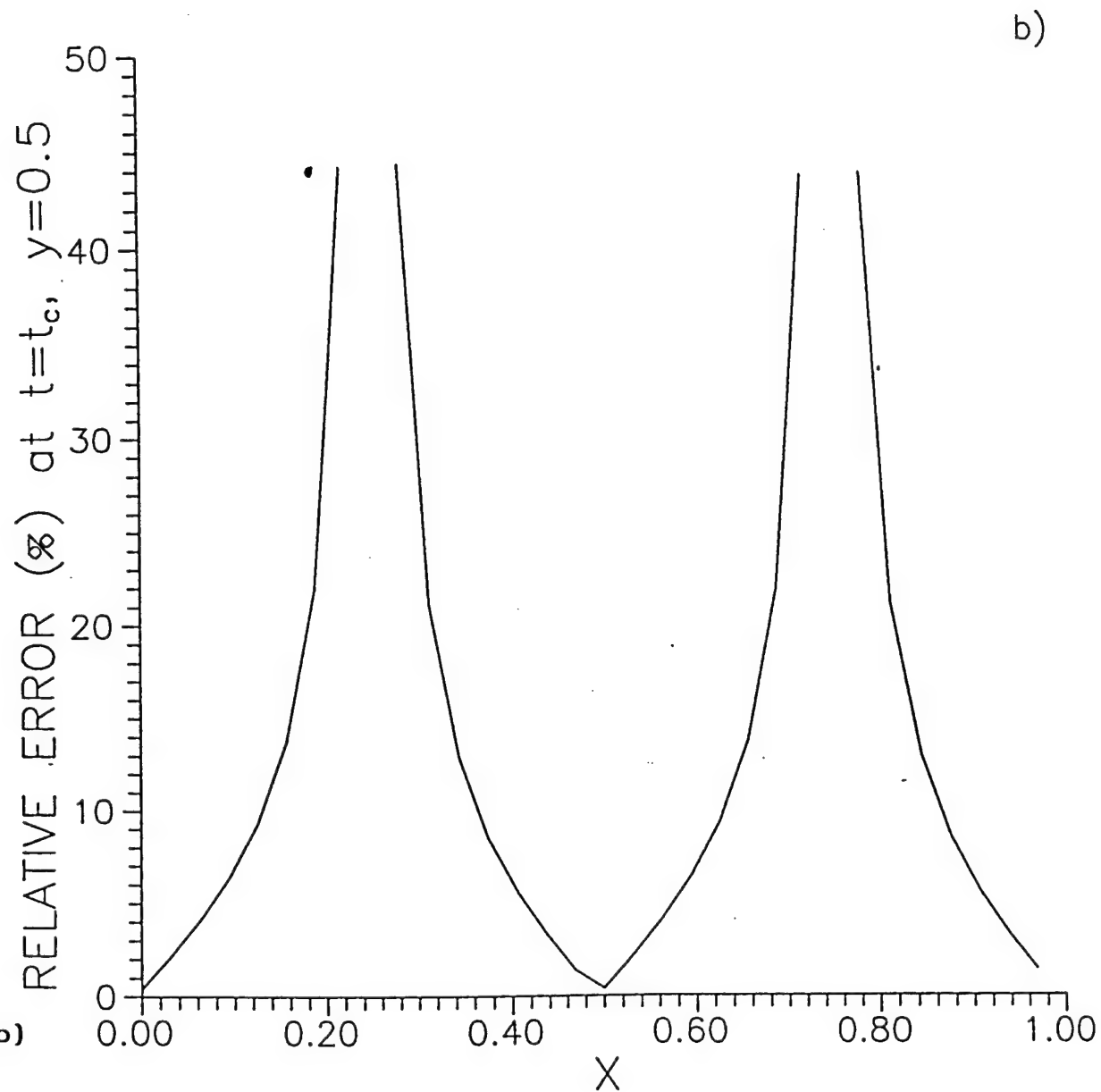


FIGURE 2(b)

Figure 2 a) Electric field along the waveguide at $P = 10$, $y = 0.5$, computed by the standard Yee scheme with 5.12° phase error (solid line). b) Error relative to the exact solution solely due to the "small" phase error allowed.

fields at the final timestep corresponding to time $t_c = P * \xi$, where P is the number of domain traversals (periods) of the mode whose phase speed is ξ^{-1} . The total number of timesteps is $NMAX = t_c / \Delta t = P * N_{ppw} * \xi / \nu$. We set $k = \sqrt{5}\pi$. Both the standard FD-TD and the (2,4) schemes are initialized by prescribing $E_z^{\ell=1}(x, y, t = 0)$ and $H_{x,y}^{\ell=1}(x, y, t = -\Delta t/2)$ from the exact solution thus obtaining the first waveguide mode traveling to the right along the x-axis. The numerically computed fields should exactly reproduce the initial conditions after the completion of $NMAX$ timesteps if there is no phase error. However, phase error accumulates during the actual computation, and we measure it by assigning $360/N_{ppw}$ degrees in each spatial cell and using linear interpolation to find the field node at time $t = t_c$ which now has shifted due to the phase error. For both schemes $\nu = 0.01$ ($\ll 1/\sqrt{2}$). The cell size is determined from the $\theta = 0^\circ$ curve in Figure 1 for $P = 10$ and $e_\phi = 5.73^\circ$ ($= 0.1$ radians), and corresponds to $N_{ppw} = 32$ for the (2,2) scheme and $N_{ppw} = 8$ for the (2,4) scheme. Since $\Delta t = \nu\Delta$ the 4th-order scheme required one fourth the amount of timesteps required by the standard scheme per computational period (715.5 timesteps for the (2,4) scheme hence we will measure e_ϕ at even multiples of the period).

Figure 3 shows for the Yee scheme the predicted (dashed line), obtained from (2.6) with $\theta = 0^\circ$, against the calculated (plus) phase errors as functions of computation time measured in integer multiples of the period corresponding to the $\ell = 1$ mode. We see the predicted error was slightly larger than the one encountered in the computation. This can be explained by considering that the particular waveguide mode can be thought to be composed of two plane waves traveling to the right at an angle $\theta_{\ell=1} = 90^\circ - \tan^{-1}(1/2)$ with the y-axis. Therefore the N_{ppw} used in this experiment was generous. The measured phase error for the 4th-order scheme (stars) can also be seen to follow the predicted phase error (solid line) obtained from (2.12) with $\theta = 0^\circ$. Again, the measured error was slightly less than the prediction for the same reason as for the Yee scheme.

4. Summary

In this paper we considered the phase error due to the spatial discretization in the two dimensional FD-TD method for Maxwell's equations. We derived how the cell size should be chosen so that only a preset phase error accumulates during a given amount of computation time. Truly two dimensional numerical simulations validated the analytical results. Although the derivation is formally valid for cases where the numerical computations are performed

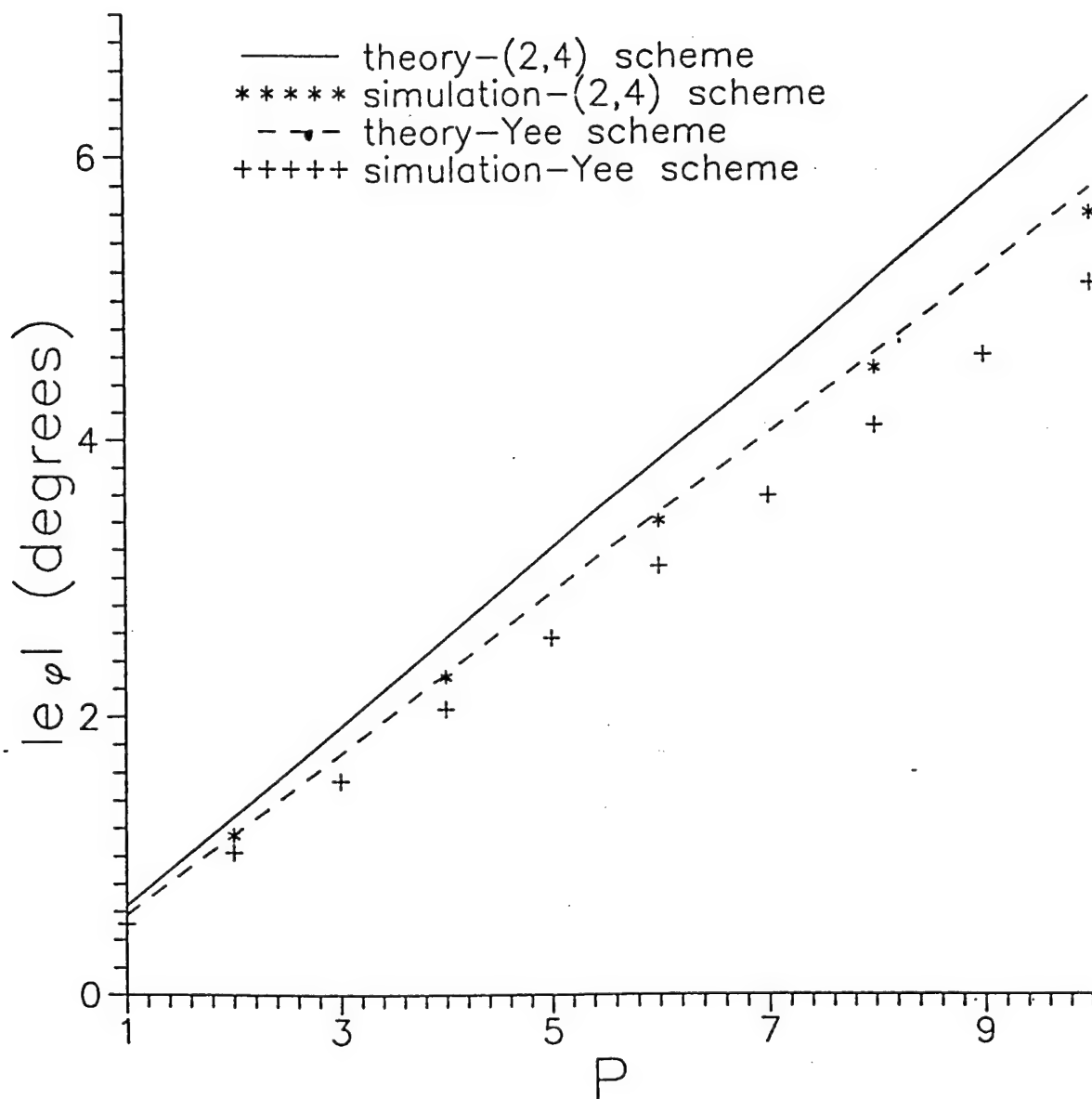


FIGURE 3

Figure 3 Computed e_ϕ versus P for the Yee scheme (stars) and the (2,4) scheme (plus), where $\nu = 0.01$ in both. The theoretical curves are for the Yee scheme from Equation (2.6) for $N_{ppw} = 32$ (dashed line given by $|e_\phi| \sim 0.5783P$), and for the (2,4) scheme from Equation (2.12) for $N_{ppw} = 8$ (solid line given by $|e_\phi| \sim 0.642P$), both for $\theta = 0^\circ$.

with ν small, we have shown the scaling of the error to hold for arbitrary ν provided π/N_{ppw} is small. Employing a small ν in the (2,4) FD-TD is necessary if any benefit is to be gained since the truncation error is $O(\Delta t^2 + \Delta^4)$ so it should be $\Delta t \sim \Delta^2$ for an overall 4th-order accuracy to be obtained. Also, using a small ν will allow for a manageable number of spatial grid cells in the FD-TD for very high frequency applications, for dispersive media (see [13]), and for any problems that require an extremely small timestep. It has been determined that the number of spatial cells can be further reduced by using a 4th-order accurate spatial scheme thus allowing electrically larger problems to be addressed given a fixed quantity of computational resources and of permitted phase error.

References

- [1] R. Lee and A.C. Cangellaris, "A Study of Discretization Error in the Finite Element Approximation of Wave Solutions," *IEEE Trans. Antennas Propagat.*, 40:542 (1992).
- [2] A.C. Cangellaris and R. Lee, "On the Accuracy of Numerical Wave Simulations Based on Finite Methods," *J. Electromag. Wav. Applicat.*, 6:1635 (1992).
- [3] A.F. Peterson and R.J. Baca, "Error in the Finite Element Discretization of the Scalar Helmholtz Equation Over Electrically large Regions," *IEEE Microw. Guided Wave Lett.*, 1:219 (1991).
- [4] K.S. Yee, Numerical Solution of Initial Boundary Value Problems Involving Maxwell's Equations in Isotropic Media, *IEEE Trans. Antennas Propagat.*, 14:302 (1966).
- [5] K. V. Roberts and N. O. Weiss, Convective Difference Schemes, *Mathematics of Computation*, 20:272 (1966).
- [6] M. A. Dablain, The Application of High-Order Differencing to the Scalar Wave Equation, *Geophysics*, 51:54 (1986).
- [7] A. R. Levander, Fourth-Order Finite-Difference P-SV Seismograms, *Geophysics*, 53:1425 (1988).
- [8] J. Fang. "Time Domain Finite Difference Computations for Maxwell's Equations," Ph.D. Dissertation, University of California, Berkeley, CA (1989).

- [9] T. Deveze, L. Beaulieu and W. Tabbara, A Fourth-Order Scheme for the FD-TD Algorithm Applied to Maxwell's Equations, *IEEE-APS International Symposium Proceedings*, pp. 346-349 (1992).
- [10] P. G. Petropoulos, Phase Error Control of FD-TD Type Methods, *Ultra-Wideband Short-Pulse Electromagnetics*, H. Bertoni, L. B. Felsen and L. Carin, eds., pp. 359-366, Plenum, NY (1993).
- [11] J. D. Jackson, *Classical Electrodynamics*, 2nd ed., John Wiley, NY (1975).
- [12] L. Lapidus and G.F. Pinder, *Numerical Solution of Partial Differential Equations in Science and Engineering*, John Wiley, NY (1982).
- [13] P. G. Petropoulos, "Stability and Phase Error Analysis of FD-TD in Dispersive Dielectrics," *IEEE Trans. Antennas Propagat.*, accepted, to appear January 1994.

A General Description of Propagation and Scattering for Electromagnetic Pulses in Dispersive Media

Thomas M. Roberts and Peter G. Petropoulos

We develop some new methods for describing pulse propagation for general dispersive media, using a Debye model for water as an example. Short-pulse, long-pulse, short-time, and long-time approximations are presented. We explain a factor-of-nine effect in the speed of waves in water, which seems to have been previously unnoticed. We also study the following problem: Knowing only the peak amplitude and power density of an incident pulse, what can be said about the peak amplitude of the propagated pulse? We provide sharp upper bounds for the propagated amplitude and reduce the computation of those bounds to a calculator exercise. These bounds may be useful in controlling the electromagnetic interference or damage produced in dispersive media.

1. INTRODUCTION

The computation of electromagnetic pulses in dispersive media is a highly developed field. For instance, a single paper,¹ published in 1976, contains numerics for the propagation of TE- and TM-polarized electromagnetic pulses that are incident obliquely on an inhomogeneous, anomalously dispersive medium. Computational electromagnetics has developed so extensively since 1976 that it now appears that, given enough computer resources, one can compute the propagation of just about any single pulse through just about any single medium. But these studies of single pulses, even of millions of single pulses, have not demonstrated that *every* microwave pulse travels through water² with one-ninth the speed of light in vacuum. That fundamental factor-of-nine effect, which appears to have been unnoticed until now, is established here by studying an electromagnetic wave equation and its scattering operators, which are the natural places to find broadly applicable rules that govern propagation. We will show that the time of arrival of transmitted pulses in anomalously dispersive media is related to a slow speed given by the DC phase velocity in each medium. This paper has several other new results, which relate to the widths and peak amplitudes of pulses, and to quantities that resemble power density. These new results, concerning broad classes of pulses, are validated here using standard numerical methods; a new numerical method for estimating errors is also developed and used, and some results of laboratory experiments on pulse propagation in a muscle-equivalent material are explained. Our results will be shown to be helpful in proposing optimum sample lengths to be used in Time Domain Spectroscopy studies for the accurate determination of the infinite-frequency and static permittivities of Debye-type dispersive media.³⁻⁴ Also, as shown in Section 4, our results can form the basis for a sensitivity analysis of the dependence of the medium response on the parameters obtained from different fits to the same band-limited experimental data.

This work was done, in part, to assist in the development of health-and-safety regulations for electromagnetic pulses in human environments. Our goal was to develop methods to support the regulation of basic quantities such as the peak amplitude and the power density of incident pulses, so that it would not be necessary to regulate every detail of a pulse's time trace. Toward that end

we formulated a problem in making inferences from incomplete data. We asked: Knowing only the peak amplitude and power density of an incident pulse, what can be said about the peak amplitude of the propagated pulse? We also asked what the incomplete data would imply about the values inside the dispersive medium of the time derivative of the magnetic field H and of a different quantity that is related to power density. Of those three quantities—peak amplitude and power density and $\partial_t H$ —it is $\partial_t H$ whose size is most closely linked to the time scale of short-risetime pulses; further, $\partial_t H$ is particularly important because it would be largely responsible for electromotive-force currents in any circuit-like structure that is inside a dispersive medium. Our results in this matter of incomplete data are quite concrete. We will show, for instance, that the peak amplitude of the electric-field part of a propagated microwave pulse is always less than 0.150 V/m, for depths greater than 2.00 mm in water, whenever the incident electric pulse's peak amplitude is less than 1.00 V/m and its power density is less than 5.29×10^{-14} Watt/m², regardless of the other details of the microwave pulse's time trace. We have similar results for power density and for $\partial_t H$. The development of such general rules for pulse propagation may put the computational basis for pulse-safety standards on as firm a basis as for the existing standards⁵ for continuous waves and periodic wave trains.

This paper's dispersion models and time scales are motivated by laboratory experiments. We use a one-term Debye⁶ model that fits laboratory data for water² up to 100 GHz, and our numerical tests involve pulses with or without DC-frequency content whose time scales are characteristic of short-pulse radar. Our methods apply to all other Debye-like media, and can be generalized for the two-term and five-term Debye models that fit laboratory data for muscle and muscle-equivalent materials.³⁻⁴ Our methods can also be generalized for non-Debye media.

2. FORMULATION AND RESULTS

A. PDEs

The equations governing the scattering and propagation of an obliquely incident pulse on a homogeneous dispersive half-space occupying $z \geq 0$ are the time-domain Maxwell's equations for the fields H_x, H_z, E_y . This set of equations is coupled through a polarization current ($\frac{\partial P_y}{\partial t}$) to a differential equation that describes the evolution of an orientational polarization (P_y) mechanism of Debye type⁶ (a relaxation process): $\tau \frac{\partial P_y}{\partial t} + P_y = \Delta \epsilon E_y$, where $\Delta \epsilon = \epsilon_s - \epsilon_\infty$, ϵ_s and ϵ_∞ are respectively the zero- and infinite-frequency relative permittivities, and τ is the dielectric relaxation time. This o.d.e. together with the constitutive law, $D_y = \epsilon_o(\epsilon_\infty E_y + P_y)$, result in the model frequency-domain relative permittivity $\epsilon(\omega) = \epsilon_\infty + \frac{\Delta \epsilon}{1 - i\omega\tau}$, where ϵ_o is the permittivity of vacuum. This model is fitted to frequency-domain experimental data for a range of frequencies ω in order to fix the various medium parameters. Typical values for water in the microwave frequency range are $\epsilon_s = 80.35$, $\epsilon_\infty = 1.00$, $\tau = 8.13$ psec. The phase velocity of each frequency component in such a medium is $v^{phase}(\omega) = \frac{c}{Re\sqrt{\epsilon(\omega)}}$, with c being the speed of light in vacuum. In the subsequent analysis $v^{phase}(0)$ and $v^{phase}(\infty)$ will arise. Finally, operational considerations fix the pulse shape, f , and its duration, T_p .

The electric field incident on the half-space from the air side ($z < 0$) is a plane pulse $E_y^{inc}(x, z, t) = f(t - x \sin \phi_{inc}/c - z \cos \phi_{inc}/c)$ of duration T_p . We assume the pulse has been in contact with the interface since $t = -\infty$. On the interface, $z = 0$, the total electric field is $E_y(x, 0, t) = g(t - x/v)$ where $v = c/\sin \phi_{inc}$; the total field is known by direct measurement of either the field on the interface or of the scattered field in $z < 0$. Defining the time-like variable $\xi = t - x/v$ we find that $E_y(x, z, t) = E_y(0, z, \xi) \rightarrow \bar{E}_y(z, \xi)$, $H_{x,z}(x, z, t) = H_{x,z}(0, z, \xi) \rightarrow \bar{H}_{x,z}(z, \xi)$, and that $\bar{H}_z(z, \xi) = \frac{1}{v\mu_o} \bar{E}_y(z, \xi)$. Changing coordinates $(x, z, t) \rightarrow (z, \xi)$ in the resulting one-dimensional system, and eliminating \bar{H}_y through differentiation with respect to ξ and \bar{P}_y by using the operator $\partial_\xi + \frac{1}{\tau}$, we obtain a single third-order partial differential equation for the electric field $E = \bar{E}_y$ (shown in factored form),

$$\partial_\xi(\partial_\xi - c_o \partial_z)(\partial_\xi + c_o \partial_z)E + \frac{\beta}{\tau}(\partial_\xi - c_1 \partial_z)(\partial_\xi + c_1 \partial_z)E = 0, \quad z > 0, \quad (2.1)$$

where $c_o = c/(\sqrt{\epsilon_\infty} \cos \phi_{inc})$, $\beta = 1 + \Delta \epsilon/(\epsilon_\infty \cos^2 \phi_{inc})$, and $c_1 = c_o/\sqrt{\beta}$. For $\phi_{inc} = 0$,

$\xi = t$. The signaling problem for (2.1) is completed by giving the boundary condition $E(0, \xi) = g(\xi)$, and the initial data $E(z, 0) = E_\xi(z, 0) = E_{\xi\xi}(z, 0) = 0$. \tilde{H}_z follows once E is known, and $\tilde{H}_z = \frac{1}{\mu_0} \int_0^\xi \frac{\partial \tilde{E}(z, \xi')}{\partial z} d\xi'$. The following results are derived in Subsection 3A.

Equation (2.1) describes the propagation of all possible waves of different orders, and their corresponding speeds, that can be excited by an arbitrary pulse. The coefficients exhibit an explicit dependence on the angle of incidence, and on the parameters that describe the medium. It is a strictly hyperbolic⁷ partial differential equation since the principal part of the operator has real distinct eigenvalues (three eigenvalues, $\pm c_0$ and 0), and a complete set of eigenvectors. Causality follows from this last sentence. The characteristic contributed by the zero eigenvalue can be visualized by considering that $\partial_\xi + c_2 \partial_z = \partial_\xi$ when $c_2 = 0$. The main feature of (2.1) is the two wave equations exhibiting distinct speeds, c_0 and c_1 . Pulse propagation is governed by these two speeds in mutually exclusive spatial regions. Disturbances mainly described by the principal part of the operator in (2.1) will be called high-order waves, while those described by the remaining operator will be called lower-order waves.⁸ The speed c_1 , while not a characteristic speed (it is sub-characteristic, $c_1 < c_0$), is important in the analysis and has several ramifications for experiments. Also, $c_1 = v^{phase}(0)$ and $c_0 = v^{phase}(\infty)$; i.e., the main disturbances will propagate with the distinct speeds which are equal to limiting values of the phase velocity. It is worthwhile to emphasize that experimental data indicates $c_1 \ll c_0$, e.g., $c_1 \sim 0.1116c_0$ for water in the microwave range; the problem is stiff so the pulse travels in the half-space with either of two speeds that are disparate.

The high-order term describes the dominant behavior for depths $z < O(c_0\tau)$ m, and the effect of the lower-order term on the the high-order waves is an exponential decay with z . The penetrating pulse propagates with speed c_0 in this shallow depth ($\sim 10^{-4}$ m for water) which we name the "skin-depth" for pulses since it is reminiscent of the well known frequency-domain concept.² From experimentally obtained data typical of tissue $\tau = O(10^{-12})$ sec, and $\beta = O(10)$. Thus $\frac{\beta}{\tau}$ is large, and we expect the bulk of the penetrated pulse to travel with the speed c_1 since (2.1) is then approximately $E_{\xi\xi} - c_1^2 E_{zz} = 0$. The main disturbance will be a lower-order wave. The effect of the high-order term on the lower-order waves, which travel with speed

c_1 , is diffusive in character and important for $z > O(c_0\tau)$ m. The main response diffuses around the ray $z_s = c_1\xi$ on which the peak of the response is found. The peak amplitude on the sub-characteristic ray decays as $1/\sqrt{z}$, or as $1/\sqrt{\xi}$ (for fixed depth). A consequence of this is that the peak of the energy-like quantity E^2 will decay as $1/z$ ($1/\xi$).

The response will also depend crucially on the pulse duration. This parameter appears through scaling ξ with T_p , and z with cT_p . Now $\frac{\beta}{\tau} \rightarrow \frac{\beta T_p}{\tau}$, and c_0 and c_1 are normalized by c . Pulses with appreciable amplitude most often have $T_p \sim 10^{-8} - 10^{-10}$ sec, so $\frac{\beta T_p}{\tau}$ is still large. Pulses that are long with respect to the relaxation time ($T_p \rightarrow \infty$, or equivalently if $\tau \rightarrow 0$) will propagate unattenuated in the half-space with amplitude equal to the DC value of the frequency-domain transmission coefficient regardless of the pulse's DC-frequency content. The field just after the interface (no "skin-depth" since $c_0\tau \rightarrow 0$) satisfies a lossless wave equation with speed c_1 . On the other hand, very short pulses ($T_p \rightarrow 0$, or equivalently if $\tau \rightarrow \infty$) will not penetrate far. In this case the electric field in the half-space (since now $c_0\tau \rightarrow \infty$) sees a high constant conductivity medium thus it satisfies a telegraphers wave equation whose far-field is the diffusion equation.

B. Green Functions

This subsection describes some rules of wave propagation that are derived from time-domain Green functions. The history of these Green functions is reviewed in Subsection 3B. We will first state some results involving upper bounds on propagated peak amplitudes and power-density-type quantities. These upper bounds are easily computed and they are independent of the detailed nature of the incident fields. The bounds are developed for normal incidence here and for oblique incidence in Subsection 3B. The present section concludes with a description of wave speeds and with brief-pulse and long-pulse approximations. These rules are all illustrated numerically using the water parameters $\epsilon_s = 80.35$, $\epsilon_\infty = 1.00$, and $\tau = 8.13$ psec from Subsection 2A; and the results are easily generalized to other Debye media and to non-Debye media. The necessary derivations and numerical validations are in Subsection 3B and Appendix A.

For normal incidence, let the y -polarized incident electric field be $f(t - z/c_0)$ in the air-filled half-space $z < 0$. In the water-filled half-space $z \geq 0$, the resulting electric field is

$$E(z, t) = E_y(z, t) = \exp\left(\frac{-z}{6.15 \times 10^{-5} \text{m}}\right) f\left(t - \frac{z}{c_0}\right) + \int_0^{t-z/c_0} ds f(s) G_E(z, t-s). \quad (2.2)$$

The Green function $G_E(z, t)$ is graphed in Fig. 1 for several depths $z > 0$. For the boundary $z = 0$, Ref. 9 derives $G_E(0, t) = -t^{-1} \exp[-t/(2.00 \times 10^{-13} \text{s})] I_1[t/(2.05 \times 10^{-13} \text{s})]$, where I_1 is the modified Bessel function of the first kind; the oblique-incidence generalization is (3.12). The magnetic field $H_x(z, t) = -\int_{z/c_0}^t ds \partial_z E_y(z, s)/\mu_0$ also has a Green-function representation similar to (2.2).

Many of our new results are based on (2.2) and Fig. 1. Safety standards may be affected by this type of analysis; so, in Appendix A, we show how to estimate the percentage error in computations, with the following results for our computations: (1) The pointwise numerical error in $G_E(0.500 \text{ mm}, t)$ is no more than 1.70% of the peak value (with respect to t) of $|G_E(0.500 \text{ mm}, t)|$; (2) The pointwise numerical error in $G_E(4.00 \text{ mm}, t)$ is no more than 0.800% of the peak

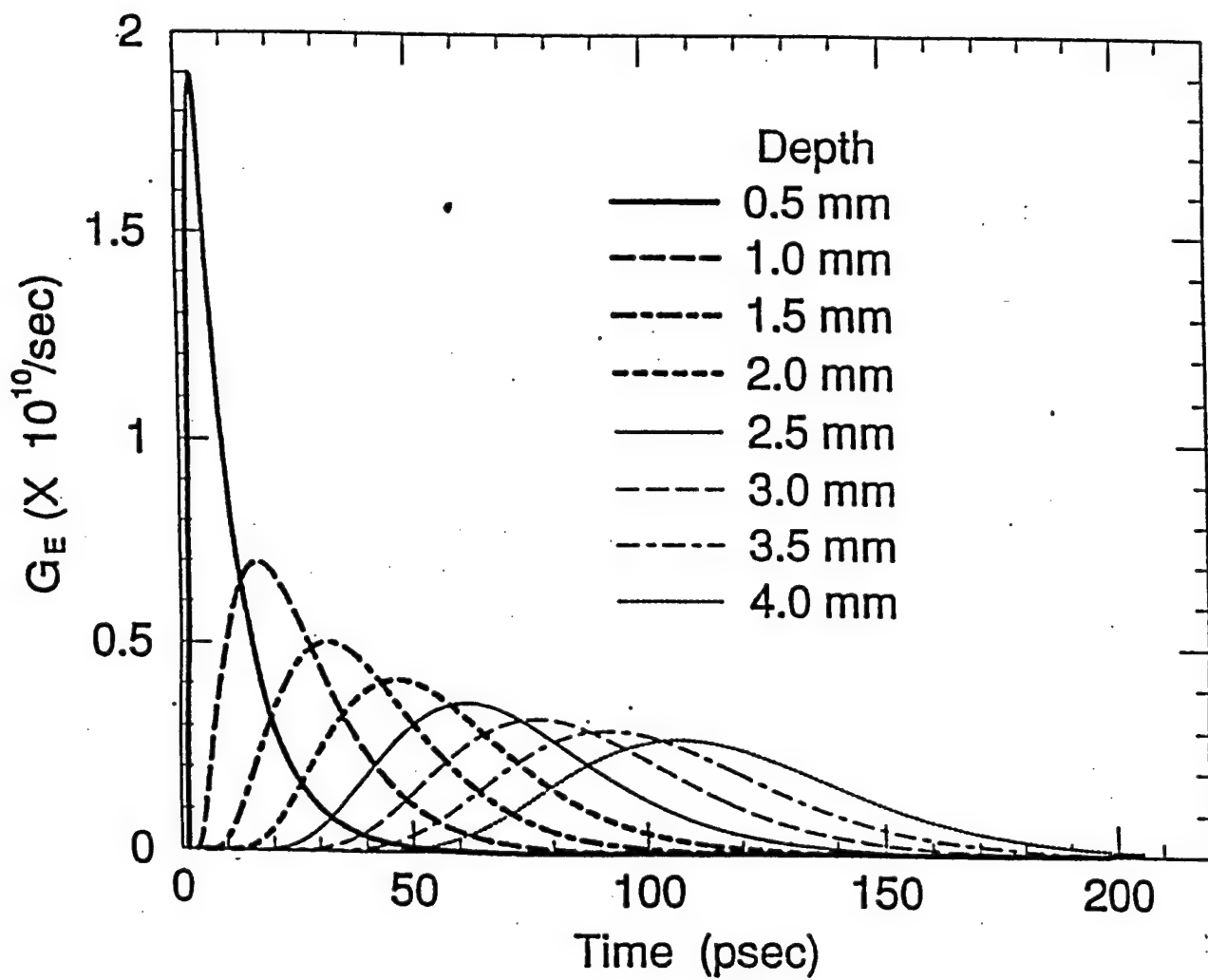


Fig. 1. The time dependence of the Green function $G_E(z, t)$ for water at several depths z .

value of $|G_E(4.00 \text{ mm}, t)|$; and (3) For intermediate depths, the relative error in $G_E(z, t)$ decreases monotonically from 1.70% at $z = 0.500 \text{ mm}$ to 0.800% at $z = 4.00 \text{ mm}$. The closed-form expression for $G_E(0, t)$ is exact.⁹

We will use the following three norms:

$$\begin{aligned}\|h(z, \cdot)\|_1 &= \int_0^\infty dt |h(z, t)| \\ \|h(z, \cdot)\|_2 &= \left(\int_0^\infty dt |h(z, t)|^2 \right)^{1/2} \\ \|h(z, \cdot)\|_\infty &= \text{least upper bound of } |h(z, \cdot)|,\end{aligned}\tag{2.3}$$

where, for each depth z , the least upper bound $\|h(z, \cdot)\|_\infty$ is evaluated with respect to t . Then, for each depth z from 0.500 mm through 4.00 mm,

$$\|E(z, \cdot)\|_\infty \leq \|f(\cdot)\|_\infty \exp\left(\frac{-z}{6.15 \times 10^{-5} \text{ m}}\right) + \min \left[\begin{array}{l} (0.202) \|f(\cdot)\|_\infty, \\ F_1(z) \|f(\cdot)\|_2, \\ F_2(z) \|f(\cdot)\|_1 \end{array} \right], \tag{2.4}$$

regardless of the detailed nature of the incident electric field $f(t)$. The right side of (2.4) is easily computed, given the functions $F_1(z) = \|G_E(z, \cdot)\|_2$ and $F_2(z) = \|G_E(z, \cdot)\|_\infty$, which are graphed in Fig. 2. Inequality (2.4) defines upper bounds on the peak amplitudes of $E(z, \cdot)$. This inequality, and all of our other Green-function results, are validated numerically in Subsection 3B. The upper bound on the right side of (2.4) is almost attained in one of the numerical validations. In that sense, the upper bound is sharp.

We will now show how relation (2.4) could be used in a safety standard for the peak amplitudes of internal electric fields. Suppose, for this hypothetical example, that it has been determined that peak electric fields must be no greater than 0.200 V/m at depths greater than 1.00 mm, and no greater than 0.150 V/m at depths greater than 3.00 mm. That hypothetical internal-field standard is translated, using (2.4) and Fig. 2, into a more easily regulated standard on incident electric fields $f(t)$. The easily regulated standard is

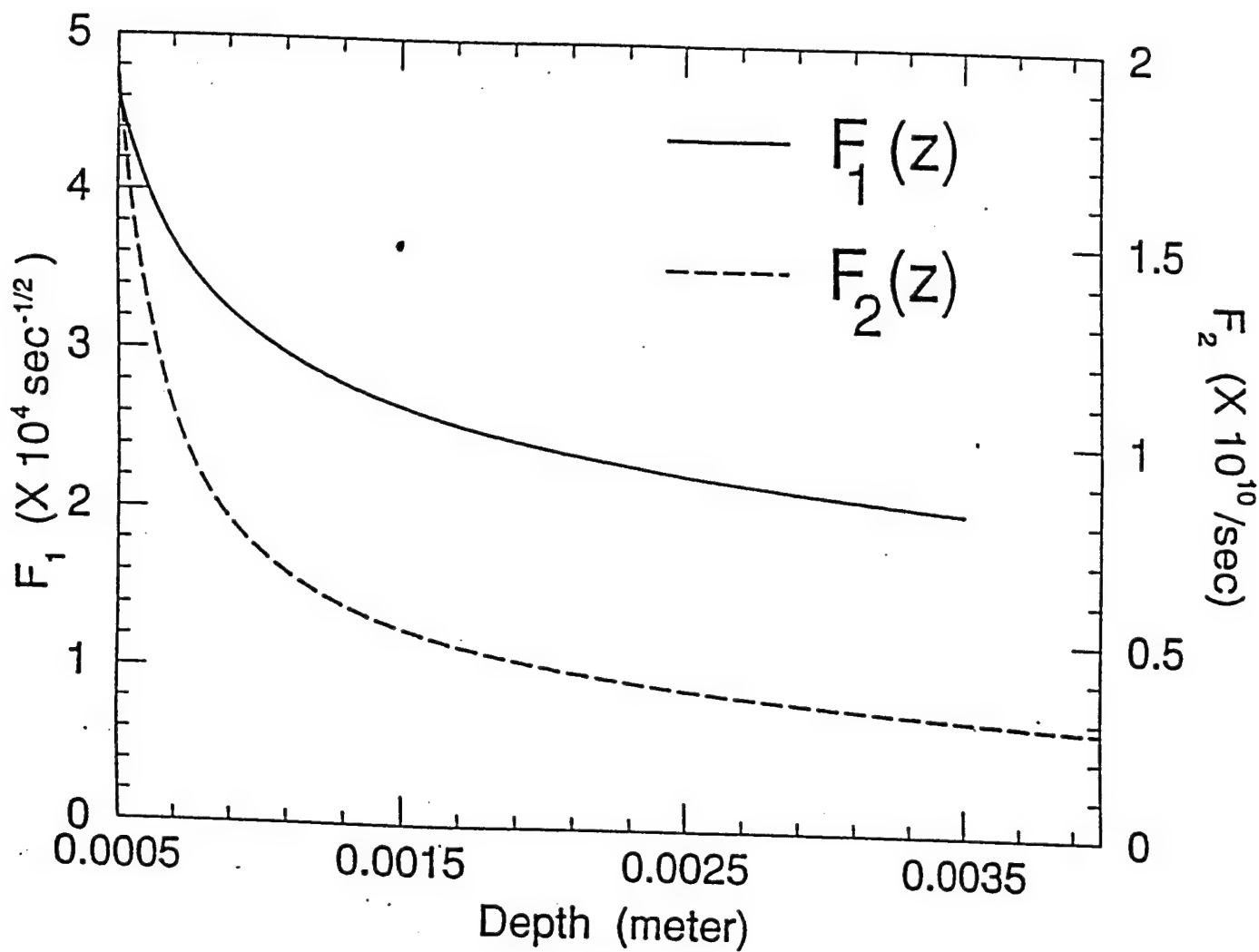


Fig. 2. The L_2 norm $F_1(z)$ and the L_∞ norm $F_2(z)$ of the Green function $G_E(z, \cdot)$ for water. These norms and Eqn. (2.4) reduce the upper-bound computations to a calculator exercise.

(1) Peak value of $|f(t)| \leq 0.740$ V/m or

(2) $\left[\text{Peak value of } |f(t)| \leq 40,000 \text{ V/m and } \int_0^\infty dt |f(t)|^2 \leq 4.00 \times 10^{-11} \text{ V}^2\text{s/m}^2 \right]$ or

(3) $\left[\text{Peak value of } |f(t)| \leq 50,000 \text{ V/m and } \int_0^\infty dt |f(t)| \leq 2.80 \times 10^{-11} \text{ Vs/m} \right]$.
(2.5)

By reading the two graphs in Fig. 2 and using a calculator, one can use (2.4) to show that any incident field that satisfies item (1) or item (2) or item (3) of (2.5) is guaranteed to produce internal fields that comply with the hypothetical internal-field standard, regardless of all other details of $f(t)$.

Upper bounds also exist for quantities that resemble power densities.¹⁰ In particular, for any incident field $f(t)$ and for each depth z from 0.500 mm through 4.00 mm, the power-density-type term¹⁰ $\|E(z, \cdot)\|_2^2 = \int_0^\infty dt |E(z, t)|^2$ satisfies

$$\int_0^\infty dt |E(z, t)|^2 \leq \left\{ \|f(\cdot)\|_2 \exp\left(\frac{-z}{6.15 \times 10^{-5} \text{ m}}\right) + \min \left[\frac{(0.202) \|f(\cdot)\|_2}{F_1(z) \|f(\cdot)\|_1} \right] \right\}^2. \quad (2.6)$$

Subsection 3B numerically validates the inequality in (2.6), showing that the upper bound on the right side of (2.6) is almost attained in at least one case.

We will now show how the upper bounds in (2.6) could be used in a safety standard for an power-density-type quantity related to internal electric fields. Suppose, for this hypothetical example, that it has been determined that the power-density-type quantity $\int_0^\infty dt |E(z, t)|^2$ must be no greater than $1.50 \times 10^{-12} \text{ V}^2\text{s/m}^2$ at depths greater than 1.00 mm, and no greater than $1.00 \times 10^{-12} \text{ V}^2\text{s/m}^2$ at depths greater than 3.00 mm. Equation (2.6) and Fig. 2 translate this hypothetical standard for internal fields into a more easily regulated standard on incident electric fields $f(t)$:

$$\begin{aligned}
(1) \quad & \int_0^\infty dt |f(t)|^2 \leq 2.40 \times 10^{-11} \text{ V}^2 \text{ s/m}^2 \quad \text{or} \\
(2) \quad & \left[\int_0^\infty dt |f(t)|^2 \leq 36.0 \text{ V}^2 \text{ s/m}^2 \quad \text{and} \quad \int_0^\infty dt |f(t)| \leq 3.90 \times 10^{-11} \text{ V s/m} \right].
\end{aligned} \tag{2.7}$$

Subsection 3B shows that some pulses almost attain the upper bounds in (2.6), which was used to obtain (2.7).

The upper-bound concepts in (2.4) and (2.6) are easily extended to magnetic fields and their time derivatives, and to oblique incidence. Subsection 3B has numerical results for all of those extensions. One can see there that making the angle of incidence more oblique will decrease the penetration into the medium of power-density-type quantities and also peak electric and magnetic fields. A related closed-form, modified-Bessel-function expression for the oblique-incidence reflection kernel $R^\theta(t) = G_{E,\theta}(0,t)$ is given in (3.12).

We will now state some Green-function results concerning wave speeds. These results are derived in Subsection 3B. For simplicity, the results are stated for normal incidence. Our first conclusion is that the main bulk of an electromagnetic pulse travels through water with speed c_0 for 0.3 mm, and then slows until, for all depths beyond 0.7 mm, the pulse travels with the constant speed $c_0/9.0$. That behavior contrasts with the wavefront speed, which is mathematically well defined but is not always observable in a laboratory. The wavefront speed is precisely c_0 for all depths.¹¹ Section 4 discusses various Debye models that are consistent, to within about 10%, with the band-limited water data² used here. The large-depth speeds (all $\approx c_0/9.0$) for those Debye models vary by only about 10%. The shallow-depth speed and the wavefront speed of any Debye model, however, are both equal to $c_0 = 1/\sqrt{\mu_0 \epsilon_\infty}$. The shallow-depth and wavefront speeds, consequently, change considerably as one varies the Debye parameter ϵ_∞ from 1.00 through 10.0, as described in Section 4. Therefore, a measurement of the wavefront speed or the shallow-depth speed would determine the Debye parameter ϵ_∞ .

We conclude with some Green-function results concerning short-pulse and long-pulse approximations. The propagation of any finite-valued incident electric

pulse $f(t)$ is given simply by (2.2) and Fig. 1. We get additional insight by considering approximations for what we will call elemental pulses f_e : An element $f_e(t)$ is zero except on a single time interval, during which it is either strictly negative or strictly positive. For instance, a square pulse is an element, but a one-cycle sinusoid is not an element. Elements are important because any incident pulse f is a sum of positive-valued elements and negative-valued elements. If the duration of an element $f_e(t)$ is much briefer than 30 psec, then the propagated pulse element is approximately $\|f_e(\cdot)\|_1 G_E(z, t)$ (see Fig. 1) for all depths greater than 0.7 mm. If the duration of an element $f_e(t)$ is much longer than 50 psec, then the propagated pulse element is approximately $0.2f_e[t - 9.0(z - 1 \text{ mm})/c + 17 \text{ psec}] = 0.2f_e(t - 9.0z/c - 13 \text{ psec})$ for all depths from 1 mm through the depth at which the duration of $G_E(z, t)$ becomes comparable to the duration of $f_e(t)$. These approximations are derived in Subsection 3B.

3. DERIVATIONS

A. PDEs

To extract from (2.1) the equation describing the early-time evolution (in the "skin-layer") of the response we set everywhere in (2.1) $\partial_\xi \sim -c_o \partial_z$ except in the operator $\partial_\xi + c_o \partial_z$ since it expresses the propagation of the high-order waves. Any other terms in the resulting equation will describe the effect of the lower-order waves. The main disturbance for early times is modeled by

$$(\partial_\xi + c_o \partial_z)E + \frac{\beta}{\tau} \frac{c_o^2 - c_1^2}{2c_o^2} E = 0; \quad z < c_o \tau, \quad (3.1)$$

subject to the boundary condition $E(0, \xi) = g(\xi)$. The solution of (3.1) is

$$E(z, \xi) = g\left(\xi - \frac{z}{c_o}\right) \exp \left[- \left(\frac{\epsilon_s/\epsilon_\infty - 1}{2 \cos^2 \phi_{inc}} \right) \left(\frac{z}{c_o \tau} \right) \right]. \quad (3.2)$$

We see that the response decays exponentially in a thin region of depth $z \sim O(c_o \tau)$, where the speed of propagation is c_o . Note that the decay constant is inversely proportional to $\cos^2 \phi_{inc}$ thus normal incidence will result in the greatest amplitude in the medium. To describe the evolution of the lower-order waves, which travel with speed c_1 , we set in (2.1) $\partial_\xi \sim -c_1 \partial_z$ except in the operator $\partial_\xi + c_1 \partial_z$ which expresses the hyperbolic nature of the lower-order waves. The main disturbance is now modeled by

$$(\partial_\xi + c_1 \partial_z)E = \frac{\tau}{\beta} \frac{c_o^2 - c_1^2}{2} \partial_z^2 E; \quad z > c_o \tau. \quad (3.3)$$

The boundary condition is approximately $E(z_o, \xi') = h(\xi')$, where z_o is the depth after which (3.1) no longer applies, ξ' is the time with origin at z_o/c_o (the time it takes for the pulse to reach z_o in the "skin-depth"), and $h(\xi')$ represents (3.2) evaluated at z_o . Equation (3.3) is an advection-diffusion equation, and describes the response after a depth of $O(c_o \tau)$ m. The peak of the response is on the sub-characteristic ray $z_s = c_1 \xi'$. The solution is very easily obtained from the solution of the diffusion equation. It is¹²

$$E(z, \xi') = \sqrt{\frac{\beta}{2\pi\tau(c_o^2 - c_1^2)}} z \times \int_0^{\xi'} d\kappa \frac{h(\kappa)}{(\xi' - \kappa)^{\frac{3}{2}}} \exp \left(- \left[\frac{\beta}{2\tau(c_o^2 - c_1^2)} \right] \left\{ \frac{[z - c_1(\xi' - \kappa)]^2}{\xi' - \kappa} \right\} \right). \quad (3.4)$$

Various techniques can be used to estimate the integral in (3.4) since β/τ is large. Here we are interested only in the primary behavior of E as a function of depth. For $\frac{\beta}{\tau} \gg 1$ the response is

$$E^\delta(z, \xi') = h(0) \sqrt{\frac{\beta}{2\pi\tau(c_0^2 - c_1^2)}} \frac{z}{\xi'^{\frac{3}{2}}} \exp \left\{ - \left[\frac{\beta}{2\tau(c_0^2 - c_1^2)} \right] \left[\frac{(z - c_1\xi')^2}{\xi'} \right] \right\}. \quad (3.5)$$

On $z_* = c_1\xi'$ we find that $\max\{E^\delta\} \sim 1/\sqrt{z}$, or $\sim 1/\sqrt{\xi'}$. This is verified with the numerical experiments in Section 4.

B. Green Functions

This subsection derives our Green-function results in the order in which they are described in Subsection 2B. Equation (2.2), for instance, is a Green-function representation. These Green functions have become a standard technique in computational electromagnetics. They were first developed for non-dispersive media,¹³ and were then used to compute fields in dispersive media.¹⁴ That dispersive-medium work has not yet been published, owing to the death of R. Krueger, but generalizations are available.¹⁵⁻¹⁷ The Green function programs used in the present paper were developed by the authors of Ref. 16, along the lines of Appendix A of that paper.

The L_∞ and L_2 norms in (2.3) have special physical significance. The L_2 norm is important because $(c\epsilon_0/2)(\|E\|_2)^2$ is the power density, whose mks units are Watt/m², of an electric pulse in free space.¹⁰ Consequently, we will focus on the peak-value ($p = \infty$) and power-density ($p = 2$) cases of the inequalities

$$\|E(z, \cdot)\|_p \leq e^{-az} \|f(\cdot)\|_p + \|G(z, \cdot)\|_r \|f(\cdot)\|_q, \quad (3.6)$$

which are obtained by applying the Young theorem¹⁸ to (2.2), and for which $a = 1.63 \times 10^4 \text{ m}^{-1}$. In particular, although (3.6) is valid whenever $1 \leq p, q, r \leq \infty$ satisfy $r^{-1} = 1 + p^{-1} - q^{-1}$, we are most interested in the cases

$$\|E(z, \cdot)\|_\infty \leq e^{-az} \|f(\cdot)\|_\infty + \min \begin{bmatrix} \|G_E(z, \cdot)\|_1 \|f(\cdot)\|_\infty, \\ \|G_E(z, \cdot)\|_2 \|f(\cdot)\|_2, \\ \|G_E(z, \cdot)\|_\infty \|f(\cdot)\|_1 \end{bmatrix} \quad (3.7)$$

and

$$[\|E(z, \cdot)\|_2]^2 \leq \left\{ e^{-az} \|f(\cdot)\|_2 + \min \begin{bmatrix} \|G_E(z, \cdot)\|_1 \|f(\cdot)\|_2, \\ \|G_E(z, \cdot)\|_2 \|f(\cdot)\|_1 \end{bmatrix} \right\}^2. \quad (3.8)$$

In numerical computations for water, $\|G_E(z, \cdot)\|_1$ was observed to decrease slowly and monotonically from 0.2019 at 0.5 mm to 0.2014 at 3.5 mm. It is as if, for those depths in water, the advection-diffusion equation (3.3) were approximated by a heat equation and $G_E(z, t)$, which is positive valued for depths beyond 0.5 mm, were analogous to a temperature distribution whose total conserved heat is proportional

to $\|G_E(z, \cdot)\|_1$. Equations (3.6)–(3.8), the almost-constant nature of $\|G_E(z, \cdot)\|_1$, and numerical Green-function computations produced the results in (2.4)–(2.7).

We now consider five numerical examples that validate the inequalities in (2.4). We will see that the minimum upper bounds in (2.4) are almost attained for some incident pulses. For these five examples, we choose the following hypothetical restrictions on the incident electric pulses $f(t)$:

$$\begin{aligned} \|f(\cdot)\|_\infty &\leq 1.00 \text{ V/m and} \\ \|f(\cdot)\|_2 &\leq 6.32 \times 10^{-6} \text{ Vs}^{1/2}/\text{m and} \\ \|f(\cdot)\|_1 &\leq 4.00 \times 10^{-11} \text{ Vs/m.} \end{aligned} \tag{3.9}$$

Then (2.4) shows that any incident pulse f that satisfies (3.9) will produce an internal field whose peak amplitude satisfies

$$\|E(z, \cdot)\|_\infty \leq \left[\exp\left(\frac{-z}{6.15 \times 10^{-5} \text{ m}}\right) \text{ V/m} \right] + \min \left[\begin{array}{c} 0.202 \text{ V/m,} \\ (6.32 \times 10^{-6} \text{ Vs}^{1/2}/\text{m}) F_1(z), \\ (4.00 \times 10^{-11} \text{ Vs/m}) F_2(z) \end{array} \right], \tag{3.10}$$

where $F_1(z)$ and $F_2(z)$ are graphed in Fig. 2. Each sum of the exponential in (3.10) and a term from the “min” clause of (3.10) yields one of the three top-most, boldface curves in Fig. 3. Relation (3.10) guarantees that the depth-dependent peak amplitudes of $E(z, \cdot)$ are less than the minimum of the three boldface upper-bound graphs. That prediction was tested using five incident pulses f that comply with (3.9). Those incident pulses are: (1) a 40-psec-duration square pulse with 1-V/m amplitude; (2) the absolute value $f_2(t) = |f_4(t)|$ of the 4-cycle, 80-GHz sinusoid in item 4 below; (3) the absolute value $f_3(t) = |f_5(t)|$ of the 1-cycle, 80-GHz sinusoid in item 5 below; (4) a 4-cycle 80-GHz sinusoid with 1-V/m amplitude; and (5) a 1-cycle 80-GHz sinusoid with 1-V/m amplitude. The norms of the pulses, which are tabulated below, all satisfy (3.9).

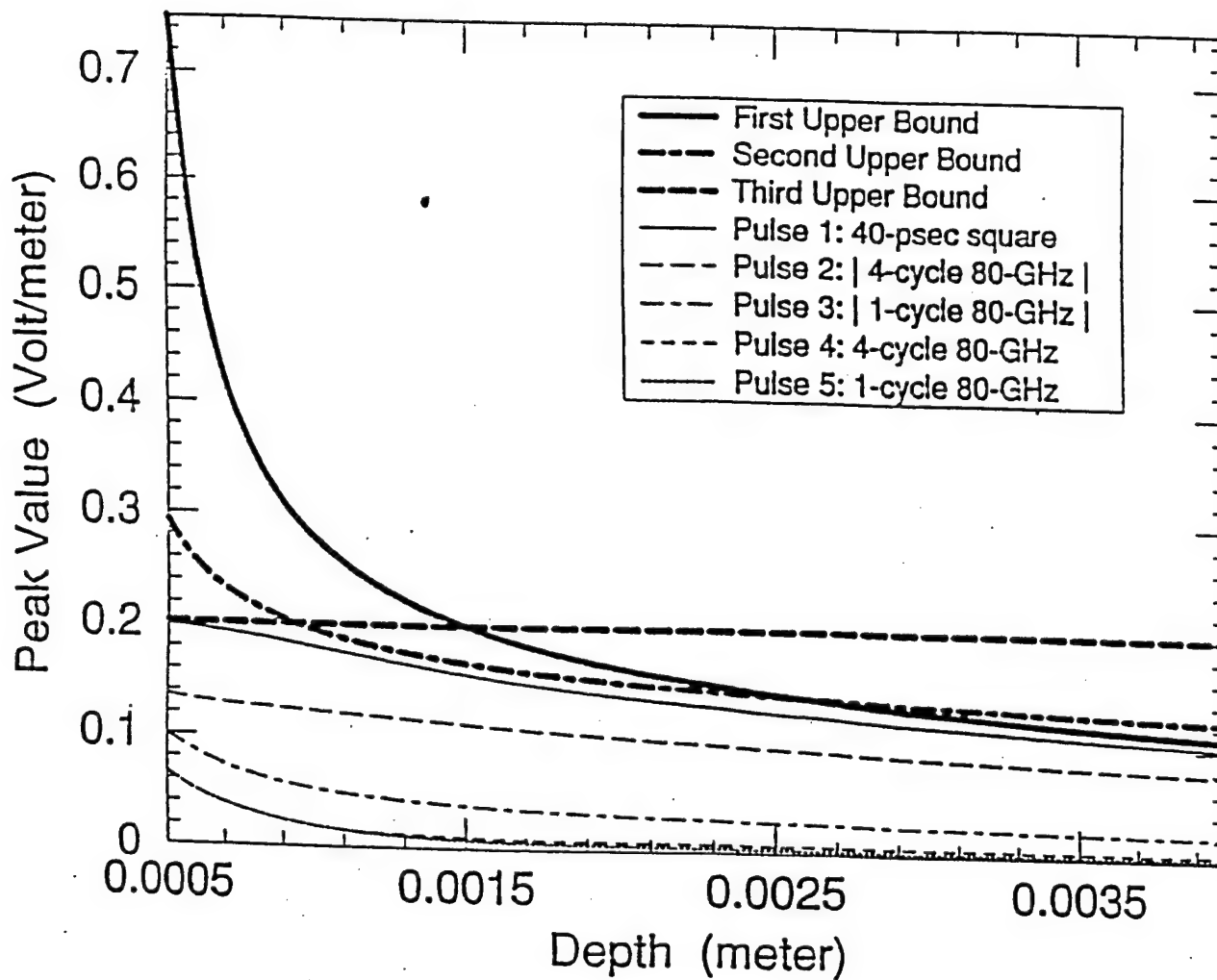


Fig. 3. Five numerical validations of the upper-bound concept for the depth-dependent peak amplitudes of $E(z, \cdot)$. The boldface curves are upper bounds from relation (3.10).

Table 1. Five incident pulses that satisfy the conditions in (3.9). The first incident pulse is 1 V/m for $0 \leq t \leq 40$ psec, and it is 0 for all other times. The second pulse is the absolute value of $(1\text{V/m}) \sin[2\pi t/(8 \times 10^{10}\text{s})]$ for $0 \leq t \leq 50$ psec, and it is 0 for all other times.

Example	Duration	Type	$\ \cdot\ _\infty$ (V/m)	$\ \cdot\ _2$ (Vs ^{1/2} /m)	$\ \cdot\ _1$ (Vs/m)
1	40-psec	square pulse	1.00	6.32×10^{-6}	4.00×10^{-11}
2	4 cycles	80-GHz sine	1.00	5.00×10^{-6}	3.18×10^{-11}
3	1 cycle	80-GHz sine	1.00	2.50×10^{-6}	7.96×10^{-12}
4	4 cycles	80-GHz sine	1.00	5.00×10^{-6}	3.18×10^{-11}
5	1 cycle	80-GHz sine	1.00	2.50×10^{-6}	7.96×10^{-12}

The peak amplitudes of the five internal fields $E(z, \cdot)$, corresponding to the above-tabulated incident fields, are also graphed in Fig. 3; the curves for Examples 4 and 5 almost overlap. Those peak amplitudes are all less than the (boldface) upper bounds described earlier. The five examples, therefore, numerically validate the upper bound concept in (2.4). Fig. 3 also shows that the upper bounds are sharp in the sense that the peak amplitude of one pulse (Example 1) almost attains the minimum upper bound. That example involves a pulse with a nonzero DC-component¹⁹⁻²¹ $\int_0^\infty dt f(t)$. It makes intuitive sense that the presence of a DC component in a pulse would tend to diminish the attenuation of the pulse in any medium, as an elementary analysis²² affirms for a non-Debye medium.

Having just validated the upper-bound concept (2.4) for peaks, we now validate (2.6): The two top-most, boldface curves in Fig. 4 correspond to the upper bounds $(e^{-az}\|f\|_2 + \|G_E\|_1\|f\|_2)^2$ and $(e^{-az}\|f\|_2 + \|G_E\|_2\|f\|_1)^2$ in (2.6), subject to the hypothetical restriction (3.9). The other five curves represent the power-density-type quantities $[\|E_x(z, \cdot)\|_2]^2$ produced by the five incident fields in Table 1. We

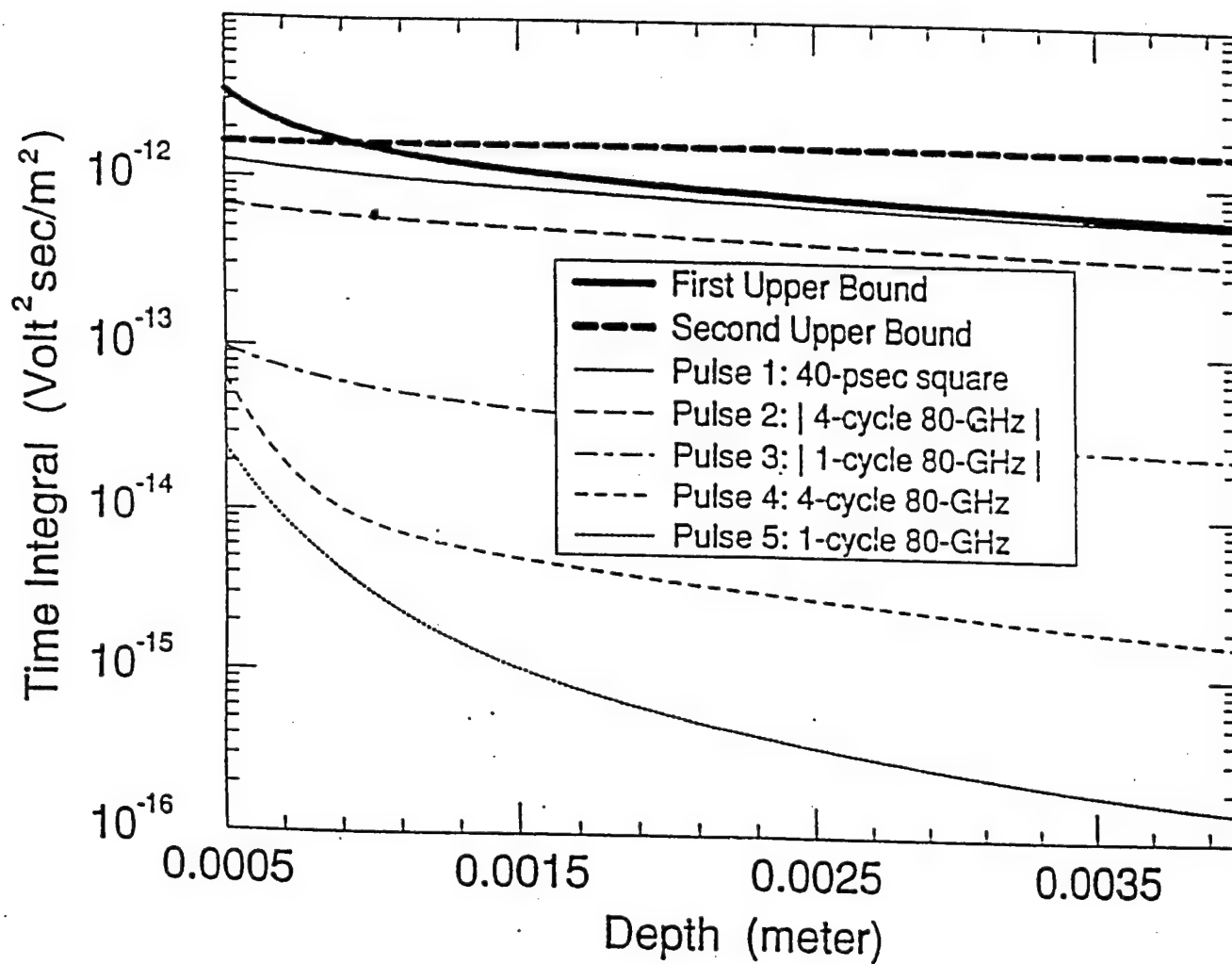


Fig. 4. Five numerical validations of the upper-bound concept for the power-density-type time integral $\int_0^\infty dt |E(z, t)|^2$. The boldface upper bounds are from relation (2.6).

see that the field produced by Example 1 of Table 1 almost attains the minimum upper bound in Fig. 4. This completes our validation of the upper-bound concepts.

As explained above (2.1), oblique incidence is taken into account using a simple, widely-known transformation of variables. Using the transformation, we obtain numerical results for 45°-incident electric fields $f[t - (x + z)/(\sqrt{2}c)]$. In water ($z \geq 0$) the y component of the electric field is

$$E(x, z, t) = E\left(0, z, t - \frac{x}{\sqrt{2}c}\right)$$

$$E(0, z, t) = \exp\left(\frac{-z}{4.35 \times 10^{-5} \text{m}}\right) f\left(t - \frac{z}{\sqrt{2}c}\right) + \int_0^{t-z/(\sqrt{2}c)} ds f(s) G_{E,45^\circ}(z, t-s). \quad (3.11)$$

The function $G_{E,45^\circ}(z, t)$ is graphed in Fig. 5 for several depths $z > 0$. The numerical errors in Fig. 5 were quantitatively estimated using the method of Appendix A. The results are: (1) For each depth z , from 0.160 mm through 2.88 mm, the error in the computed values of $G_{E,45^\circ}(z, t)$ are no more than 3.19% of the peak value, with respect to time, of the actual values $|G_E(z, t)|$; and (2) The relative errors decrease, but not necessarily monotonically, from 3.19% at 0.160 mm to 2.07% at 2.88 mm. At the boundary $z = 0$ and for all $t > 0$, $G_{E,45^\circ}(0, t) = -t^{-1} \exp[-t/(1.01 \times 10^{-13} \text{s})] I_1[t/(1.03 \times 10^{-13} \text{s})]$, where I_1 is the modified Bessel function of the first kind. More generally, the oblique-incidence transformation and Ref. 9 imply, for all $t > 0$, that

$$R^\theta(t) = G_{E,\theta}(0, t) = \frac{-1}{t} \exp\left[-\left(b + \frac{a}{2\varepsilon_\infty \cos^2 \theta}\right)t\right] I_1\left(\frac{at}{2\varepsilon_\infty \cos^2 \theta}\right). \quad (3.12)$$

That exact result uses the modified Bessel function of the first kind to represent the reflections in the air-filled half-space ($z < 0$) that are caused by waves that are incident obliquely on the Debye half-space ($z \geq 0$) defined by

$$D(z, t) = \begin{cases} \varepsilon_\infty \varepsilon_0 E(z, t), & z < 0 \\ \varepsilon_\infty \varepsilon_0 E(z, t) + a\varepsilon_0 \int_0^t ds e^{-b(t-s)} E(z, s), & z \geq 0 \end{cases} \quad (3.13)$$

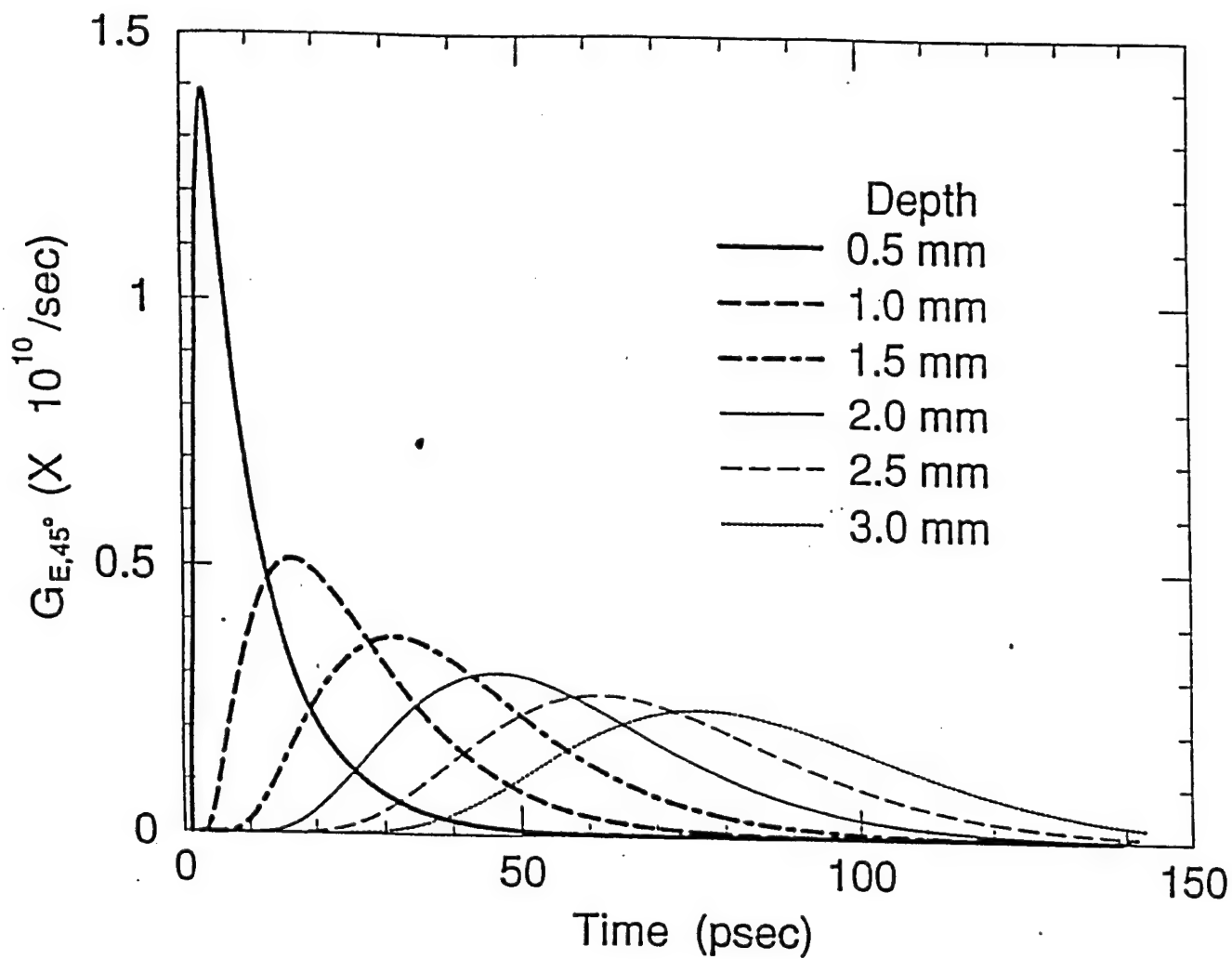


Fig. 5. The time dependence of the Green function $G_{E,45^\circ}(z, t)$ for several depths z . This Green function is used for pulses that are incident on water at an angle of 45° .

In particular, the reflected field is exactly $\int_0^t ds f(s) R^\theta(t-s)$ for any incident field f . Equation (3.12) was used numerically to validate the $z = 0$ boundary values of the oblique-incidence Green-function computations that yielded Figs. 5, 6 and 8. Equation (3.12) was also used to validate, at $z = 0$, the previous percentage-error estimates for oblique incidence. At $z = 0$, the estimated relative error was 1.91%; the true relative error was 1.87%.

Applying the Young-theorem result (3.6) to the oblique-incidence representation (3.11) yields obvious oblique-incidence generalizations of the upper-bound results (2.4)–(2.6); for instance, $\|E(0, z, \cdot)\|_2 \leq \|f(\cdot)\|_2 \exp[-z/(4.35 \times 10^{-5} \text{m})] + \min[\|G_{E,45^\circ}(z, \cdot)\|_1 \|f(\cdot)\|_2, \|G_{E,45^\circ}(z, \cdot)\|_2 \|f(\cdot)\|_1]$. The norms $F_3(z) = \|G_{E,45^\circ}(z, \cdot)\|_2$ and $F_4(z) = \|G_{E,45^\circ}(z, \cdot)\|_\infty$ are graphed in Fig. 6, and $\|G_{E,45^\circ}(z, \cdot)\|_1$ was observed to decrease slowly and monotonically from 0.149 at 0.240 mm to 0.144 at 3.00 mm. We numerically tested these oblique-incidence inequalities using the five pulses in Table 1. The inequalities were validated in each case, and the minimum upper bound was almost attained in the case of a DC-component pulse (Example 1).

We will now substantiate the results in the last two paragraphs of Subsection 2B. The results rely mainly on (2.2) and Fig. 1. Note that the first term on the right side of (2.2) represents a wave that travels with speed c_0 and decays exponentially by a factor of 132 in each 0.300 mm interval. Therefore the convolution term in (2.2) predominates for depths greater than 0.300 mm. The major features, such as the peaks, of the convolution kernel G_E are seen in Fig. 1 to travel more slowly than c_0 for depths greater than 0.500 mm. The peak of $G_E(z, t)$, for instance, is shown in Fig. 7 to travel with speed c_0 for the first 0.300 mm, and then to slow gradually to $c_0/9.0$. (The small non-monotonic feature at shallow depths is a numerical artifact caused by applying the $\max(\cdot)$ function to a peak that is broad.) The numerically determined fast speed c_0 and the slow speed $c_0/9.0$ agree quantitatively with analytical results in Subsection 2A, and also substantiate the results in the next-to-last paragraph of Subsection 2B.

The last paragraph of Subsection 2B concerns elemental pulses $f_e(t)$, which are zero except on a single time interval, during which they are either strictly positive or strictly negative. For example, the Green function $G_E(z, t)$ is an elemental

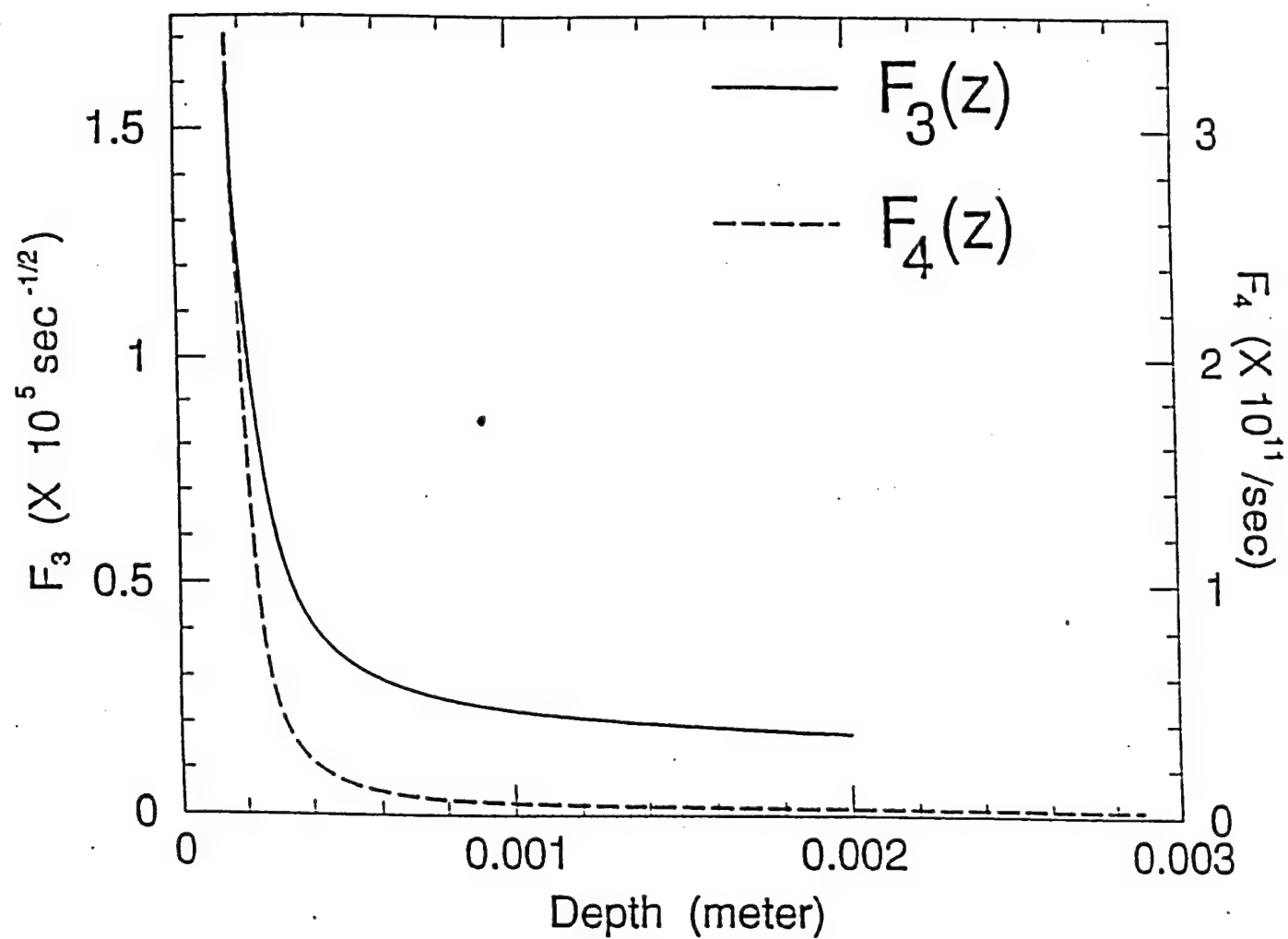


Fig. 6. The L_2 norm $F_3(z)$ and the L_∞ norm $F_4(z)$ of the Green function $G_{E,45\bullet}(z, \cdot)$.
The paragraph below (3.13) relates these norms to upper bounds for obliquely incident pulses.

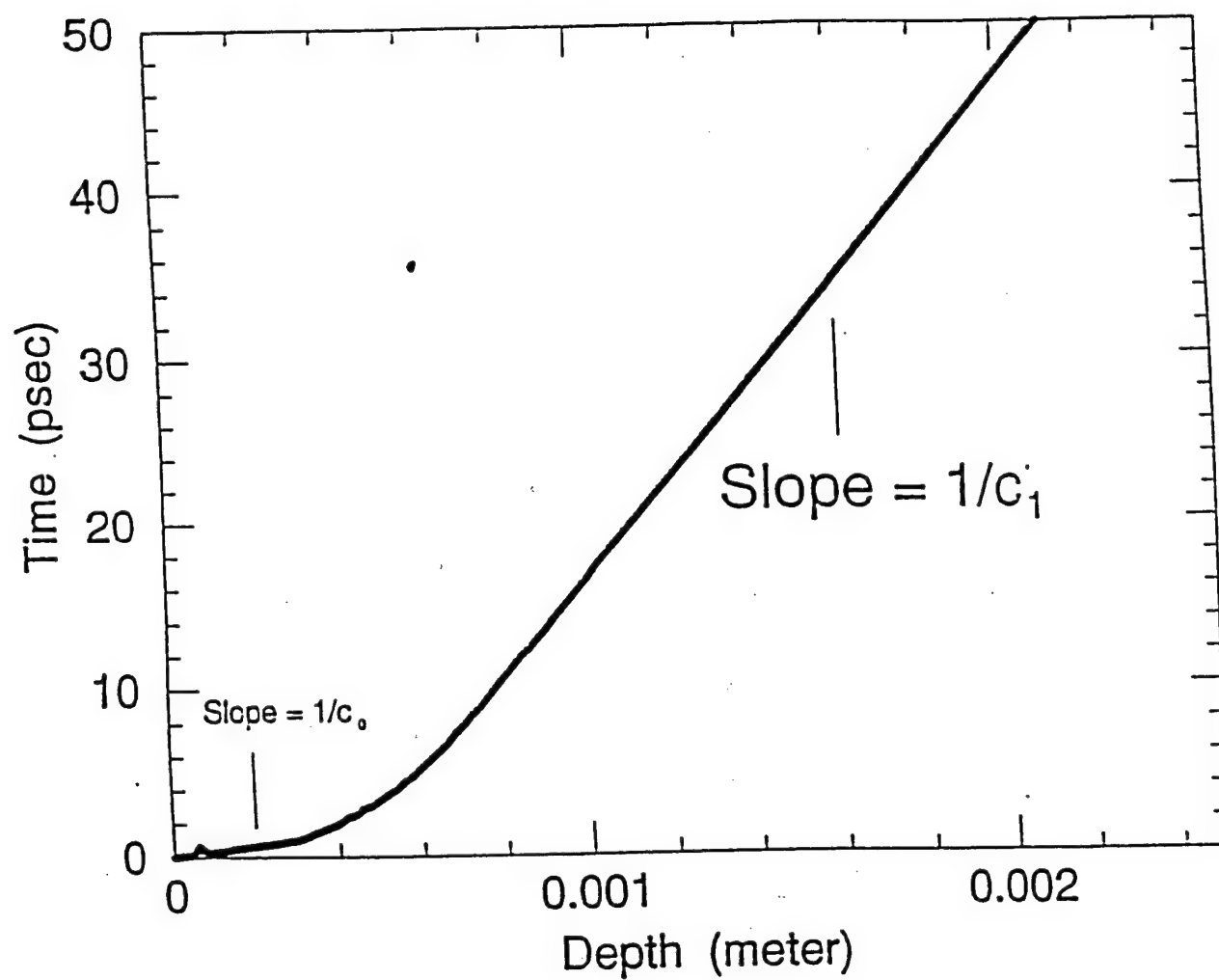


Fig. 7. The time of arrival of the peak of the Green function $G_E(z, t)$ at various depths in water.

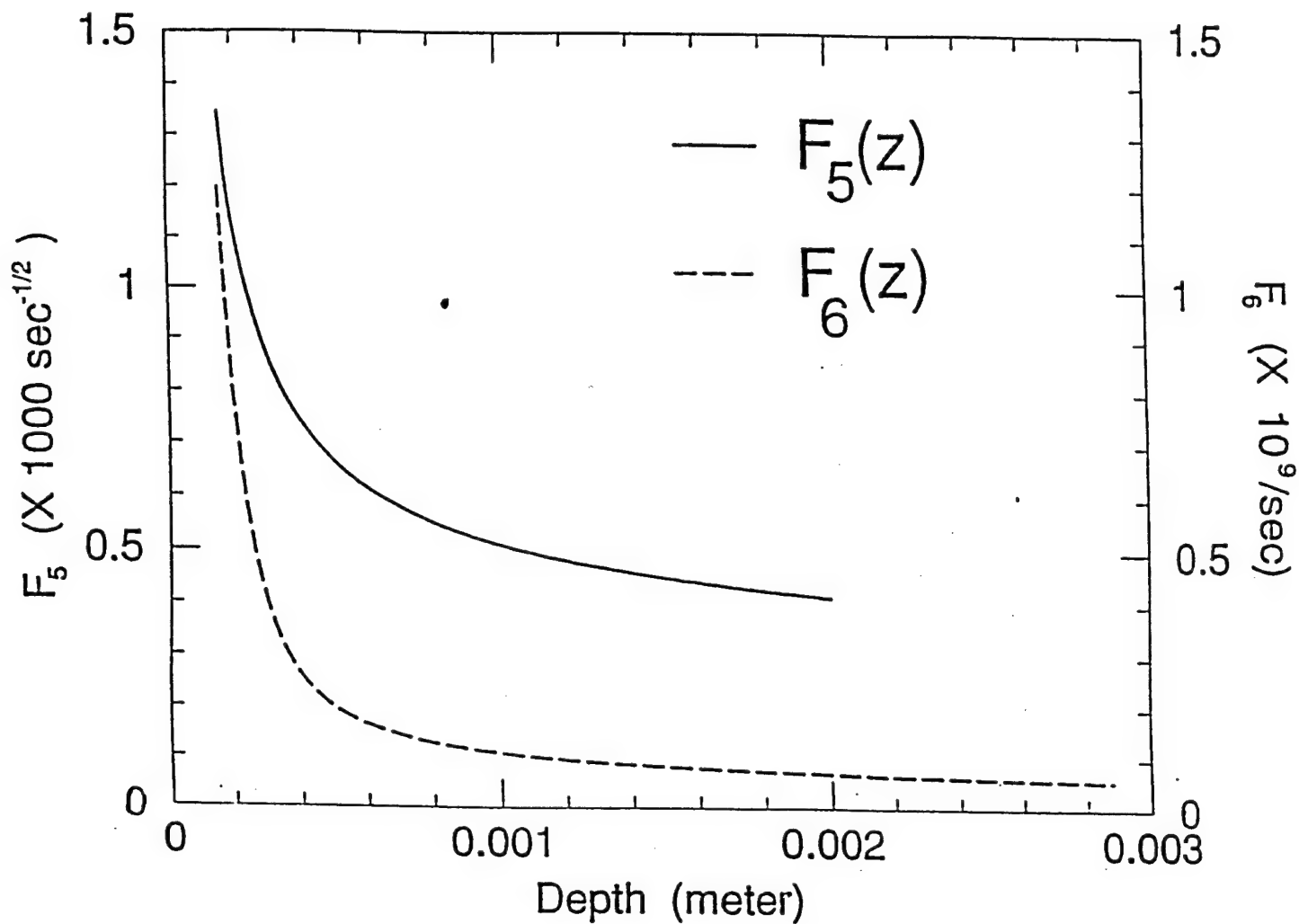


Fig. 8. The L_2 norm $F_5(z)$ and the L_∞ norm $F_6(z)$ of the Green function $G_{H,45^\circ}(z, \cdot)$ for magnetic fields produced by pulses that are incident on water at an angle of 45° . The last paragraph of Section 3 relates this figure to upper bounds for $\partial_t H$:

pulse for all of the depths graphed in Fig. 1. The statements in Subsection 2B that concern the propagation of elemental pulses all rely on the following approximation: If an elemental pulse $f_{\text{brief}}(t)$ is much briefer than an elemental pulse $f_{\text{long}}(t)$, and if $f_{\text{brief}}(t)$ is concentrated at the time t_0 , then $|\int_0^t ds f_{\text{brief}}(t-s) f_{\text{long}}(s)| = |\int_0^t ds f_{\text{long}}(t-s) f_{\text{brief}}(s)| \approx \|f_{\text{brief}}(\cdot)\|_1 |f_{\text{long}}(t-t_0)|$. That approximation is associated with the concept of δ -sequence functions in the elementary theory of Dirac delta functions. We also note that the exponential term in (2.2) quickly becomes negligible because it decays by a factor of 132 across each 0.300 mm interval of depth. These three results—the negligible exponential, the approximation of the convolution, and the observation that G_E is an elemental pulse—together with (2.2) and Fig. 1 yield the brief-pulse result in Subsection 2B, which has the term $\|f_e\|_1 G_E(z, t)$. The long-pulse result in that subsection uses the additional observation, below (3.8), that $\|G_E(z, \cdot)\|_1$ is approximately constant, and the time shift in the long-pulse result in Subsection 2B also relies on Fig. 7 and results from the previous paragraph.

In a final matter we would like to make it clear that we do not know what are the medical effects of isolated pulses. We have, however, developed methods that are flexible enough that they may be useful once the medical effects are known. Although we originally developed the upper-bound method along the lines of peak amplitudes and power densities, following Ref. 5, the method can easily be extended to, say, the time derivative of the magnetic field $H_x(z, t)$. To demonstrate the extension, we computed the Green function G_H in $H_x(0, z, t) = -\left[e^{-az} f(t-z/c_\infty) + \int_{z/c_\infty}^t ds f(t-s) G_H(z, s)\right] / (\mu_0 c_\infty)$ using the methods of Refs. 13-17, and we validated the computation as described in Section 4. The Green-function representation for H_x yields the following analog of (3.6): $\mu_0 c_\infty \|\partial_t H_x(z, \cdot)\|_p \leq e^{-az} \|\partial_t f(\cdot)\|_p + |f(0)| \|G_H(z, \cdot)\|_p + \|G_H(z, \cdot)\|_r \|\partial_t f(\cdot)\|_q$, where $r^{-1} = p^{-1} + q^{-1} - 1$ and $1 \leq p, q, r \leq \infty$. The norms $F_5(z) = \|G_{H,45^\circ}(z, \cdot)\|_2$ and $F_6(z) = \|G_{H,45^\circ}(z, \cdot)\|_\infty$ for that inequality are graphed in Fig. 8 for the 45°-incidence, magnetic Green function $G_{H,45^\circ}$.

4. NUMERICAL VALIDATION AND LABORATORY EXPERIMENTS

We validated the numerical results obtained with the Green's function approach by comparing the computed electric and magnetic fields in a Debye half-space (Section 2, $\phi_{inc} = 0$) to those computed with a finite difference method.²³⁻²⁴ Figure 9 shows electric field time-traces computed at three spatial locations in the half-space due to a $T_p = 40$ -psec square pulse of initial amplitude 1 V/m. We note excellent agreement to within a width of the line over an amplitude scale of 10 orders of magnitude. This indicates a better than 1-part-per-billion agreement. (The small difference increases to two-pen-strokes' width at the shallowest depth, but only after the field itself decreases by a factor one thousand.) Also, the speeds of the first arrival and of the peak of the response can be deduced from this graph. We see that the first arrival occurs with speed $c_o = c$, while the peak of the response arrives with the speed $c_1 = 0.1116c$ as predicted in Section 2. Figure 10 shows a comparison of magnetic fields, computed with the two methods at three depths in the half-space, for a square-modulated sinusoidal pulse of $T_p = 50$ -psec duration and carrier frequency 80 GHz. Again similarly excellent agreement is noted.

Next, we confirm the analytical results presented in Subsection 2A by solving, with the Green's function method, for the impulse response, $f(t - x/c) = \delta(t - x/c)$, of the Debye half-space described there for $\phi_{inc} = 0$ ($\xi = t$). To determine the two speeds predicted by (2.1) the peak of the impulse response was obtained from the simulation results. The temporal versus the spatial location of the peak's occurrence is graphed in Figure 7. The slope of the graph is the reciprocal of the speed of the peak of the response. The relative unimportance of the characteristic $z = c_o t$ (equivalently, the wavefront speed) with respect to the sub-characteristic $z = c_1 t$ is immediately evident. The value of the slope is given in Figure 7 for two ranges of depth. We see that for depths of $O(c_o \tau)$ the response travels with the speed c_o , and then slows down in another $O(c_o \tau)$ interval. This additional interval will be much smaller or altogether absent for band-limited pulses. Eventually, the pulse travels with the speed c_1 for the remainder of the half-space. The diffusive character of the main disturbance in the half-space is exemplified in Figure 11 where the numerically obtained $\max\{E^\delta\}$ is compared with the analytically predicted behavior $(1/\sqrt{z})$ as a function of depth. The

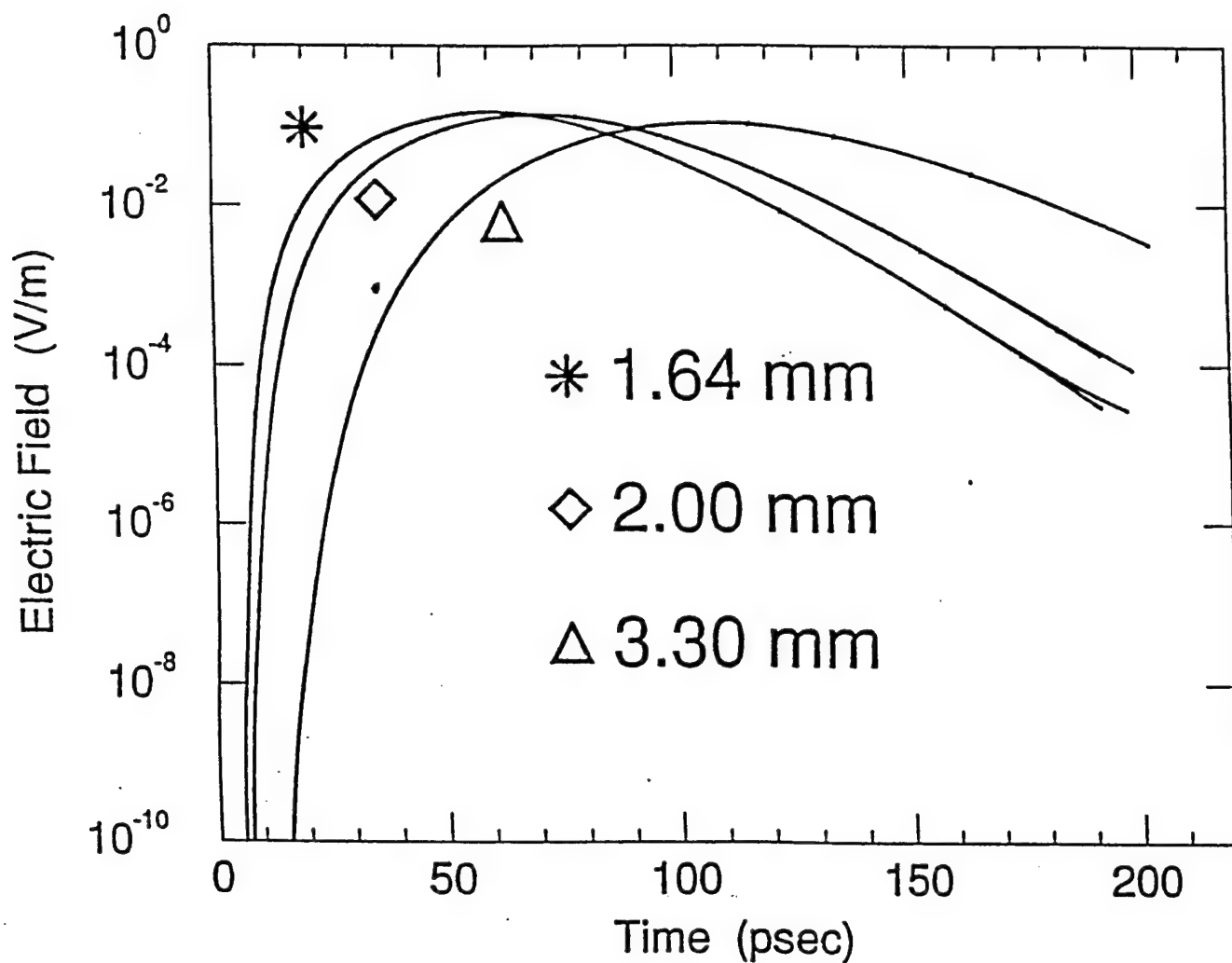


Fig. 9. The electric fields, at three depths in water, that result from a normally incident 40-psec square pulse of 1-V/m amplitude. At the three depths graphed, the fields are precisely 0 until 5.46 psec, 8.20 psec, and 9.60 psec respectively.

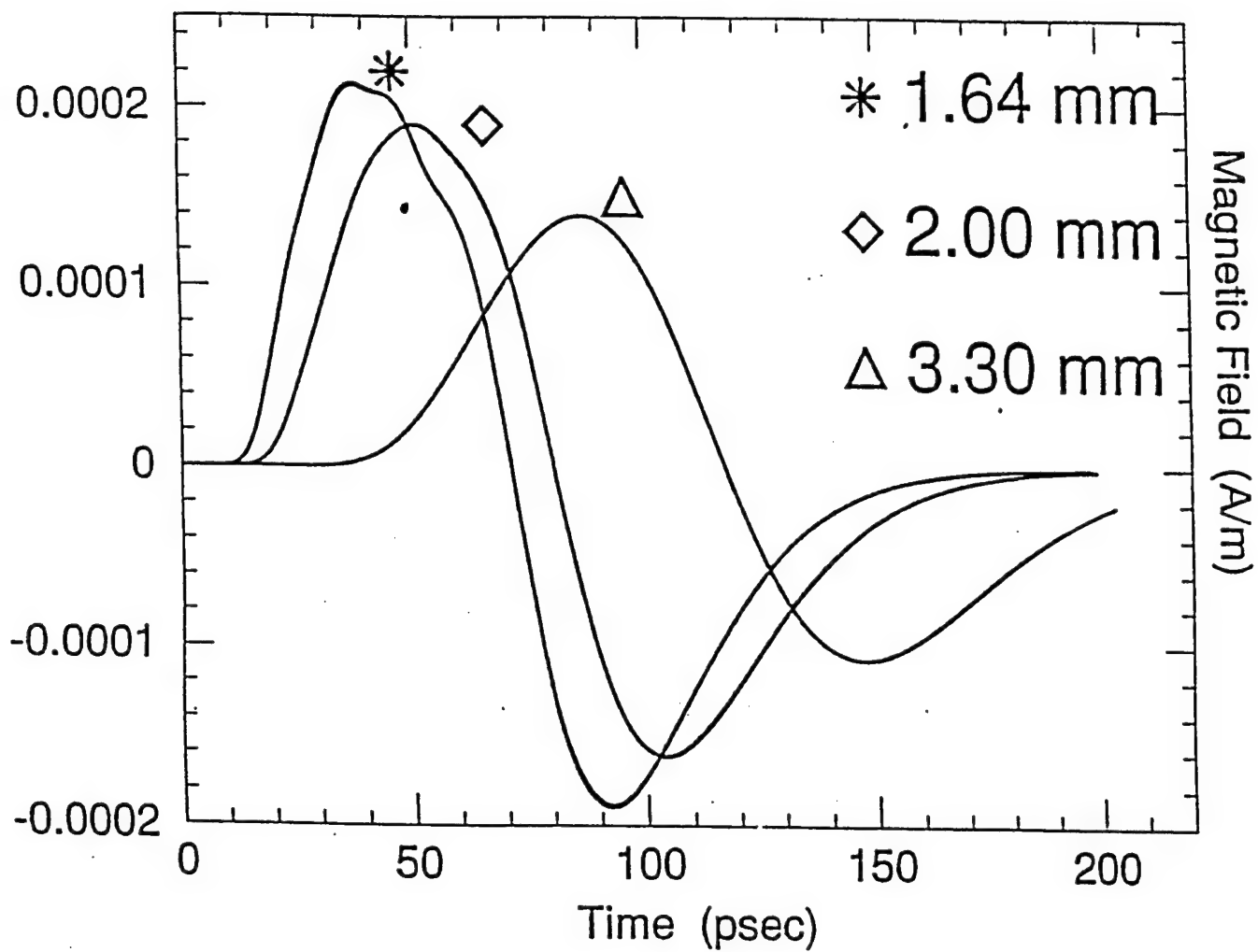


Fig. 10. The magnetic fields that result from a normally incident 4-cycle 1-V/m-amplitude square-modulated sinusoid of 50-psec duration.

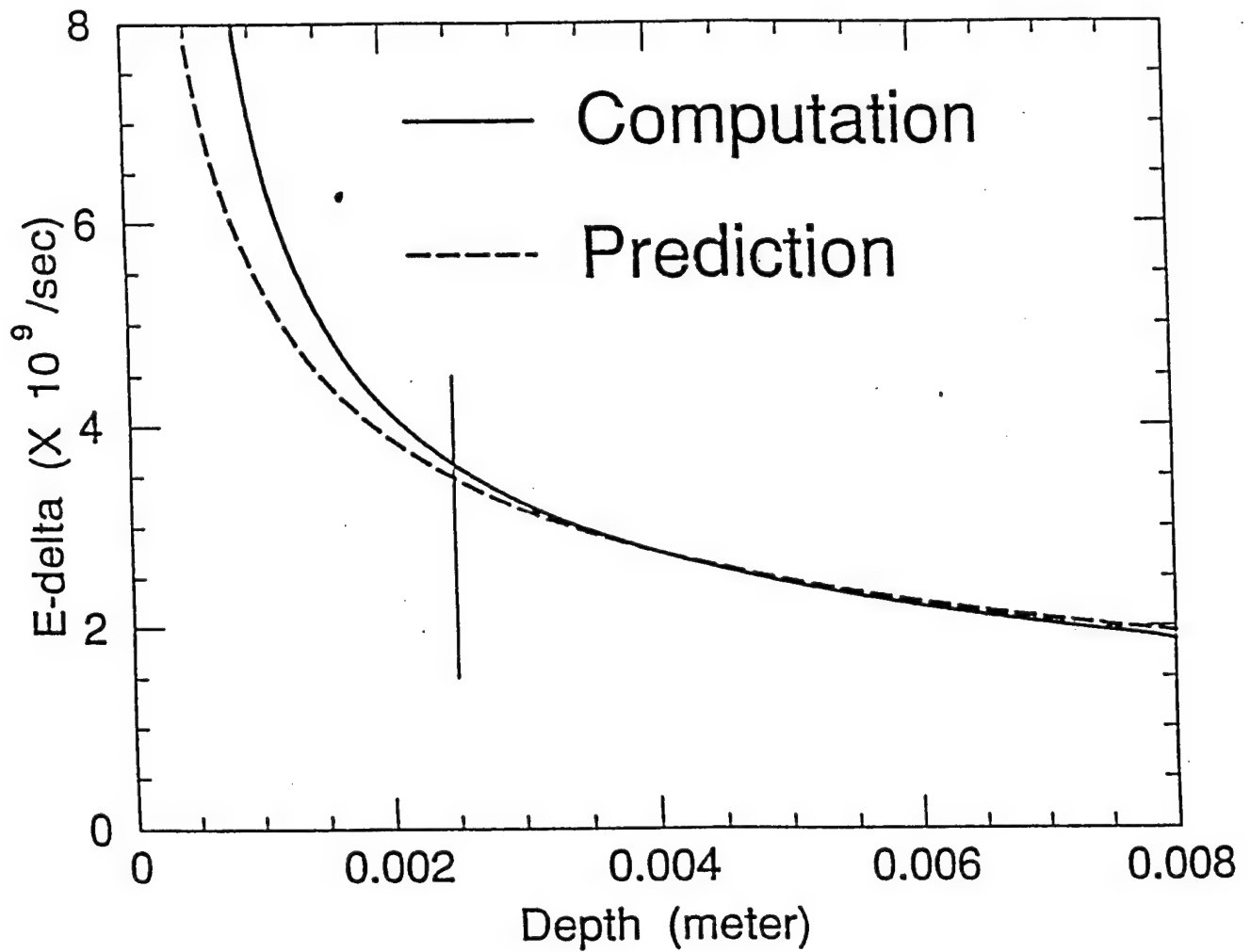


Fig. 11. The predicted and computed decays of the peak field as a function of depth.

constant of proportionality for the $1/\sqrt{z}$ prediction was fit to the data at the center-point (4 mm) of the graph. We note that although the slow speed is achieved very early on ($z \sim 0.1$ mm), it takes some time for the pulse to start diffusing ($z \sim 2.5$ mm). This delay depends on the frequency content of the incident signal, and will be shorter for band-limited pulses. From the discussion and figures it is evident that the envelope and duration of the incident pulse control the magnitude and nature of the response of the medium. Any high-frequency carrier component decays exponentially with depth. Similar behavior was observed in numerical simulations with square pulses of various durations. All long duration pulses were found to travel unattenuated with amplitude $T(\omega = 0) \times \max\{E^{inc}\}$, and square modulated sinusoidal pulses of various carrier frequencies and durations (1 to 10 cycles) behaved like the Green's function with the carrier component exponentially small.

We also checked the sensitivity of our calculations to the way in which we modeled the water data of Ref. 2. Reference 25 points out that many other data sets are available for water, so we were satisfied with any model that fit the data in Ref. 2 to within 10%. In particular, we examined several Debye-model fits to the data in Ref. 2 for frequencies that are below 100 GHz and for which the data are also said, in the reference, to be reliable. Our experience in fitting those data is that ϵ_∞ can be taken to be any number from 1.00 through 10.0, and then values for the two other Debye parameters, ϵ_s and τ , can be found that fit the data to within 10%. In that sense, the value of ϵ_∞ is somewhat arbitrary; for most of our simulations we chose $\epsilon_\infty = 1.00$, which is consistent with an assumption in Ref. 2. The corresponding Debye parameters are $\epsilon_\infty = 1.00$ and $\epsilon_s = 80.35$ and $\tau = 8.13 \times 10^{-12} \text{s}^{-1}$ in the notation of Subsection 2A, or, equivalently, $a = 9.76 \times 10^{12} \text{s}^{-1}$ and $b = 1.23 \times 10^{11} \text{s}^{-1}$ in the notation of (3.13). This fit is referred to as Model 1 in Fig. 12; it is the fit that is used in most of the numerical computations in this paper. Another model that fits the water data to within 10% accuracy is defined by $\epsilon_\infty = 5.50$ and $\epsilon_s = 78.20$ and $\tau = 8.1 \times 10^{-12} \text{s}^{-1}$, or, alternatively, $a = 8.98 \times 10^{12} \text{s}^{-1}$ and $b = 1.23 \times 10^{11} \text{s}^{-1}$. This second model is used only in Fig. 12, where it is called Model 2. The propagation of an incident 5-cycle 8-GHz 1-V/m-amplitude square-modulated sinusoid was computed for these two models. Figure 12 shows the resulting electric field produced at a 9.75-mm depth for both models. We compared the electric fields at 31 other representative

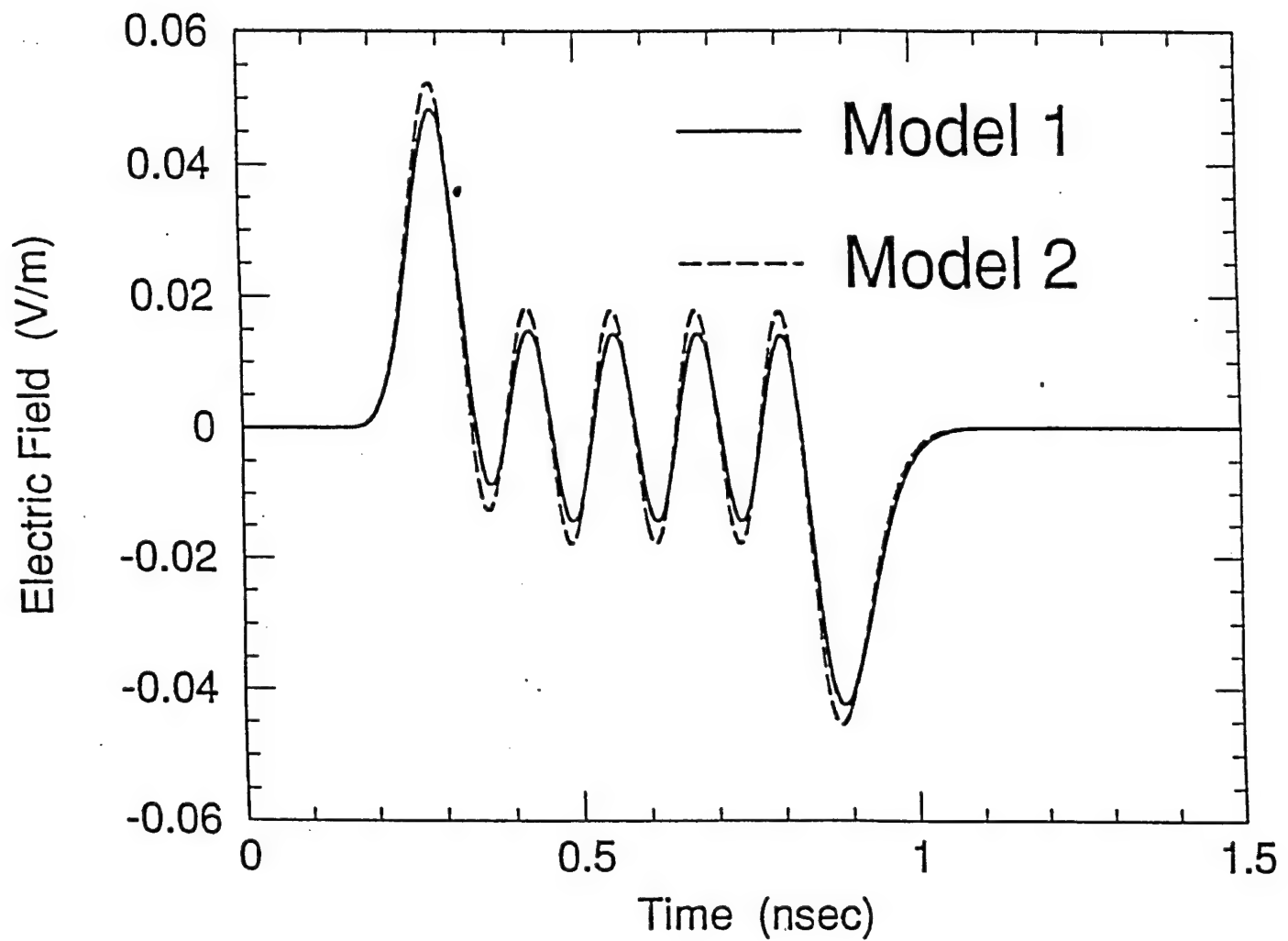


Fig. 12. Electric fields for two models of water. The fields, which result from the same incident pulse, are computed at a 9.75-mm depth for each model.

depths, from 0 cm through 4 cm, and observed similar agreement, commensurate with two different 10%-accuracy fits to the water data. A similar degree of agreement was also seen for the two models in computations for the following incident fields: (1) A 1-cycle 8-GHz square-modulated sinusoid; (2) A 1-cycle 10-GHz square-modulated sinusoid; (3) A 50-psec square pulse; and (4) A 100-psec square pulse. These results are numerical evidence that the computed internal fields are stable as the water model is perturbed by about 10%.

Now we wish to provide an explanation, based on the understanding developed herein, of the observations in Ref. 3 whereas no significant differences in SAR (Specific Absorption Rate) distribution between pulsed and CW (Continuous Wave) exposures were measured for a MEM (Muscle Equivalent Material) exhibiting two relaxation times. The dielectric model was composed of two Debye mechanisms, which fit experimentally determined permittivity and conductivity data for MEM at 2.07, 2.8, 5.6, and 9.3 GHz. The two relaxation times were $\tau_1 = 6.63$ psec, and $\tau_2 = 83.7$ psec. The material was illuminated with a train of square-modulated pulses of various durations and repetition rates. We will explain the observations in Ref. 3 for the smallest pulse repetition rate used (200 pulses per second) for which the pulse duration was $0.5 \mu\text{sec}$. All other results in Ref. 3 with different pulse settings are similarly explained. For this incident signal the author of Ref. 3 used a carrier of 5.6 GHz. Thus, the pulse duration was $T_p = 5 \times 10^{-7}$ sec, the quiescent interval between pulses was $T_q = 5 \times 10^{-3}$ sec, and each pulse contained 2800 cycles of carrier. Further, it happened that $T_p \gg \max\{\tau\} = \tau_2$, thus the medium would not respond in a dispersive manner, rather it exhibited an effective relative permittivity of $\epsilon'_1 + \epsilon'_2 - \epsilon_\infty = 42.4 + 15.8 - 4.3 = 53.9$ to the envelope of the pulses. With these parameter values in mind we expect the medium to sense a CW signal of carrier 5.6 GHz, even in the pulsed case. Since the MEM has low heat diffusivity, i.e., it takes about 40 sec for a temperature change of 0.04°C to occur, its temperature will change immeasurably in the time T_q between pulses. Consequently, the temperature will remain constant until the next pulse arrives again to be seen by the medium as part of a CW exposure, hence the observed indistinguishability of the CW SAR versus the pulsed SAR. As the carrier frequency is increased the CW vs. pulsed exposure SARs should start disagreeing at smaller depths. This is related to the frequency-

dependent skin depth for the carrier component which is 9.7 mm at 5.6 GHz. All the measurements of SAR were obtained at depths well within the skin depth. The effects of the pulsing should be observable at depth greater than $c_0\tau_2 \sim 1.2$ cm since then the carrier component will have decayed sufficiently (it is exponentially decaying as in the CW case) so the remaining field will be due to the square envelope and will behave diffusively.

The results presented in our paper also help in accurately predetermining sample thickness to be used in single and total transmission Time Domain Spectroscopy (TDS) studies such as those presented in Ref. 26. In the single transmission approach one studies the first arrival through a long sample so that the highest frequency components will have decayed sufficiently in order not to mask the lower frequency components which, as we showed in Section 2, are significantly slower (for water $c_1 \sim c_0/9$). The first suggestion arising from the analysis of Section 2 (verified by the numerical simulations) is that the sample can be as short as $2c_0\tau$ when one is interested in measuring the static permittivity of a Debye-like material with single transmission TDS. On the other hand, in the total transmission approach the first arrival time through a short sample is used to best measure the infinite-frequency permittivity of the material under test. Therefore, a sample length shorter than $c_0\tau$ should be appropriate in order to capture the time of arrival of the highest frequencies and thus determine ϵ_∞ . (The next-to-last paragraph of Section 2 has related comments.) For the test case presented in the results section of Ref. 26 [Eqn. (8) there] it happens that $\epsilon_s = 17.3$, $\epsilon_\infty = 3.3$, $\tau = 460$ psec. Thus, the highest frequency components travel with a speed $c_0 = 0.5505c$, the lowest frequency components travel with speed $c_1 = 0.2673c$, and $c_0\tau = 7.6$ cm. The experimenters could have used a slab of material of at least 15 cm to reliably measure ϵ_s , and a slab thickness of at most 7 cm to measure ϵ_∞ , instead of using 50 cm and 2.7 cm respectively to do the measurements. In Figure 13 we show the x - t location of the peak of the impulse response for this medium. (The two data points in one corner of the graph are minor numerical artifacts that are related to the similar numerical artifacts in Fig. 7.) The graph as a whole confirms our predictions of the sample lengths with which TDS will be most successful in measuring the permittivities.

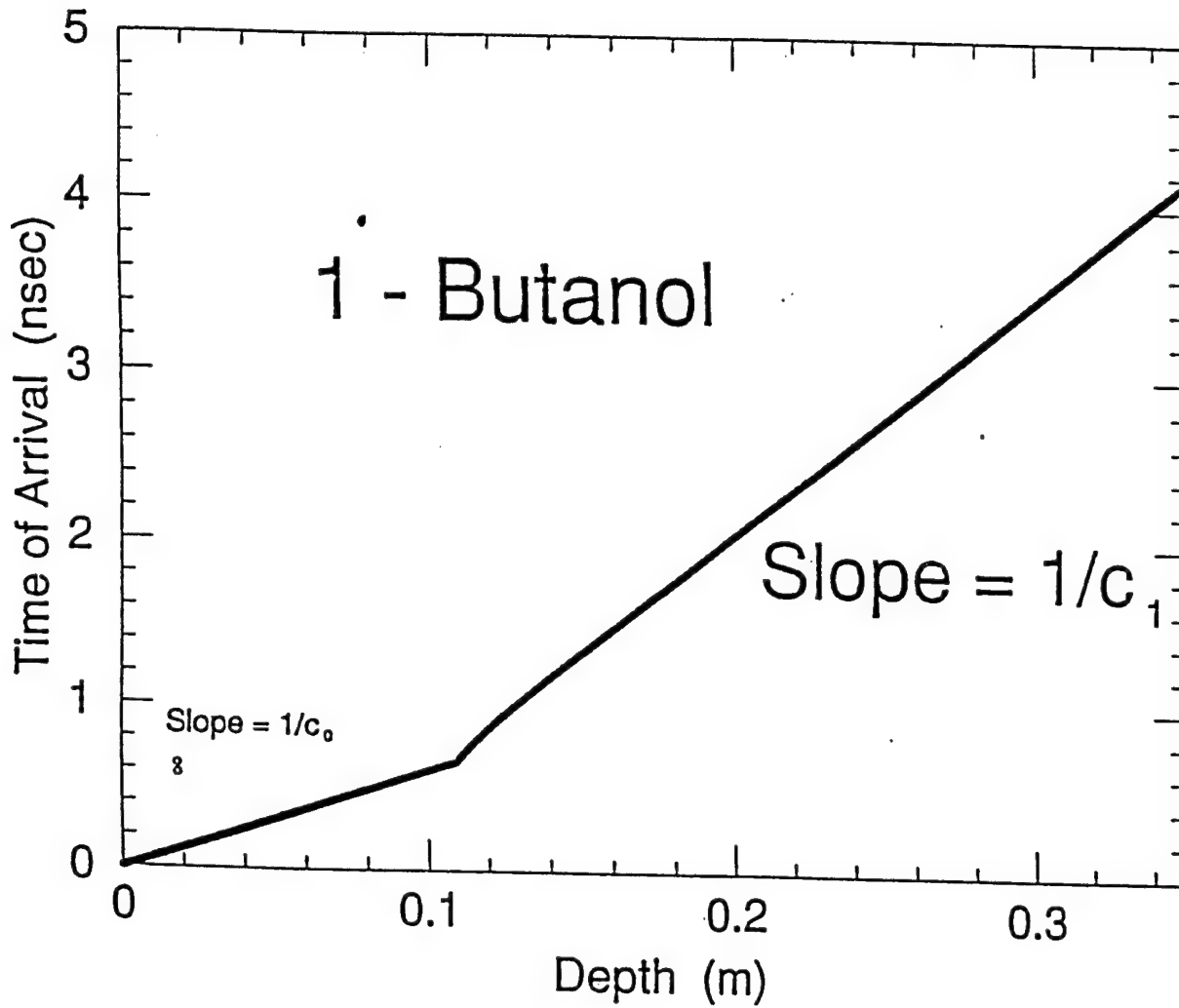


Fig. 13. The time of arrival of the peak of the Green function $G_E(z, t)$ at various depths in the medium of Ref. 26.

5. CONCLUSION

There are many generalized methods for computing the response of any single dispersive medium to any single incident pulse. This paper has contributed nothing along those lines; instead, we have developed several related results that are general in a different way. We have found, for instance, that the power density and the peak amplitude of an incident pulse place upper bounds on the peak amplitude suffered inside a dispersive medium—independent of the other details of the incident pulse. Our Green-function results reduce the computation of such upper bounds to little more than a calculator exercise, and we have given numerical examples in which these sharp upper bounds are almost attained. We have reported similar upper-bound estimates for a quantity related to power density, and for the time derivative of the magnetic field. That time derivative, $\partial_t H$, is largely responsible for electromotive-force currents in circuit-like structures; it is especially large for short-risetime pulses. Such upper bounds could, potentially, help in the regulation of electromagnetic interference or damage produced in dispersive media.

Although our methods apply to dispersive media generally, we have used a Debye model for microwave-pulse propagation in water as a specific numerical example. For that water example, we reported a factor-of-nine effect in the wave speeds that seems to have been unnoticed until now, and we explained this large effect analytically using PDEs. The PDE analysis also yielded simple short-pulse and long-pulse approximations, as did an analysis of the numerical Green functions involved in the upper-bound concepts described earlier. We studied rates of decay in Subsection 2A, and approximations for detailed time traces are given in Subsection 2B and Eqns. (3.2) and (3.4). Section 4 uses that work to explain the results of some laboratory experiments, and to offer suggestions for future experiments.

APPENDIX A: ERROR ESTIMATES

This appendix develops an easily used method for estimating the percentage error in grid-dependent computations. The estimates are validated numerically in some cases for which exact solutions are known, and the estimates are also used in cases for which exact solutions are not known. These estimates use only one of the many definitions of relative error for functions of two variables, but the estimates can easily be adapted to other measures of relative error and to functions of more than two variables. We were motivated to estimate percentage errors because quantitative estimates of uncertainty could help in setting safety standards or in the use of other computations for which measures of numerical uncertainty are vital.

The error estimates in this paper are empirical. The estimates are obtained by computing with several different grid sizes, noticing a pattern in the relative errors of the different computer runs, and using that inferred pattern to sum the series on the right side of the inequality $\|f_c - f_e\|_\infty \leq \|f_c - f_1\|_\infty + \|f_1 - f_2\|_\infty + \|f_2 - f_3\|_\infty + \dots$. The concepts of rate and order of convergence are not used in these empirical estimates. The logic behind the estimates is slightly intricate, but the resulting method uses only least upper bounds and geometric means and geometric series, which are extraordinarily simple concepts.

We will estimate relative errors for functions of two variables. The error in a computed solution $f_c(z, t)$ relative to the exact solution $f_e(z, t)$ can be defined as

$$E_{\text{rel}}[f_c, f_e] = \frac{\|f_c(z, \cdot) - f_e(z, \cdot)\|_\infty}{\|f_e(z, \cdot)\|_\infty}. \quad (A1)$$

The relative error (A1) is a function of the depth z . For instance, if the relative error is known to be less than 1% over a range of depths z , then, for those depths, the exact solution $f_e(z, t)$ can differ from the computed solution $f_c(z, t)$ by no more than 1% of the peak value (with respect to t) of $|f_e(z, t)|$. The just-mentioned peak value of $|f_e(z, \cdot)|$ is unknown in all practical cases in which the exact solution f_e is unknown; however, in the present hypothetical case of 1% relative error, the peak value of the unknown quantity $|f_e(z, \cdot)|$ can differ by no more than 1% from the peak value of the known quantity $|f_c(z, \cdot)|$. A brief derivation involving a geometric series then shows that, in the case of 1% relative error, the graph of the exact solution

$f_e(z, t)$ is guaranteed to fall between the graph of $f_c(z, t) + 1.01\% \|f_c(z, \cdot)\|_\infty$ and the graph of $f_c(z, t) - 1.01\% \|f_c(z, \cdot)\|_\infty$. The quantities $\pm 1.01\% \|f_c(z, \cdot)\|_\infty$ are called error bars.

We will now go step by step through the error estimates illustrated in Fig. 14. Those estimates are for Green-function computations of waves normally incident on water. The computations were done for five different grids, and the results are called $f_1(z, t), f_2(z, t), \dots, f_5(z, t)$ in order of the increasing fineness of the grids. Because of computer limitations, the finer-grid computations were done for shallower depths than were the coarser-grid computations. For zero depth, the light circles on the $z = 0$ axis of Fig. 14 represent $\|f_1(0, \cdot) - f_2(0, \cdot)\|_\infty / \|f_5(0, \cdot)\|_\infty$, $\|f_2(0, \cdot) - f_3(0, \cdot)\|_\infty / \|f_5(0, \cdot)\|_\infty$, $\|f_3(0, \cdot) - f_4(0, \cdot)\|_\infty / \|f_5(0, \cdot)\|_\infty$, and $\|f_4(0, \cdot) - f_5(0, \cdot)\|_\infty / \|f_5(0, \cdot)\|_\infty$, running from top to bottom along the vertical axis. For instance, the error in $f_4(0, t)$ relative to the most finely computed result $f_5(0, t)$ is 0.157%. The even spacing of the four light circles along the logarithmic, vertical axis of Fig. 14 suggests that the four relative errors are in geometric progression; in fact, the ratio of the second-largest relative error to the largest relative error is 0.368, the ratio of the next two smaller relative errors is 0.284, the ratio of the two smallest relative errors is 0.268, and the geometric mean of the three previous numbers is 0.304. For those reasons we assume

$$\frac{\|f_{n+1}(0, \cdot) - f_{n+2}(0, \cdot)\|_\infty}{\|f_5(0, \cdot)\|_\infty} \approx (0.304)^n \frac{\|f_1(0, \cdot) - f_2(0, \cdot)\|_\infty}{\|f_5(0, \cdot)\|_\infty}, \quad (A2)$$

even for hypothetical results, such as f_{100} , which would come from computations involving a much-finer grid than was used for the actual computation of f_5 . We also assume that the exact result $f_e(z, t)$ is the $n \rightarrow \infty$ limit of $f_n(z, t)$. The triangle inequality for norms then implies $\|f_1 - f_e\|_\infty \leq \|f_1 - f_2\|_\infty + \|f_2 - f_3\|_\infty + \|f_3 - f_4\|_\infty + \dots$. We use (A2) in the right side of the previous inequality to get a geometric series, which sums to

$$\frac{\|f_1(0, \cdot) - f_e(0, \cdot)\|_\infty}{\|f_5(0, \cdot)\|_\infty} \lesssim \frac{1}{1 - 0.304} \frac{\|f_1(0, \cdot) - f_2(0, \cdot)\|_\infty}{\|f_5(0, \cdot)\|_\infty} = 8.08\% \quad (A3)$$

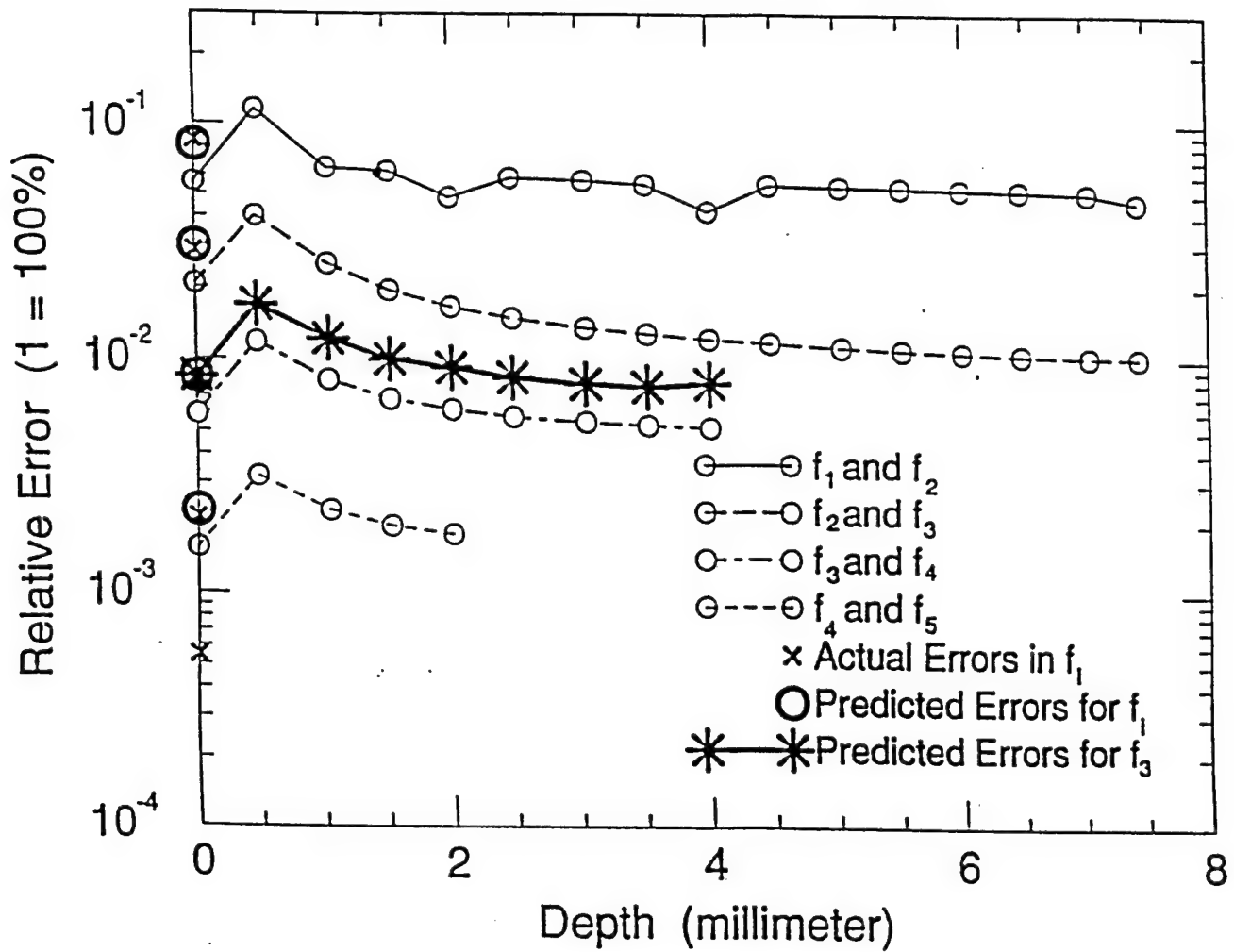


Fig. 14. Relative errors for the computation of G_E for water. The bold marks represent the final error estimates and their numerical validations. The lighter marks represent intermediate steps in the computation of error estimates.

at $z = 0$. That 8.08% estimated relative error is plotted as the top-most heavy circle on the vertical axis of Fig. 14. The analysis was repeated for the relative errors of other computations f_i , yielding

$$\frac{\|f_i(0, \cdot) - f_e(0, \cdot)\|_\infty}{\|f_5(0, \cdot)\|_\infty} \lesssim 1.44 \frac{\|f_i(0, \cdot) - f_{i+1}(0, \cdot)\|_\infty}{\|f_5(0, \cdot)\|_\infty}, \quad (A4)$$

for $i = 1, 2, 3, 4$. Those estimated relative errors are also plotted as heavy circles on the vertical axis of Fig. 14.

Reference 9 has an exact, closed form, modified-Bessel-function expression of the zero-depth Green function for a half-space of Debye medium. That exact solution f_e was used to compute the true relative errors $E_{rel}[f_i, f_e]$ at $z = 0$. Those true relative errors are plotted as the bold Xs on Fig. 14. The true relative errors (bold Xs) validate the error estimates (bold circles) because the two sets of errors match closely; for instance, the error estimate (A4) for $f_3(0, \cdot)$ was that there would be 0.844% error relative to f_e , and the actual error in $f_3(0, \cdot)$ relative to f_e was 0.797%. Our percentage-error method involving geometric means and geometric series is thereby validated.

The relative errors $\|f_i(z, \cdot) - f_{i+1}(z, \cdot)\|_\infty / \|f_5(z, \cdot)\|_\infty$ were then computed at the depths $z = 0.480$ mm, 1.04 mm, 1.52 mm, and 2.00 mm, for $i = 1, 2, 3, 4$. Those results are plotted as some of the light circles to the right of the vertical axis in Fig. 14. Error estimates for $f_3(z, \cdot)$ were computed using the geometric-series technique in (A2)–(A4), with the results plotted as several bold asterisks on Fig. 14. The ratios of relative errors and the geometric means of the ratios were computed separately for each depth. In particular, the geometric means for the four depths mentioned in this paragraph are 0.302, 0.328, 0.315, and 0.333 for 0.480 mm through 2.00 mm, consecutively. We will now explain how the relative errors for depths beyond 2.00 mm were computed.

The finest-discretization run was not computed beyond 2.00 mm for reasons related to computer resources. Thus, only f_1 , f_2 , f_3 , and f_4 were analyzed for the depths from 2.48 mm through 4.00 mm. These analyses were done as described in the previous paragraph, and the geometric means were also computed separately for each depth. Similarly, the runs f_1 , f_2 , and f_3 were analyzed for depths from

5.04 mm through 7.04 mm. In these computations, and in all other computations described in this appendix, the L_∞ norms were computed using 90 evenly spaced time points.

The final result in Fig. 14 is symbolized by the bold asterisks there. The result is that $f_3(z, t)$ has errors relative to f_e that are expected to fall monotonically from about 1.70% at $z = 0.480$ mm to about 0.799% at $z = 4.00$ mm. The error in $f_3(0, t)$ relative to $f_e(0, t)$ is actually 0.797%. Figure 14 shows that the relative errors are non-monotonic from 0.00 mm through 0.500 mm; therefore, we make no further inferences about the relative errors in that first half-millimeter.

REFERENCES

- [1] J. C. Lin and C. K. Lam, "Coupling of Gaussian electromagnetic pulse into a muscle-bone model of biological structure," *J. Microwave Power* 11, 67-75 (1976).
- [2] J. D. Jackson, *Classical Electrodynamics* 2nd ed., (Wiley, New York, 1975). See Secs. 7.5e, 7.7, and 7.11g.
- [3] W. D. Hurt, "Measurement of specific absorption rate in human phantoms exposed to simulated Air Force radar emissions," USAFSAM-TR-84-16 (June 1984) (Armstrong Laboratory, Brooks AFB, TX, 1984).
- [4] W. D. Hurt, "Multiterm Debye dispersion relations for permittivity of muscle," *IEEE Trans. Biomed. Engnr.* BME-32, 60-64 (1985).
- [5] *IEEE Standard for Safety Levels with Respect to Human Exposure to Radio Frequency Electromagnetic Fields, 3kHz to 300 GHz*, IEEE C95.1-1991 (IEEE Standards Board, New York, 1991).
- [6] P. Debye, *Polar Molecules* (Dover, New York, 1929). See p. 90.
- [7] F. John, *Partial Differential Equations*, 4th ed. (Springer-Verlag, New York, 1991). See pp. 152 and 160.
- [8] G. B. Whitham, *Linear and Nonlinear Waves* (New York, Wiley, 1974).
- [9] R. S. Beezley and R. J. Krueger, "An electromagnetic inverse problem for dispersive media," *J. Math. Phys.* 26, 317-325 (1985), Sec. IV. Equate their function $R(t)$ with our $G_E(0, t)$. See also our Eqn. (3.12).
- [10] J. A. Stratton, *Electromagnetic Theory* (McGraw-Hill, New York, 1941) Sec. 2.19. From (11) and $E_{inc} = f(t - z/c)$, one can show that the incident power density of the electric part $f(t)$ of an incident pulse is $(\epsilon_0/2) \int_{-\infty}^{\infty} dz |f(z/c)|^2 = (c\epsilon_0/2) \int_{-\infty}^{\infty} dt |f(t)|^2 = (c\epsilon_0/2) [\|f(\cdot)\|_2]^2$, whose mks units are Watt/m².

- [11] T. M. Roberts, "Causality Theorems," in *Invariant Imbedding and Inverse Problems*, J. P. Corones, G. Kristensson, P. Nelson, and D. L. Seth, eds. (Society for Industrial and Applied Mathematics, Philadelphia, Pa., 1992), pp. 114, 121, and 122-123.
- [12] E. Zauderer, *Partial Differential Equations of Applied Mathematics* (Wiley, New York, 1983), pp. 218-223 and 615-618.
- [13] R. J. Krueger and R. L. Ochs, Jr., "A Green's function approach to the determination of internal fields," *Wave Motion* **11**, 525-543 (1989).
- [14] R. Krueger and R. Winther, "Internal field, inhomogeneous dispersive medium" and other unpublished notes and computer programs, Ames Laboratory, Ames, Iowa 50011 (personal communication, 1989).
- [15] G. Kristensson, "Direct and inverse scattering problems in dispersive media — Green's functions and invariant imbedding techniques," in *Direct and Inverse Boundary Value Problems*, Vol. 37 of *Methoden und Verfahren der mathematischen Physik*, R. Kleinman, R. Kress, and E. Martensen, eds. (Peter Lang, Frankfurt, Germany, 1991).
- [16] T. M. Roberts and M. Hobart, "Energy velocity, damping, and elementary inversion," *J. Opt. Soc. Am. A* **9**, 1091-1101 (1992).
- [17] A. Karlsson, H. Otterheim, and R. Stewart, "Transient wave propagation in composite media: Green's function approach," *J. Opt. Soc. Am. A* **10**, 886-895 (1993).
- [18] M. Reed and B. Simon, *Methods of Modern Mathematical Physics II: Fourier Analysis, Self-Adjointness* (Academic, New York, 1975), pp. 28, 29, and 32.
- [19] C. E. Baum, "EMP simulators for various types of nuclear EMP environments: An interim categorization," *IEEE Trans. on Antennas and Propagat.* **26**, 35-53 (1978). See Sect. II.
- [20] J.-Y. Chen and O. P. Gandhi, "Currents induced in an anatomically based model of a human for exposure to vertically polarized electromagnetic pulses," *IEEE Trans. Microw. Theor. Tech.* **39**, 31-39 (1991). See Figs. 3(a) and 4.

- [21] F. M. Tesche, "Prediction of the E and H fields produced by the Swiss mobile EMP simulator (MEMPS)," IEEE Trans Electromagn. Compat. 4, 381-390 (1992). See Figs. 7, 10(a), 13(b), and 15(b).
- [22] In Sec. 7.11g of Ref. 2, take large-depth limits while keeping the relative time $|t - t_1|$ fixed. Then use (7.146)-(7.148), (7.141), and (3.89) to show that the large-depth, fixed-relative-time values of the Brillouin precursor decay as $(\text{depth})^{-1/3}$ if the frequency-domain amplitude $A(\omega)$ is nonzero at $\omega = 0$, and that the values decay as $(\text{depth})^{-2/3}$ if $A(\omega)$ has a first-order zero at $\omega = 0$. The error is $O(\omega^4)$.
- [23] R. M. Joseph, S. C. Hagness, and A. Taflov, "Direct time integration of Maxwell's equations in linear dispersive media with absorption for scattering and propagation of femtosecond electromagnetic pulses," Optics Letters 16, 1412-1414 (1991).
- [24] F. J. German, "The analysis of pulse propagation in linear dispersive media with absorption by the finite-difference time-domain method," unpublished report and computer program, Department of Electrical Engineering, Auburn University, Auburn, Alabama 36849 (personal communication, 1993).
- [25] M. R. Querry, D. M. Wieliczka, and D. J. Segelstein, "Water (H_2O)," in *Handbook of Optical Constants of Solids II*, Edward D. Palik, ed. (Academic Press, Boston, 1991), pp. 1059-1065.
- [26] B. Geelblom and E. Noreland, "Transmission Methods in Dielectric Time Domain Spectroscopy," J. Phys. Chem. 81, 782-788 (1977).